The Journal of Chemical Physics

RESEARCH ARTICLE | AUGUST 28 2025

Influence of vibrational motion and temperature on interatomic Coulombic electron capture

Elena M. Jahr ; Jan Šenk ; Jan P. Drennhaus ; Přemysl Kolorenč ; Nicolas Sisourat ; Elke Fasshauer

J. Chem. Phys. 163, 084313 (2025)
https://doi.org/10.1063/5.0280381

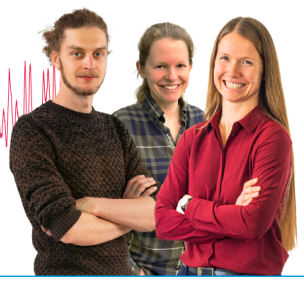

The Journal of Chemical Physics ARTICLE pubs.aip.org/aip/jcp

Influence of vibrational motion and temperature on interatomic Coulombic electron capture

Cite as: J. Chem. Phys. 163, 084313 (2025); doi: 10.1063/5.0280381
Submitted: 12 May 2025 • Accepted: 31 July 2025 •
Published Online: 28 August 2025

Elena M. Jahr,[1,2] Jan Šenk,[3,4] Jan P. Drennhaus,[5] Přemysl Kolorenč,[4] Nicolas Sisourat,[3] and Elke Fasshauer[1,2,a)]

AFFILIATIONS

[1] Institute of Physical and Theoretical Chemistry, University of Tübingen, Auf der Morgenstelle 18, 72076 Tübingen, Germany
[2] Center for Light-Matter Interaction, Sensors and Analytics (LISA+), University of Tübingen, Auf der Morgenstelle 15, 72076 Tübingen, Germany
[3] Laboratoire de Chimie Physique–Matière et Rayonnement, UMR 7614, Sorbonne Université, CNRS, F-75231 Paris Cedex 05, France
[4] Institute of Theoretical Physics, Faculty of Mathematics and Physics, Charles University, V Holešovičkách 2, 180 00 Prague, Czech Republic
[5] Institute for Theoretical Physics, Department of Physics and Astronomy, KU Leuven, Celestijnenlaan 200d, P.O. Box 2415, 3001 Leuven, Belgium

[a)] **Author to whom correspondence should be addressed:** elke.fasshauer@gmail.com

ABSTRACT

Interatomic Coulombic electron capture (ICEC) is an environment-mediated process in which a free electron attaches to a species by transferring excess energy to a neighbor. While previous theoretical investigations assumed fixed nuclei, recent studies indicate that nuclear dynamics significantly influences the ICEC process. In this work, we incorporate the vibrational motion into an analytical model of the ICEC cross section, including both energy and electron transfer. To validate this approach, we compare the results to the adiabatic-nuclei approximation based on fixed-nuclei *ab initio* R-matrix calculations. We apply our theory to the helium–neon dimer, which is ideal for studying diverse dynamical effects. We show that while vibrational dynamics can slightly reduce ICEC efficiency, ICEC remains dominant over photorecombination and can trigger dimer dissociation. Accounting for the nuclear motion also enables to describe the broadening of the electron spectrum and enables evaluation of temperature-dependent cross sections—capabilities beyond the reach of fixed-nuclei approaches.

I. INTRODUCTION

The capture of free electrons by atoms, ions, molecules, and quantum dots is a fundamental process with wide-ranging implications in both basic and applied sciences. It plays a key role in astrophysics and plasma physics, where it influences stellar processes and ionized gases.[1,2] Furthermore, electron capture is critical for understanding electrochemical and photochemical reactions, impacting biological systems[3] and solid-state technologies.[4]

One such electron capture mechanism is the interparticle Coulombic electron capture (ICEC) that occurs exclusively in systems embedded within an environment.[5] In ICEC, a free electron is captured by an electron acceptor (A), which in this work will be a cation, while the excess energy is transferred via Coulomb interaction to a neighboring electron donor (D), leading to the ionization of D,

$$e_k^- + \mathrm{A} + \mathrm{D} \rightarrow \mathrm{A}^- + \mathrm{D}^+ + e_{k'}^-. \tag{1}$$

This environment-mediated coupling significantly enhances the probability of electron capture across various systems, as shown in theoretical studies.[6,7] A detailed overview of the mechanism and its theoretical basis can be found in Ref. 8.

In most earlier studies, theoretical approaches to investigate ICEC have assumed static nuclei, neglecting the influence of nuclear dynamics.[8] However, recent results[9] reveal that nuclear motion, particularly vibrational dynamics, can substantially affect the efficiency and outcome of the process. Findings for related processes, such as

resonant two-center photoionization[10] and two-center dielectronic recombination,[11] further support the importance of nuclear motion in interparticle electron capture. These findings highlight the necessity of incorporating nuclear dynamics into ICEC models to achieve a more complete theoretical understanding.

In this work, we extend the previous analytical energy and electron transfer model[6,12] of ICEC by explicitly incorporating the relative nuclear motion between the interacting partners, providing intuitive insights grounded in the physical characteristics of the individual systems. We apply this approach to the positively charged helium–neon dimer and benchmark our results against the adiabatic-nuclei approximation based on fixed-nuclei *ab initio* R-matrix calculations, which offer a rigorous quantum mechanical treatment of ICEC as a scattering process.[13,14] Using both approaches, we assess the impact of nuclear dynamics on ICEC and aim to provide theoretical guidance for future experimental efforts.

This paper is organized as follows: we first establish the theoretical framework in Sec. II, incorporating nuclear degrees of freedom into the analytical model of ICEC. In Sec. III, we describe the approximations taken to include nuclear dynamics into the R-matrix approach. Section IV describes the physical parameters of our example of a weakly bound system, the positively charged helium–neon dimer. Section V outlines the computational details. The results for the ICEC cross sections of the helium–neon dimer are discussed in Sec. VI. Finally, we summarize our findings and their implications in Sec. VII. We use atomic units ($\hbar = m_e = e = 1$) throughout this paper, unless explicitly mentioned otherwise.

II. NUCLEAR DYNAMICS IN THE ANALYTICAL ENERGY AND ELECTRON TRANSFER MODEL OF ICEC

From a scattering theory perspective, ICEC is a multichannel inelastic process in which an incoming electron interacts with a target.[6,15] It is characterized by a cross section that quantifies its probability for a given electron energy. Our goal is to derive an approximation to the ICEC cross section that includes nuclear dynamics.

We consider the process in Eq. (1), where an electron is captured by an electron acceptor A and a neighboring electron donor D emits an electron. Both species can be atoms, molecules, or ions. The corresponding differential cross section is

$$\frac{\mathrm{d}\sigma}{\mathrm{d}\Omega_{\mathbf{k}'}} = \frac{1}{(2\pi)^2}\frac{k'}{k}|M|^2, \tag{2}$$

where $\Omega_{\mathbf{k}'}$ is the solid angle of the outgoing electron and M is the transition matrix element,[6,15] in our case between two vibronic states Ψ_α accounting for the vibrational dynamics between A and D. We describe the vibronic states as a single term of the Born–Huang expansion,[16,17]

$$|\Psi_\alpha(\mathbf{r}, R)\rangle = |\phi_\alpha(\mathbf{r}\,; R)\rangle\,|\nu_\alpha(R)\rangle, \tag{3}$$

where ϕ_α is the electronic wave function, ν_α is the nuclear wave function, $\mathbf{r}$ are the electronic coordinates, and R is the distance between the centers of mass of A and D.

As shown in Ref. 12, the antisymmetry of the electronic wave function leads to two distinct contributions to M,[15]

$$M(\mathbf{k}' \leftarrow \mathbf{k}) = M_{\mathrm{el}}(\mathbf{k}' \leftarrow \mathbf{k}, e^-_k = e^-_{k'}) + M_{\mathrm{en}}(\mathbf{k}' \leftarrow \mathbf{k}, e^-_k \neq e^-_{k'}). \tag{4}$$

The electron transfer term, M_{el}, assumes the incoming and outgoing electrons are the same and describes direct scattering accompanied by electron relocation from donor to acceptor. The energy transfer term, M_{en}, involves capture of the incoming electron by A, with excess energy transferred to D, which emits an electron.

These two mechanisms dominate at different distances between the two particles: electron transfer requires short-range interactions, while energy transfer remains effective even at larger separations.[18] In the following, we focus on incorporating nuclear dynamics into the energy transfer contribution before turning to electron transfer.

A. Energy transfer contribution to ICEC

For the energy transfer contribution M_{en}, we extend the derivation from Refs. 5 and 6, incorporating the necessary modifications to account for nuclear motion. Here, we treat the process as events taking place separately on A and D, linked by the energy transfer via first order of perturbation theory. This approach is referred to as "asymptotic" or "virtual photon" approximation in the literature.[8] We will see that this enables us to express the cross section in terms of physical parameters of A and D,[5,6] which can be found in the literature or obtained from experiments.

We begin by approximating the initial (i) and final (f) electronic wave functions as products of the individual states of A and D,

$$\begin{aligned} |\phi_i\rangle &= |\phi_{\mathrm{A},\mathbf{k}}\rangle|\phi_{\mathrm{D}}\rangle, \\ |\phi_f\rangle &= |\phi_{\mathrm{A}^-}\rangle|\phi_{\mathrm{D}^+,\mathbf{k}'}\rangle, \end{aligned} \tag{5}$$

where the energy-normalized state $\phi_{\mathrm{A},\mathbf{k}}$ ($\phi_{\mathrm{D}^+,\mathbf{k}'}$) describes A ($\mathrm{D}^+$) together with the incoming (outgoing) electron of momentum $\mathbf{k}$ ($\mathbf{k}'$).[5] This is justified if A and D are far enough away from each other and the electronic interaction between them can be assumed to be weak.

By using Eqs. (5) and (3) and employing the Born–Oppenheimer approximation, the transition matrix element within the first order of perturbation theory for a single initial and final state is

$$M_{\mathrm{en}} = \langle \nu_f |\, \langle \phi_{\mathrm{A}^-}|\langle \phi_{\mathrm{D}^+,\mathbf{k}'}|\, \hat{V}\, |\phi_{\mathrm{A},\mathbf{k}}\rangle|\phi_{\mathrm{D}}\rangle\, |\nu_i\rangle, \tag{6}$$

where $\hat{V}$ is the Coulomb interaction between the charges of the two systems and ν_i (ν_f) is the nuclear wave function of the initial (final) state according to Eq. (3).

For sufficiently large distance R between A and D, we expand $\hat{V}$ in a Taylor series around R and retain the leading term that yields a non-zero contribution to the transition matrix element M_{en}. This term corresponds to the dipole–dipole interaction of the two charge densities,

$$\hat{V}_{\mu\mu} = \frac{1}{R^3}\left(\hat{\boldsymbol{\mu}}_{\mathrm{A}} \cdot \hat{\boldsymbol{\mu}}_{\mathrm{D}} - 3\,(\mathbf{u}_R \cdot \hat{\boldsymbol{\mu}}_{\mathrm{A}})\,(\mathbf{u}_R \cdot \hat{\boldsymbol{\mu}}_{\mathrm{D}})\right), \tag{7}$$

where $\mathbf{u}_R$ is the unit vector pointing from A into the direction of D. As the electronic dipole moment operators $\hat{\boldsymbol{\mu}}_{\mathrm{A}}$ and $\hat{\boldsymbol{\mu}}_{\mathrm{D}}$ of A and D are independent of R, we can separate the integration over electronic and nuclear coordinates.

Substituting Eqs. (6) and (7) into Eq. (2) yields the differential cross section in the lowest-order approximation for the energy transfer contribution to ICEC,

$$\frac{d\sigma}{d\Omega_{\mathbf{k}'}} = \frac{1}{(2\pi)^2}\frac{k'}{k}\left|\left[\boldsymbol{\mu}_A\cdot\boldsymbol{\mu}_D - 3\,(\mathbf{u}_R\cdot\boldsymbol{\mu}_A)\,(\mathbf{u}_R\cdot\boldsymbol{\mu}_D)\right]\langle v_f|R^{-3}|v_i\rangle\right|^2, \tag{8}$$

where $\boldsymbol{\mu}_A = \langle\phi_{A^-}|\,\hat{\boldsymbol{\mu}}_A\,|\phi_{A,\mathbf{k}}\rangle$ and $\boldsymbol{\mu}_D = \langle\phi_{D^+,\mathbf{k}'}|\,\hat{\boldsymbol{\mu}}_D\,|\phi_D\rangle$ are the electronic transition dipole moments. To obtain the total cross section, Eq. (8) is integrated over the solid angle $\Omega_{\mathbf{k}'}$ of the outgoing electron and averaged over the incoming electron angle $\Omega_{\mathbf{k}}$. To facilitate this integration, one expands the plane waves in the initial and final states in terms of spherical waves.[5,19]

The dipole transition moments involved in the process can be related to the corresponding photorecombination (PR) and photoionization (PI) cross sections. The PR cross section of the electron acceptor A is given by[19]

$$\sigma_A^{PR}(\varepsilon) = \frac{4\pi^2\omega^3}{3c^3k^2}\,|\boldsymbol{\mu}_A|^2, \tag{9}$$

where c is the speed of light and ε is the kinetic energy of the incoming electron, corresponding to momentum k. The quantity ω is the energy of the emitted photon, corresponding here to the excess energy of the electron capture. Its value is given by the sum of ε and the electron attachment energy of A, which is equal to the ionization potential of A^-, IP_{A^-}.

Similarly, the PI cross section for the electron donor D is[19]

$$\sigma_D^{PI}(\omega') = \frac{4\pi^2\omega'}{3c}\,|\boldsymbol{\mu}_D|^2, \tag{10}$$

where ω' corresponds to the energy available to ionize D. The difference of ω' and ω is $\Delta\omega_{fi} = E_f - E_i$, where E_i (E_f) is the energy of the initial (final) vibrational state of the dimer. As a result, the kinetic energy of the outgoing electron is

$$\varepsilon' = \omega - \Delta\omega_{fi} - IP_D, \tag{11}$$

where IP_D is the ionization potential of the electron donor D.

Using these two expressions, we arrive at an approximation to the energy-transfer contribution to the ICEC cross section for the transition from vibrational state $|v_i\rangle$ of AD to vibrational state $|v_f\rangle$ of A^-D^+,

$$\sigma(k, v_i \to v_f) = \frac{3c^4}{4\pi}\,\frac{\sigma_A^{PR}(\varepsilon)\,\sigma_D^{PI}(\omega-\Delta\omega_{fi})}{\omega^3(\omega-\Delta\omega_{fi})}\,\left|\langle v_f|R^{-3}|v_i\rangle\right|^2. \tag{12}$$

Having established a working expression for the energy transfer contribution to ICEC, we now turn our attention to the electron transfer mechanism.

B. Electron transfer contribution to ICEC

For the electron transfer contribution M_{el}, we extend the derivation from Ref. 12, modifying to account for nuclear motion, analogously to Sec. II A. In this approach, the overlap of the electronic wave functions is not neglected, but instead approximated by the overlap of two Gaussians.[12,20–22]

In the electron transfer contribution, we assume that we can distinguish the scattering electron from the bound electrons of (AD). We further assume that we can treat the interaction of the continuum electron and the target as a simple interaction of charge distributions, neglecting electron correlation. We can then write our initial and final electronic states as

$$\begin{aligned}|\phi_i\rangle &= |\phi_{AD}\rangle|\mathbf{k}+\rangle,\\ |\phi_f\rangle &= |\phi_{A^-D^+}\rangle|\mathbf{k}'-\rangle,\end{aligned} \tag{13}$$

where ϕ_{AD} ($\phi_{A^-D^+}$) is the electronic wave function of the dimer and $\mathbf{k}$ ($\mathbf{k}'$) is the initial (final) momentum vector of the continuum electron. We denote with + (−) the incoming (outgoing) scattering state,[15] where the continuum electron scatters off of AD (A^-D^+).

Although we do not consider the electrons of A and D as distinguishable, the electron correlation between them can still be treated as a perturbation. Applying Eqs. (3) and (13) within the Born–Oppenheimer approximation, the transition matrix element at first order of perturbation theory for a single initial and final state is given by

$$M_{el} = \left\langle v_f\right|\,\langle\mathbf{k}'-|\langle\phi_{A^-D^+}|\,\hat{V}\,|\phi_{AD}\rangle|\mathbf{k}+\rangle\,\left|v_i\right\rangle, \tag{14}$$

where $\hat{V}$ is the Coulomb interaction between electrons situated on A (including the incoming electron) and on D, and now, ϕ neglects the correlation between electrons on A and D as the zero-order wave function.

We can again apply the multipole expansion to $\hat{V}$ [cf. Eq. (7)], but the lowest contributing order is now the R^{-1} term, as we assume the wavefunctions of A and D to have a nonzero overlap. We obtain the transition matrix element as

$$M_{el} = \left\langle v_f\right|\,\frac{\langle\phi_{A^-D^+}|\phi_{AD}\rangle\,\langle\mathbf{k}'-|\mathbf{k}+\rangle}{R}\,\left|v_i\right\rangle. \tag{15}$$

Assuming a single Slater determinant for the initial and final electronic states of the dimer, the overlap $\langle\phi_{A^-D^+}|\phi_{AD}\rangle$ reduces to the product of the virtual orbital of A, which accepts an electron, ϕ_α^A, and the orbital of D, which donates said electron, ϕ_δ^D. Approximating these two orbitals as Gaussians of widths a_A and a_D results in the following expression for the overlap:[12]

$$S_{AD}(R) = \langle\phi_\alpha^A|\phi_\delta^D\rangle = \left(\frac{a_A a_D}{a_A^2+a_D^2}\right)^{3/2}\exp\left(-\frac{R^2}{2(a_A^2+a_D^2)}\right). \tag{16}$$

Note that the true overlap of the two orbitals can vanish due to their symmetries.

Now, let us gather the results for the approximation to the differential cross section of the electron transfer path of ICEC by substituting Eq. (15) into Eq. (2),

$$\frac{d\sigma}{d\Omega_{\mathbf{k}'}} = \frac{1}{(2\pi)^2}\frac{k'}{k}\left|\left\langle v_f\right|\,\frac{S_{AD}\,\langle\mathbf{k}'-|\mathbf{k}+\rangle}{R}\,\left|v_i\right\rangle\right|^2. \tag{17}$$

To obtain the total cross section σ, we integrate Eq. (17) over the solid angle $\Omega_{\mathbf{k}'}$ of the outgoing electron. The angular dependence enters only through the overlap of the incoming and outgoing scattering states, $\langle\mathbf{k}'-|\mathbf{k}+\rangle$. Assuming the potential of the dimer can be

approximated by its spherical component, we employ a partial wave expansion of the scattering states,[15] leading to

$$\langle \mathbf{k}' - |\mathbf{k}+\rangle = \frac{1}{2\pi^2 k k'} \int_0^\infty \mathrm{d}r \sum_{\ell=0}^{\infty} (2\ell+1)\, \psi^{-}_{\ell\mathbf{k}'}{}^{*}(r,R) \times \psi^{+}_{\ell\mathbf{k}}(r,R) P_\ell(\hat{\mathbf{k}}' \cdot \hat{\mathbf{k}}), \tag{18}$$

where the hat denotes unit vectors, $\psi^{\pm}$ are the radial incoming and outgoing scattering wave functions, and P_ℓ is the Legendre polynomial. The angular parts of this expansion—the Legendre polynomials—do not depend on R, hence we can carry out the integration over $\Omega_{\mathbf{k}'}$. If we then define

$$J_\ell := \int_0^\infty \mathrm{d}r\, \psi^{-}_{\ell\mathbf{k}'}{}^{*}(r,R)\, \psi^{+}_{\ell\mathbf{k}}(r,R), \tag{19}$$

the total cross section reads

$$\sigma_{\mathrm{el}} = 32\pi \frac{1}{\sqrt{\varepsilon^3 \varepsilon'}} \sum_{\ell=0}^{\infty} (2\ell+1) \left| \left\langle v_f \right| S_{\mathrm{AD}}\, J_\ell\, R^{-1} \left| v_i \right\rangle \right|^2, \tag{20}$$

where ε (ε') is the kinetic energy of the incoming (outgoing) electron. Note that compared to Ref. 12, the integral defining J_ℓ is not squared and that we cannot simplify the absolute square further due to the integration over R.

We further assume an exponential decrease in J_ℓ squared, as in Ref. 12,

$$J_\ell^2 \approx C \exp\left(-\frac{\ell(\ell+1)}{K_{AV}^2} \right), \tag{21}$$

where we defined $K_{AV}^2 = (a_A + R)^2 \varepsilon + (a_D + R)^2 \varepsilon'$, and an ad hoc dependence of C on $\varepsilon' - \varepsilon$,

$$C \approx \overline{C} \exp\left(-\frac{|\varepsilon' - \varepsilon|}{d} \right), \tag{22}$$

where $\overline{C}$ and d are fitting parameters taken from Ref. 12.

With both the energy and electron transfer contributions established for a single vibrational transition, let us summarize the results.

C. Final considerations of the analytical energy and electron transfer model

In our model, the total ICEC cross section is given by the sum of energy and electron transfer contributions,

$$\sigma = \sigma_{\mathrm{en}} + \sigma_{\mathrm{el}}, \tag{23}$$

with expressions provided in Eqs. (12) and (20), respectively. Although these mechanisms could, in principle, interfere, their transition amplitudes are only comparable over a narrow range of R.[12] Since the integration spans all internuclear distances, their direct interference contributes only marginally and an incoherent sum of cross sections is appropriate.

So far, we have considered only a single vibrational transition. In practice, ICEC involves transitions to multiple bound and dissociative final states. For the former, we sum over all final vibrational states v_f, and for the latter, we integrate over the dissociation energy E,

$$\sigma(k, v_i) = \sum_f \sigma(k, v_i \to v_f) + \int_{E=0}^{E_{\max}} \frac{\mathrm{d}\sigma}{\mathrm{d}E}(k, v_i \to E)\, \mathrm{d}E, \tag{24}$$

where $E_{\max} = \omega - \mathrm{IP_D} + E_i$ is the maximum dissociation energy allowed by energy conservation, corresponding to the limit of $\varepsilon' = 0$.

To account for a thermal population in the initial state, we average over initial vibrational states using a Boltzmann distribution, which introduces temperature dependence,

$$\sigma(k, T) = \frac{1}{\sum_i e^{-E_i/(k_B T)}} \sum_i e^{-E_i/(k_B T)} \sigma(k, v_i), \tag{25}$$

where E_i is the energy of vibrational state v_i, T is the thermodynamic temperature, and k_B is the Boltzmann constant. This temperature dependence is a key feature of our model, made possible by explicitly including nuclear motion.

With this theoretical foundation, we now turn to the R-matrix approach.

III. NUCLEAR DYNAMICS IN THE R-MATRIX APPROACH

We aim to compare the results of the semi-empirical model introduced in Sec. II with a more rigorous approach. We calculate the cross section for the vibronic transitions using an approximation building upon the fixed-nuclei scattering T-matrix. We evaluate this T-matrix using the *ab initio* R-matrix method,[23,24] which is well suited for low-energy electron–molecule scattering calculations. The fixed-nuclei cross section is given in terms of the T-matrix as[24]

$$\sigma_{i\to f}(\varepsilon; R) = \frac{\pi}{k^2} \sum_{lml'm'} |T_{ilm\to f l'm'}(\varepsilon, \varepsilon'; R)|^2, \tag{26}$$

where l, m (l', m') denote all the contributing partial waves of the incoming (outgoing) electron.

We employ the adiabatic-nuclei (AN) approximation[25] to compute the vibrationally resolved scattering cross section. In this approach, the vibrational scattering matrix is constructed as follows:

$$T_{iv_i\to f v_f}(\varepsilon, \varepsilon') = \left\langle v_f | T_{i\to f}(\varepsilon, \tilde{\varepsilon}'; R) | v_i \right\rangle_R. \tag{27}$$

The incoming ε and the outgoing ε' electron energies in the vibrationally resolved picture are related by the conservation of energy [an equivalent of Eq. (11)],

$$\varepsilon + \mathscr{E}_i^{v_i} = \varepsilon' + \mathscr{E}_f^{v_f}, \tag{28}$$

where $\mathscr{E}_i^{v_i}$ ($\mathscr{E}_f^{v_f}$) is the energy of the initial (final) vibronic state. If we define the energy reference as the energy of the final electronic state in the limit of large R, then $\mathscr{E}_f^{v_f} = E_f$. The approximation utilizes the fixed-nuclei on-shell T-matrix, $T_{i\to j}(\varepsilon, \tilde{\varepsilon}'; R)$, where the incoming ε and the outgoing $\tilde{\varepsilon}'$ electron energies are related by the R-dependent conservation of energy,

$$\varepsilon + E_i(R) = \tilde{\varepsilon}' + E_f(R), \tag{29}$$

where $E_i(R)$ $[E_f(R)]$ is the potential energy curve of the initial (final) electronic state. This means that $\tilde{\varepsilon}' \neq \varepsilon'$, i.e., the cross section for a vibronic transition at given outgoing electron energy ε' is calculated from fixed-nuclei data corresponding to a different, in fact R-dependent, outgoing energy $\tilde{\varepsilon}'$. This is because the AN approximation does not take the energy of the vibrational states into account. Nevertheless, it has been used successfully for vibrational,[26] rotational,[27] and electronic[28] excitations and it is valid for electron energies larger than the corresponding excitation thresholds.[25]

In ICEC, dissociation in the final state can be prominent, making the adiabatic-nuclei approximation invalid in a larger range of electron energies above the ICEC threshold. To remedy this, we use the energy-balanced adiabatic-nuclei (EBAN) approximation introduced for calculating electron impact dissociation of H_2 in Ref. 29. In this approximation, we use

$$T_{iv_i \to f v_f}(\varepsilon, \varepsilon') = \left\langle v_f \middle| T_{i\to f}(\tilde{\varepsilon}, \varepsilon'; R) \middle| v_i \right\rangle_R, \tag{30}$$

instead of Eq. (27), and

$$\tilde{\varepsilon} + E_i(R) = \varepsilon' + E_f(R), \tag{31}$$

instead of Eq. (29). In this variant, the vibronic outgoing electron energy coincides with the fixed-nuclei outgoing electron energy, and the non-equivalence is transferred to the incoming electron energies.

So far, we have not specified whether the vibrational states are bound or dissociative. In our study, the initial vibrational states are going to be bound, and in the final state, we consider both bound and dissociative ones. For the bound–bound transitions, Eq. (26) can be readily applied, replacing i by iv_i and f by fv_f. For bound–dissociative transitions, a similar formula holds

$$\frac{\mathrm{d}\sigma_{iv_i \to f v_E}(\varepsilon)}{\mathrm{d}\varepsilon'} = \frac{\pi}{k^2} \sum_{lml'm'} |T_{iv_i lm \to f v_E l'm'}(\varepsilon, \varepsilon')|^2, \tag{32}$$

provided that the dissociative states v_E are energy-normalized.[29,30] We note that for dissociative states, the vibrational energy E_f equals the kinetic energy release (KER).

The dissociative character of the final states also hints at why, in Eq. (30), we should use the correct outgoing electron energy instead of the incoming electron energy. In our case, the fixed-nuclei incoming electron energy $\tilde{\varepsilon}$ differs from the correct one, ε, on the energy scale of the dissociation threshold of the initial electronic state. If we took the correct incoming electron energy, the fixed-nuclei outgoing energy would have differed from the correct one on the scale of the dissociation energy. This discrepancy varies for different ε' with a fixed ε and is severe when most of the energy is released as KER and the outgoing electron is slow. For the ICEC scenarios which correspond to electronic deexcitation, we have to use AN because EBAN introduces an unphysical threshold. An illustration and more detailed discussion of the AN and EBAN cross sections can be found in the supplementary material. Let us also note that for very low incoming electron energy, both AN and EBAN break down. Further work is necessary to properly understand how their performance compares, perhaps by an analytically or numerically exactly solvable model.

With both the analytical model and the R-matrix approach in place, let us introduce the physical system we shall investigate.

TABLE I. Parameters of the surfaces X, A, and B from Ref. 31: equilibrium distance R_e, dissociation energy D_e, harmonic vibrational frequency ω_e, and electronic energy E at equilibrium. The last column denotes corresponding asymptotic ($R \to \infty$) states.

State	R_e (Å)	D_e (cm^{-1})	ω_e (cm^{-1})	E (a.u.)	Asymptotics
$X\ ^2\Sigma^+$	1.43	5200	911	−130.943 49	$He + Ne^+(2p_z^{-1})$
$A\ ^2\Pi_{1/2}$	2.42	283	152	−130.921 76	$He + Ne^+(2p_{x/y}^{-1})$
$B\ ^2\Sigma^+$	2.66	343	152	−130.807 54	$He^+(1s^{-1}) + Ne$

IV. THE SYSTEM STUDIED: $(HeNe)^+$

In the previous sections, we introduced two approaches for calculating vibrationally resolved ICEC cross sections. Section II presented an analytical model extended to include nuclear dynamics, accounting for both energy and electron transfer mechanisms. In Sec. III, we built upon the *ab initio* fixed-nuclei R-matrix results and included the nuclear dynamics using the AN or EBAN approximation, referred to as the R-matrix. We apply both methods to the $(HeNe)^+$ dimer as an example of a weakly bound system.

To contextualize the calculations, we begin with the structural and electronic properties of $(HeNe)^+$. Neon and helium have ionization potentials of 21.56 and 24.59 eV, respectively. Energy conservation implies that when He^+ captures an electron, the electron affinity is sufficient to ionize neon. In contrast, electron capture by Ne^+ requires additional kinetic energy.

Vibrational dynamics are described using Morse potentials for the three lowest electronic states, offering analytic solutions. Parameters from Ref. 31 are used and listed in Table I. Without loss of generality, we assume the dimer is aligned along the z axis. The ground state X asymptotically corresponds to $HeNe^+(2p_z^{-1})$, with

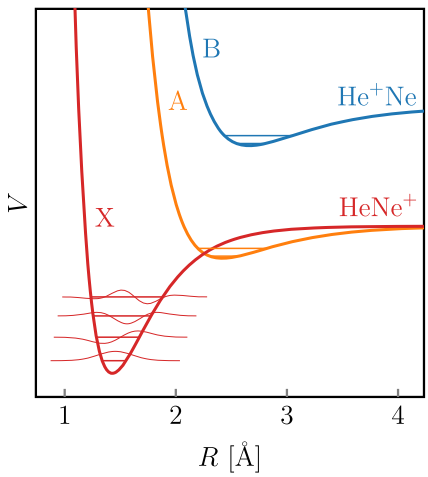

FIG. 1. Schematic potential energy surfaces X, A, and B corresponding to the three lowest electronic states of $(HeNe)^+$. For ease of comparison, surfaces A and B are multiplied by 4 and B is shifted down by 2.5 eV. The figure is taken from E. M. Jahr and J. Šenk (2025). "Influence of vibrational motion and temperature on Interatomic Coulombic electron capture - Figures," Figshare. https://doi.org/10.6084/m9.figshare.28883378.v2.[32] Copyright 2025 Author(s), licensed under a Creative Commons Attribution 4.0 License.

the charge localized on neon, also noted in the last column of Table I. The first excited state A—not to be confused with the electron acceptor—corresponds to $HeNe^+(2p_{x/y}^{-1})$, sharing the same asymptotic energy as X. The second excited state B, $He^+(1s^{-1})Ne$, is the first with the charge on helium.

This system provides an excellent platform for studying a wide range of vibrational effects, as it features potential energy surfaces with distinct characteristics. The excited states A and B are shallower and shifted toward larger internuclear distances compared to X (see Fig. 1), providing a diverse range of conditions found in different physical systems.

V. COMPUTATIONAL DETAILS

In this section, we outline the computational framework used to model ICEC in the $(HeNe)^+$ dimer. We first describe the numerical implementation of the analytical model, followed by the details of the R-matrix calculations.

A. The analytical energy and electron transfer model

To implement the model, we require (i) atomic photoionization cross sections for the energy transfer term in Eq. (12), (ii) Gaussian widths for the electron transfer term in Eq. (20), and (iii) vibrational states of the dimer. The implementation[33] was carried out in Python using the mpmath module,[34] which supports confluent hypergeometric functions with complex arguments—necessary for the dissociative Morse states adopted from Ref. 35.

Photoionization cross sections for He and Ne were taken from Ref. 36. Since the three degenerate $2p$ orbitals in Ne contribute equally under an isotropic field approximation,[19] we divide the total cross section by three: $\sigma_{2p_\ell}^{\mathrm{PI}} = \sigma^{\mathrm{PI}}/3$.

For the electron transfer contribution, we follow Ref. 12, using Gaussian widths in Eq. (16) based on covalent radii[37] scaled by $\alpha = 1.6$. Electron transfer efficiency depends on orbital orientation: in the ground electronic state (X), the $2p_z$ orbital of Ne^+ aligns with the interatomic axis and facilitates the transfer. In the excited A state, the perpendicular $2p_{x/y}$ orbital results in negligible overlap with He's s-orbital, suppressing electron transfer. Consequently, we include electron transfer only in X to B and B to X transitions and restrict A to B and B to A transitions to the energy transfer mechanism.

We use the analytical bound and dissociative solutions of the Morse potential from Ref. 35. Dissociative states are discretized and normalized within a finite box, $R \in (0, 10\ \text{Å}]$. All but the highest bound vibrational state of each electronic state remain well confined within this range. We, therefore, exclude the highest initial bound state due to unreliable overlap with dissociative states in the finite box; this is justified at low temperatures where its population is negligible. Final vibrational states are not restricted, as long as only bound initial states are considered—excluding the highest initial state. Energy-normalized dissociative cross sections are obtained by multiplying the corresponding cross sections from box-normalized dissociative states of energy E_f with the density of states, $\rho(E_f) = 2/|E_{f+1} - E_{f-1}|$.

Unless stated otherwise, we assume the dimer starts in the vibrational ground state of the initial electronic state and sum over all final vibrational states. For fixed-nuclei calculations, the ICEC cross section is evaluated at the equilibrium distance R_e of the initial electronic state.

B. The R-matrix approach

We employed the fixed-nuclei R-matrix method as implemented in the `UKRmol+` suite.[38] Molecular orbitals for the scattering calculations were obtained using the `MOLPRO`[39–41] implementation of the Hartree–Fock method applied to the HeNe system, with the cc-pVDZ basis set. Continuum orbitals were constructed using a radial GTO basis optimized for an R-matrix radius of $a = 13a_0$, as provided in the `UKRmol-scripts` release,[42] and included partial waves up to angular momentum $l = 6$.

As the target orbitals of the scattering model, we used the 1s orbital of Ne as frozen and the 2s, 2p, and 3p orbitals of Ne and the 1s and 2s orbitals of He as active. We included four target states into the scattering calculations, as only those are energetically accessible in the investigated region of scattering energies. The R-matrix was propagated to $r_{\mathrm{af}} = 80a_0$.

We performed the fixed-nuclei R-matrix calculations for interatomic distances ranging from $R = 1.5a_0$ to $R = 9.5a_0$ with a step of $\Delta R = 0.5a_0$. To evaluate the dissociative states, we use the sine discrete variable representation (DVR)[43] in the confinement box $R \in (0, 10\ \text{Å}]$ with 3000 grid points.

We use the AN approximation for the transitions B to X and B to A and the EBAN approximation for the transitions X to B and A to B. The R-integral in Eqs. (27) and (30) for AN and EBAN, respectively, is facilitated using a composite 10-point Gauss–Legendre quadrature.[44,45] Because the dissociative states in the energy range studied can oscillate with high frequencies, it is necessary to interpolate the fixed-nuclei T-matrices because performing the *ab initio* calculations on such a dense grid would be excessively computationally demanding. In the region of energies that we investigate, there are no resonances and the T-matrix elements are smooth both in energy and in R. The cubic spline interpolation[46] is used. The R-quadrature is carried out over the extent of the DVR box. For obtaining the T-matrix values outside the range of the fixed-nuclei calculations, we used linear extrapolation for $R < 1.5a_0$ and $1/R^3$ extrapolation for $R > 9.5a_0$ motivated by the form of the asymptotic approximation[6] to fixed-nuclei ICEC cross sections that is valid in this range. The implementation is available at Ref. 47.

With the computational framework in place, we proceed to analyze the ICEC cross sections for the $(HeNe)^+$ dimer.

VI. RESULTS AND DISCUSSION

In this section, we present the computed ICEC cross sections for the $(HeNe)^+$ dimer, examining how vibrational motion affects the efficiency of electron capture. We compare results from the analytical model[48] and the R-matrix approach,[49] highlighting key trends and deviations.

We begin by discussing the energy transfer and electron transfer contributions to ICEC in Sec. VI A. In Sec. VI B, we investigate the total cross section for ICEC from the ground vibrational state and compare to the transitions from the excited vibrational states. Then, we present the temperature-dependent ICEC cross section in Sec. VI C. Last but not the least, we investigate the spectrum of the outgoing electron for a fixed incoming electron energy in Sec. VI D.

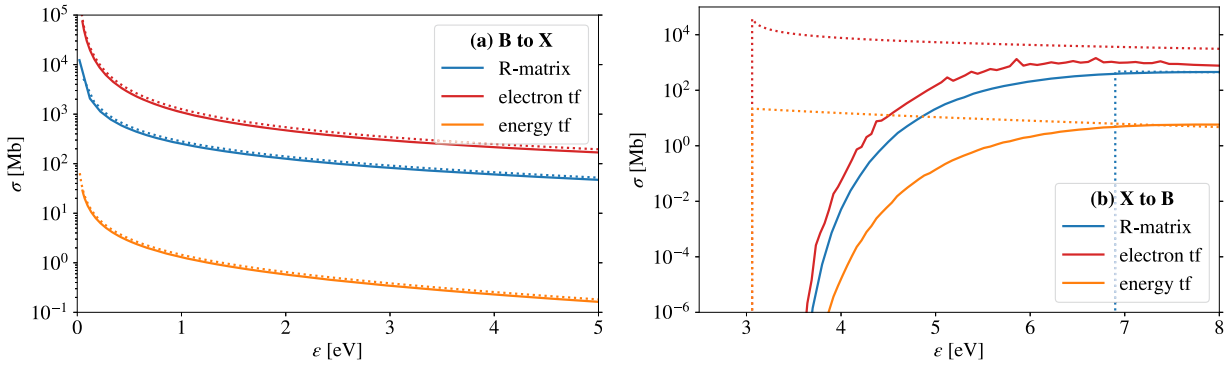

FIG. 2. ICEC cross section vs incoming electron energy ε for $v_i = 0$ from energy transfer (orange), electron transfer (red), and R-matrix (blue). The solid lines indicate nuclear dynamics; the dotted lines indicate fixed-nuclei results. The fixed-nuclei model uses asymptotic energies while R-matrix considers a vertical transition at R_e, resulting in different thresholds for X to B. The figure is taken from E. M. Jahr and J. Šenk (2025). "Influence of vibrational motion and temperature on Interatomic Coulombic electron capture - Figures," Figshare. https://doi.org/10.6084/m9.figshare.28883378.v2.[32] Copyright 2025 Author(s), licensed under a Creative Commons Attribution 4.0 License.

A. Energy vs electron transfer for B to X and X to B

The analytical model, introduced in Sec. II, includes both energy and electron transfer contributions to ICEC. While energy transfer applies to all transitions, electron transfer is only relevant when the state X is involved (see Sec. V A). We, therefore, focus on the B to X and X to B transitions in this chapter.

Figure 2 shows the corresponding ICEC cross sections as a function of the incoming electron energy. The electron transfer contribution (red) dominates over energy transfer (orange) by three

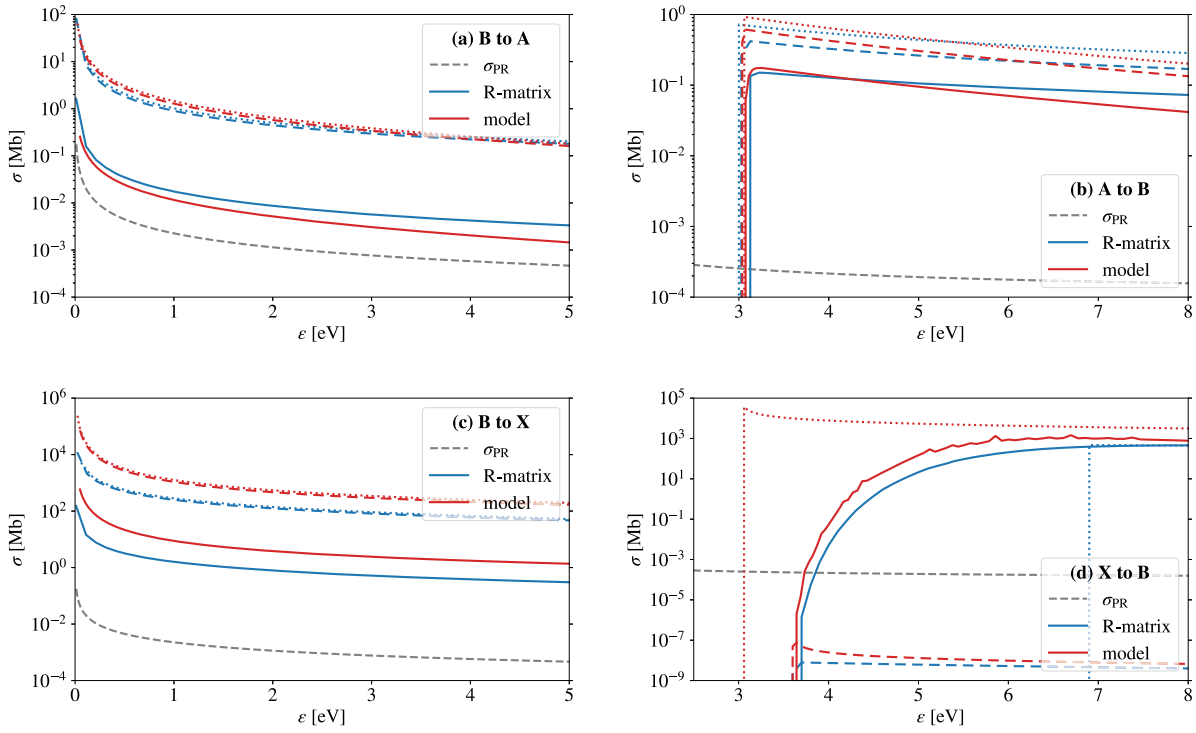

FIG. 3. ICEC cross section vs incoming electron energy ε for $v_i = 0$. Left panel: electron captured by He^+; right panel: captured by Ne^+. R-matrix (blue) and model (red) results: the solid lines represent bound–dissociative, the dashed lines represent bound–bound transitions, and the dotted lines represent fixed-nuclei results. In panels (a) and (c), the dotted and dashed lines nearly coincide. The dashed gray lines represent photorecombination cross sections on the capturing atom. The figure is taken from E. M. Jahr and J. Šenk (2025). "Influence of vibrational motion and temperature on Interatomic Coulombic electron capture - Figures," Figshare. https://doi.org/10.6084/m9.figshare.28883378.v2.[32] Copyright 2025 Author(s), licensed under a Creative Commons Attribution 4.0 License.

orders of magnitude, making it the primary mechanism for these transitions. This dominance stems from the electron transfer being strongly favored at short interatomic distances around R_e.[12] Despite their magnitude difference, both contributions show similar trends with increasing kinetic energy ε.

We compare the analytical model to the R-matrix results (blue), which include both energy and electron transfer contributions. While all curves exhibit the same overall trend, the analytical model is roughly a factor of three larger than the R-matrix results. This discrepancy stems from the electron transfer term, which is exaggerated due to parameter choices in the Gaussian description of the electronic distributions for the $(HeNe)^+$ system.[12]

From here on, we include both energy and electron transfer contributions in the model for the X to B and B to X transitions. We now turn to comparing the total cross section with vibrationally resolved and fixed-nuclei results.

B. Total cross section

Figure 3 presents ICEC cross sections for all electronically distinct processes, comparing the analytical model, the R-matrix, and fixed-nuclei results. Across all cases, the model agrees with the R-matrix approach within an order of magnitude, consistent with the comparisons discussed in Sec. VI A.

Threshold energies differ between channels. When He^+ captures the electron (left panels), the process can occur at zero incoming electron energy due to the high electron affinity of He^+. For the reverse process (right panels), the incoming electron has to supply an energy of 3–4 eV to make ICEC possible.

The relative importance of bound–bound (b–b) and bound–dissociative (b–d) transitions varies by channel. For B to X and B to A (left panels), b–b transitions dominate by about two orders of magnitude, driven by large overlaps between the ground vibrational state of B and bound states of X or A. For A to B, b–b transitions still dominate but only marginally.

In contrast, the X to B process is dominated by b–d transitions—by up to ten orders of magnitude. The suppression of the b–b transitions arises from minimal overlap between the ground state of X and the bound states of B due to the shift in equilibrium distance R, as shown in Fig. 1. The same holds even for low-energy dissociative states but the overlap grows with increasing KER (the energy of the dissociative state), as the turning point moves to smaller R. With larger kinetic energy ϵ, more dissociative states are accessible, enhancing the total cross section. Once the relevant dissociative states are fully accessible, the cross section saturates and eventually decreases due to the kinetic energy dependence.

Comparison with fixed-nuclei results calculated at the equilibrium distance of the initial electronic state (dotted lines) reveals the impact of nuclear dynamics. For transitions B to A, B to X, and A to B, the fixed-nuclei cross sections are comparable with the dominant b–b or b–d contribution. For A to B, the agreement in magnitude is within a factor of two across the full energy range.

The X to B transition, however, shows a significant discrepancy in threshold between the fixed-nuclei and vibrationally resolved cross sections. This stems from different energy conservation assumptions: the fixed-nuclei model (dotted red) uses asymptotic energy conservation, $\epsilon' = \epsilon + \mathrm{IP}_{A^-} - \mathrm{IP}_D$,[6] leading to a threshold energy of 3.02 eV for X to B, while the fixed-nuclei R-matrix (dotted blue) uses vertical transitions at R_e, shown in Eq. (29), corresponding to 6.9 eV. Both the model and R-matrix approaches for including nuclear dynamics instead conserve the vibronic energy, Eq. (11), yielding a more gradual onset of the cross section.

In all cases, the dominant ICEC cross section—whether b–b or b–d—surpasses the photorecombination cross section of the capturing ion by at least three orders of magnitude. For the X to B transition, the enhancement reaches up to six orders of magnitude, highlighting the efficiency of ICEC and its significant role in environments where low-energy electrons and weakly bound systems are present.

C. Temperature dependence

To model ICEC realistically, the thermal population of initial vibrational states must be considered. Unlike fixed-nuclei methods, our approach includes vibrational averaging via a Boltzmann distribution, introducing temperature dependence into the cross sections, as outlined in Sec. II C.

We show in Fig. 4 how the ICEC cross section for $(HeNe)^+$ changes with increasing incoming electron energy for different temperatures. For the B to X, A to B, and B to A transitions, increasing

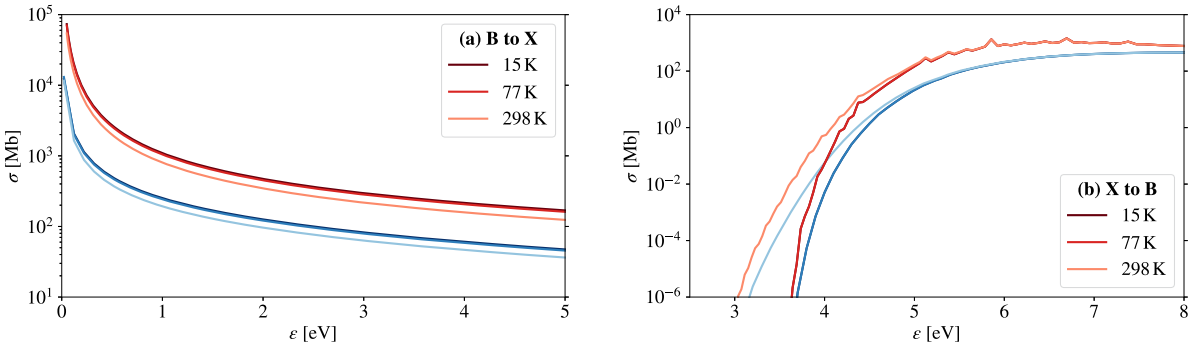

FIG. 4. Temperature-dependent ICEC cross section vs incoming electron energy ε. Shades of blue: the R-matrix; shades of red: the model. Lighter shades correspond to higher temperatures. The curves for $T = 15$ and 77 K coincide in the right panel. The figure is taken from E. M. Jahr and J. Šenk (2025). "Influence of vibrational motion and temperature on Interatomic Coulombic electron capture - Figures," Figshare. https://doi.org/10.6084/m9.figshare.28883378.v2.[32] Copyright 2025 Author(s), licensed under a Creative Commons Attribution 4.0 License.

the temperature to $T = 298$ K results in a reduction in the total cross section. For instance, in the B to X transition (panel 4a), the asymptotic model predicts a decrease of up to a factor of 1.4 when comparing 298 K (orange) with 15 K (red). This trend is also observed in the R-matrix calculations (blue). The decrease stems from significant population of excited vibrational states at higher temperatures and for these transitions, excited initial states yield lower cross sections. A detailed analysis of this vibrational-state dependence is provided in the supplementary material.

In contrast, the X to B transition [panel Fig. 4(b)] exhibits the opposite behavior. At low incoming electron energies, the cross section increases with temperature. This enhancement is due to the strong contribution from higher initial vibrational states, which, in this case, produce substantially larger cross sections in the low-energy regime due to lowering the threshold and enhancing the overlap between initial and final vibrational wave functions. More details can be found in the supplementary material. At higher electron energies, where the dependence on the initial vibrational state becomes weaker, the temperature effect diminishes and the cross section remains nearly unchanged.

Moreover, for X to B, we observe a lowering of the ICEC threshold with increasing temperature. This is a direct consequence of the reduced threshold energies associated with vibrationally excited initial states, which begin to dominate the vibrational average at higher temperatures.

D. Spectrum

Nuclear dynamics significantly impacts the spectrum of the outgoing electron in ICEC. At fixed incident electron energy, the spectrum features discrete peaks from bound–bound transitions and a continuum from bound–dissociative transitions.

Figure 5 presents the outgoing electron energy spectra for all ICEC processes considered, assuming initial ground vibrational states. We use $\varepsilon = 1$ eV (He^+ as acceptor) and $\varepsilon = 5$ eV (Ne^+ as acceptor). The line part of the spectrum denotes bound–bound transitions, with the signal of the highest outgoing electron energy corresponding to the ground vibrational final state; the continuous curves represent bound-dissociative contributions. Energy conservation links the outgoing electron energy to the final vibrational state, shown in the secondary x axis at the top of the plots. Spectra are truncated below $10^{-3} \times \sigma_{PR}$ due to experimental irrelevance.

For A to B, B to A, and B to X, bound–dissociative cross sections decrease with increasing KER, often with modulations. This behavior persists for higher initial vibrational states (see the supplementary material). For X to B, by contrast, the

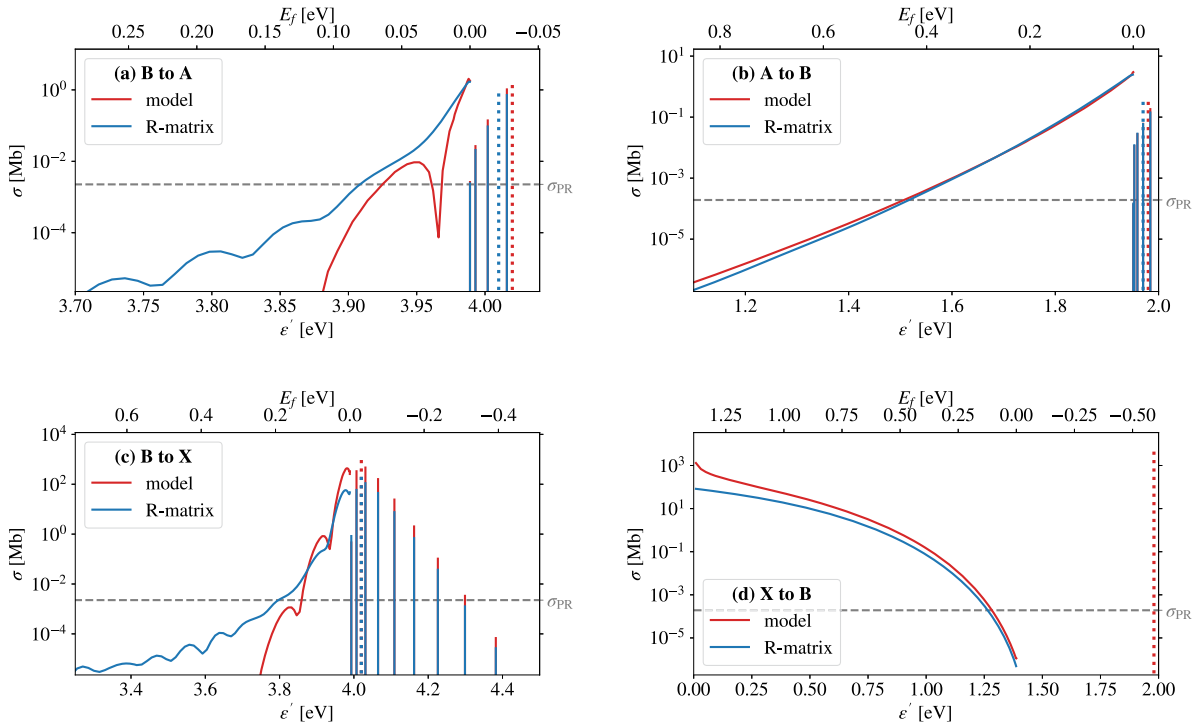

FIG. 5. ICEC cross section vs outgoing electron energy ε' for $\nu_i = 0$. Each panel shows a different electronic ICEC process: left for He^+ ($\varepsilon = 5$ eV), right for Ne^+ ($\varepsilon = 1$ eV). The line spectrum denotes bound–bound transitions and the solid curves represent bound–dissociative differential cross sections in Mb eV^{-1}; see Eqs. (24) and (32). R-matrix (blue), model (red), photorecombination reference (dashed gray), and fixed-nuclei data (dotted line spectrum) are included. In panel (d), the fixed-nuclei ICEC channel is closed for the R-matrix result and, therefore, not represented. The figure is taken from E. M. Jahr and J. Šenk (2025). "Influence of vibrational motion and temperature on Interatomic Coulombic electron capture - Figures," Figshare. https://doi.org/10.6084/m9.figshare.28883378.v2.[32] Copyright 2025 Author(s), licensed under a Creative Commons Attribution 4.0 License.

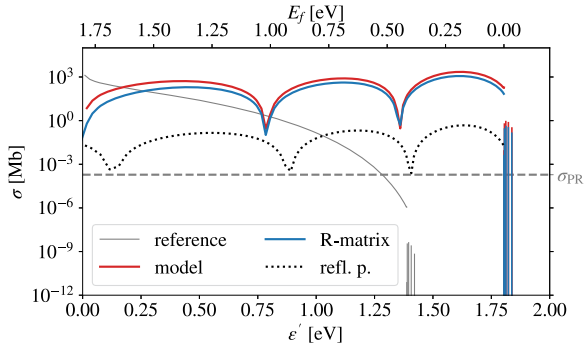

FIG. 6. ICEC cross section vs outgoing electron energy ε' for X to B. Ne^+ captures the incident electron with a kinetic energy of $\varepsilon = 5$ eV. The initial vibrational state is $v_i = 5$. The dotted curve represents the reflection principle prediction of the cross section. The reference (gray curve) shows the model data for $v_i = 0$ [i.e., from panel Fig. 5(d)]. The blue and red lines are as in Fig. 5. The figure is taken from E. M. Jahr and J. Šenk (2025). "Influence of vibrational motion and temperature on Interatomic Coulombic electron capture - Figures," Figshare. https://doi.org/10.6084/m9.figshare.28883378.v2.[32] Copyright 2025 Author(s), licensed under a Creative Commons Attribution 4.0 License.

bound–dissociative cross section increases rapidly with KER. Higher v_i introduce modulations, with an increasing number of minima.

Note that in Fig. 5(d) (X to B), the discrepancy between the energy conservations discussed in Sec. VI B manifests in the fixed-nuclei ICEC channel being closed for the R-matrix approach and open for the analytical model. The fixed-nuclei R-matrix result is, therefore, not represented in this spectrum.

Figure 6 compares X to B spectra for $v_i = 0$ and $v_i = 5$. Three key differences arise: (i) the entire spectrum for $v_i = 5$ is shifted by ~ 0.4 eV due to the initial vibrational energy difference; (ii) bound–bound cross sections increase by eight orders of magnitude for $v_i = 5$, due to enhanced overlap with final bound states at larger R; and (iii) the dissociative spectrum for $v_i = 5$ shows multiple peaks and valleys, in contrast to the monotonic shape for $v_i = 0$.

This structure can be qualitatively explained using the reflection principle.[50] By projecting the initial vibrational state's density, weighted by the electron transfer interaction $\propto \exp\left(-cR^2\right)/R^2$, Eqs. (16) and (20), we reproduce the overall shape and nodal structure of the cross section. However, the predicted peak positions are systematically shifted to higher ε', likely due to the approximation of the final-state potential by its linear component at the turning point within the reflection principle approximation.

Finally, we compare the analytical model and the R-matrix results. Overall, the model cross sections agree well with the R-matrix results—both in magnitude and qualitative behavior. They show consistent trends and magnitudes for the bound–bound spectra and similarly capture the shape of the bound–continuum transitions. The largest discrepancies occur in bound–dissociative transitions with He^+ as electron acceptor: the model predicts more pronounced oscillations and shows a faster decay with increasing KER compared to the R-matrix results. These differences likely arise from limitations of the model, including the neglect of higher-order multipole terms and interference between energy and electron transfer mechanisms. The reliability of the R-matrix approach, on the other hand, is affected by the use of the AN approximation in B to X and B to A, which becomes less accurate at higher KER.

VII. CONCLUSION

We have presented a comprehensive theoretical investigation of how nuclear motion influences the ICEC cross section in the positively charged helium-neon dimer—an example of a weakly bound system. In our approach, we incorporate vibrational dynamics into an analytical model of ICEC, including both the energy and electron transfer mechanisms in terms of a semi-empirical model. To validate the model, we implemented an approximation based on fixed-nuclei *ab initio* R-matrix results, finding agreement within an order of magnitude. Beyond this quantitative agreement, the model also reproduces the qualitative behavior and offers valuable interpretative insight.

Our results demonstrate that including nuclear motion and temperature dependence leads to important modifications of the ICEC cross sections. These include changes in threshold position, threshold behavior, energy dependence, outgoing electron energy, and overall magnitude. When the neon cation captures the incoming electron, the cross section rises near the threshold and is predominantly followed by dissociation at higher electron energies— tendency that becomes even more pronounced at elevated temperatures. In contrast, electron capture by the helium cation favors bound–bound transitions, with slightly reduced cross sections observed at lower temperatures. We find that electron transfer dominates the cross section, as the bound vibrational states are localized in the short-range region where the asymptotic energy-transfer approximation breaks down. Although nuclear motion can slightly reduce the total cross section compared to fixed-nuclei calculations at equilibrium geometries, ICEC remains several orders of magnitude more efficient in the helium–neon dimer than photorecombination, reinforcing its physical relevance.

It is important to note that, although we treat the electronic states X and A as distinct within our theoretical framework, such separation may not be feasible experimentally due to limited resolution, which could obscure individual contributions. In addition, while our treatment neglects molecular rotations, their inclusion would introduce further fine structure in the bound–bound transitions. However, resolving this substructure would be experimentally challenging, as the energy splitting between rotational states within the same vibrational level is minimal.

The influence of nuclear dynamics on ICEC has important implications for both theoretical modeling and experimental detection. Our results highlight the need for including this dynamics into ICEC descriptions, particularly in molecular and weakly bound systems.

SUPPLEMENTARY MATERIAL

The supplementary material provides the ICEC cross sections for higher initial vibrational states, which underlie the temperature dependence discussed in Sec. VI C. We further show the cross sections for different temperatures for all electronic transitions, as well as the spectra for higher initial vibrational states. We also show a comparison of the AN and EBAN cross sections in two example cases.

ACKNOWLEDGMENTS

We acknowledge the DFG-ANR for providing financial support through the QD4ICEC project. The corresponding Grant Nos. are FA 1989/1-1 and ANR-22-CE92-0071-01. E.F. and E.M.J. acknowledge the Zentrum für Frankophone Welten at the University of Tübingen for a travel grant; furthermore, E.F. acknowledges funding by LISA$^+$ at the University of Tübingen. J.P.D. acknowledges financial support from the COST Action CA18212–Molecular Dynamics in the GAS phase (MD-GAS), supported by COST (European Cooperation in Science and Technology).

AUTHOR DECLARATIONS

Conflict of Interest

The authors have no conflicts to disclose.

Author Contributions

Elena M. Jahr: Conceptualization (equal); Formal analysis (equal); Investigation (equal); Methodology (lead); Software (lead); Visualization (equal); Writing – original draft (equal); Writing – review & editing (supporting). **Jan Šenk**: Conceptualization (equal); Formal analysis (equal); Investigation (equal); Methodology (supporting); Software (supporting); Visualization (equal); Writing – original draft (equal); Writing – review & editing (supporting). **Jan P. Drennhaus**: Methodology (supporting); Writing – review & editing (supporting). **Přemysl Kolorenč**: Methodology (equal); Supervision (supporting); Writing – review & editing (equal). **Nicolas Sisourat**: Conceptualization (lead); Funding acquisition (equal); Methodology (equal); Project administration (equal); Supervision (equal); Writing – review & editing (equal). **Elke Fasshauer**: Conceptualization (lead); Funding acquisition (equal); Methodology (lead); Project administration (equal); Supervision (equal); Writing – review & editing (lead).

DATA AVAILABILITY

The data that support the findings of this study are openly available and cited at the appropriate locations within this paper.

REFERENCES

[1] W. H. Tucker, *Radiation Processes in Astrophysics* (The MIT Press, 1978).
[2] G. Visentin, S. Schippers, and S. Fritzsche, Astron. Astrophys. **679**, A13 (2023).
[3] J. Narayanan S J, D. Tripathi, P. Verma, A. Adhikary, and A. K. Dutta, ACS Omega **8**, 10669 (2023).
[4] T. N. Morgan, Phys. Rev. B **28**, 7141 (1983).
[5] K. Gokhberg and L. S. Cederbaum, Phys. Rev. A **82**, 052707 (2010).
[6] K. Gokhberg and L. S. Cederbaum, J. Phys. B: At., Mol. Opt. Phys. **42**, 231001 (2009).
[7] A. Molle, O. Zatsarinny, T. Jagau, A. Dubois, and N. Sisourat, J. Chem. Phys. **158**, 134306 (2023).
[8] A. Bande, E. Fasshauer, A. Molle, D. Peláez, F. M. Pont, and N. Sisourat, J. Phys. B: At., Mol. Opt. Phys. **56**, 232001 (2023).
[9] F. M. Pont, A. Bande, E. Fasshauer, A. Molle, D. Peláez, and N. Sisourat, Phys. Rev. A **110**, 042804 (2024).
[10] F. Grüll, A. B. Voitkiv, and C. Müller, Phys. Rev. A **102**, 012818 (2020).
[11] J. P. Drennhaus, A. Molle, J. Šenk, E. Jahr, E. Fasshauer, F. M. Pont, and N. Sisourat, Phys. Rev. A **111**, 032810 (2025).
[12] J. Šenk, V. Graves, J. D. Gorfinkiel, P. Kolorenč, and N. Sisourat, J. Chem. Phys. **161**, 174113 (2024).
[13] N. Sisourat, T. Miteva, J. D. Gorfinkiel, K. Gokhberg, and L. S. Cederbaum, Phys. Rev. A **98**, 020701 (2018).
[14] A. Molle, A. Dubois, J. D. Gorfinkiel, L. S. Cederbaum, and N. Sisourat, Phys. Rev. A **104**, 022818 (2021).
[15] J. R. Taylor, *Scattering Theory: The Quantum Theory of Nonrelativistic Collisions* (Courier Corporation, 2006).
[16] C. J. Ballhausen and A. E. Hansen, Annu. Rev. Phys. Chem. **23**, 15 (1972).
[17] M. Born and K. Huang, *Dynamical Theory of Crystal Lattices* (Oxford University Press, 1996).
[18] V. Graves, J. Šenk, P. Kolorenč, N. Sisourat, and J. D. Gorfinkiel, J. Chem. Phys. **160**, 204306 (2024).
[19] I. I. Sobel'Man, *An Introduction to the Theory of Atomic Spectra*, *International Series in Natural Philosophy* (Elsevier Ltd., 1973), Vol. 40.
[20] J. Mahanty and B. W. Ninham, J. Chem. Phys. **59**, 6157 (1973).
[21] J. Franz, R. Bennett, and S. Y. Buhmann, Phys. Rev. A **104**, 013103 (2021).
[22] A. Niggas, S. Creutzburg, J. Schwestka, B. Wöckinger, T. Gupta, P. L. Grande, D. Eder, J. P. Marques, B. C. Bayer, F. Aumayr, R. Bennett, and R. A. Wilhelm, Commun. Phys. **4**, 180 (2021).
[23] P. G. Burke, *R-Matrix Theory of Atomic Collisions* (Springer, Berlin, Heidelberg, 2011).
[24] J. Tennyson, Phys. Rep. **491**, 29 (2010).
[25] D. M. Chase, Phys. Rev. **104**, 838 (1956).
[26] F. H. M. Faisal and A. Temkin, Phys. Rev. Lett. **28**, 203 (1972).
[27] A. Temkin and E. C. Sullivan, Phys. Rev. Lett. **33**, 1057 (1974).
[28] M. Shugard and A. U. Hazi, Phys. Rev. A **12**, 1895 (1975).
[29] D. T. Stibbe and J. Tennyson, New J. Phys. **1**, 2 (1999).
[30] L. H. Scarlett, D. V. Fursa, J. Knol, M. C. Zammit, and I. Bray, Phys. Rev. A **103**, L020801 (2021).
[31] J. Seong, K. C. Janda, M. P. McGrath, and N. Halberstadt, Chem. Phys. Lett. **314**, 501 (1999).
[32] E. M. Jahr and J. Šenk (2025). "Influence of vibrational motion and temperature on Interatomic Coulombic electron capture - Figures," Figshare. https://doi.org/10.6084/m9.figshare.28883378.v2
[33] E. M. Jahr (2025). "ETM-IV v0.1.0: Implementation of the analytical energy and electron transfer model for ICEC with vibrational motion," Zenodo. https://doi.org/10.5281/zenodo.15348382
[34] "The mpmath development team, "Mpmath: A Python library for arbitrary-precision floating-point arithmetic," (2023), version 1.3.0, http://mpmath.org/.
[35] A. Matsumoto, J. Phys. B: At., Mol. Opt. Phys. **21**, 2863 (1988).
[36] G. V. Marr and J. B. West, At. Data Nucl. Data Tables **18**, 497 (1976).
[37] P. Pyykkö and M. Atsumi, Chem. - Eur. J. **15**, 186 (2009).
[38] Z. Mašín, J. Benda, J. D. Gorfinkiel, A. G. Harvey, and J. Tennyson, Comput. Phys. Commun. **249**, 107092 (2020).
[39] H.-J. Werner, P. J. Knowles, G. Knizia, F. R. Manby, and M. Schütz, WIREs Comput. Mol. Sci. **2**, 242 (2012).
[40] H.-J. Werner, P. J. Knowles, F. R. Manby, J. A. Black, K. Doll, A. Heßelmann, D. Kats, A. Köhn, T. Korona, D. A. Kreplin, Q. Ma, T. F. Miller III, A. Mitrushchenkov, K. A. Peterson, I. Polyak, G. Rauhut, and M. Sibaev, J. Chem. Phys. **152**, 144107 (2020).
[41] H.-J. Werner, P. J. Knowles, P. Celani, W. Györffy, A. Hesselmann, D. Kats, G. Knizia, A. Köhn, T. Korona, D. Kreplin, R. Lindh, Q. Ma, F. R. Manby, A. Mitrushenkov, G. Rauhut, M. Schütz, K. R. Shamasundar, T. B. Adler, R. D. Amos, S. J. Bennie, A. Bernhardsson, A. Berning, J. A. Black, P. J. Bygrave, R. Cimiraglia, D. L. Cooper, D. Coughtrie, M. J. O. Deegan, A. J. Dobbyn, K. Doll, M. Dornbach, F. Eckert, S. Erfort, E. Goll, C. Hampel, G. Hetzer, J. G. Hill, M. Hodges, T. Hrenar, G. Jansen, C. Köppl, C. Kollmar, S. J. R. Lee, Y. Liu, A. W. Lloyd, R. A. Mata, A. J. May, B. Mussard, S. J. McNicholas, W. Meyer, T. F. Miller III, M. E. Mura, A. Nicklass, D. P. O'Neill, P. Palmieri, D. Peng, K. A. Peterson, K. Pflüger, R. Pitzer, I. Polyak, M. Reiher, J. O. Richardson, J. B. Robinson, B. Schröder, M. Schwilk, T. Shiozaki, M. Sibaev, H. Stoll, A. J. Stone, R. Tarroni, T. Thorsteinsson, J. Toulouse, M. Wang, M. Welborn, and B. Ziegler, *MOLPRO, 2012.1, a package of ab initio programs*, 2025.

[42]K. Houfek, J. Benda, Z. Mašín, A. Harvey, T. Meltzer, V. Graves, and J. D. Gorfinkiel, Comput. Phys. Commun. **298**, 109113 (2024).
[43]D. T. Colbert and W. H. Miller, J. Chem. Phys. **96**, 1982 (1992).
[44]J. Stoer, R. Bulirsch, R. H. Bartels, W. Gautschi, and C. Witzgall, *Introduction to Numerical Analysis*, in *Texts in Applied Mathematics No. 12*, 2nd ed. (Springer, 1993).
[45]M. Abramowitz and I. A. Stegun, *Handbook of Mathematical Functions with Formulas, Graphs, and Mathematical Tables*, 10th ed. (Dover, New York, 1964).
[46]R. L. Burden, J. D. Faires, and A. M. Burden, *Numerical Analysis*, 10th ed. (Cengage Learning, 2016).
[47]J. Šenk (2025). "Code for ICEC cross sections with vibrational motion using fixed-nuclei R-matrix results," Zenodo. https://doi.org/10.5281/zenodo.15302392
[48]E. M. Jahr (2025). "Influence of vibrational motion and temperature on Interatomic Coulombic electron capture - Dataset," Figshare. https://doi.org/10.6084/m9.figshare.28892498.v2
[49]J. Šenk (2025). "R-matrix approach data supporting 'influence of vibrational motion and temperature on Interatomic Coulombic electron capture,'" Figshare. https://doi.org/10.6084/m9.figshare.28883423
[50]E. A. Gislason, J. Chem. Phys. **58**, 3702 (1973).

Time-resolved spectroscopy of interparticle Coulombic decay processes

Elke Fasshauer* and Lars Bojer Madsen
Department of Physics and Astronomy, Aarhus University and Ny Munkegade 120, 8000 Aarhus, Denmark

(Received 12 April 2019; revised manuscript received 6 March 2020; accepted 17 March 2020; published 24 April 2020)

We report the theory for time-resolved spectator resonant interparticle Coulombic decay (ICD) processes. Following excitation by a short extreme ultraviolet pulse, the spectrum of the resonant ICD electron develops. Strong-field ionization is imagined to quench the decay at different time delays and to initiate regular ICD. In this latter process, the ICD electron signal can be measured without interference effects. The typical lifetimes of ICD processes allow for the observation of oscillations of the time- and energy-differential ionization probability. We propose to utilize this oscillation to measure lifetimes of electronic decay processes.

DOI: 10.1103/PhysRevA.101.043414

I. INTRODUCTION

Interparticle Coulombic decay (ICD) [1,2] is an electronic decay process of ionized systems consisting of at least two weakly bonded units, be it atoms, molecules, or clusters. ICD has been observed in multiple systems like noble gas clusters [3–11] and clusters of different solvent molecules like water [4,5,12] or ammonia [13–16]. It allowed one to explain the repair mechanism of the enzyme photolyase [17] and was used to establish a more efficient double ionization strategy [18]. ICD is furthermore discussed as a source of slow electrons, which are most efficient in damaging the DNA after exposure to high energy radiation or radioactive materials in the human body [19–24]. In this work, we shed light on this fundamental process by offering a time-resolved perspective directly of the electron dynamics.

Due to developments in creating short pulses in the extreme ultraviolet (XUV) and x-ray domain [26] a time-dependent investigation of ICD processes should be within reach. Fano profiles of a much faster autoionization (AI) process were recently measured [27,28]. A few time-resolved investigations of ICD have already been performed theoretically and experimentally, where the ions produced in the process were measured [29–36]. However, electrons can be measured with higher energy resolution than ions and grant direct access to the electron dynamics and interference effects during the process. In this work, we will therefore focus on the evolution of the time- and energy-differential ionization probability, propose how it might be possible to measure this quantity in experiment, and discuss how decay lifetimes can be determined from the time-resolved signal.

In brief, the ICD process starts from a unit A, which is ionized in the inner valence shell. This vacancy is filled by an electron from the same unit and the excess energy is simultaneously transferred to a neighboring unit B. The latter is consequently ionized by emission of the ICD electron. The two positively charged units undergo a Coulomb explosion (see Fig. 1). A related process is initiated by an excitation of unit A. This resonant ICD (RICD) can be characterized by the behavior of the excited electron: it either participates in the decay process or not. The respective processes are called participator RICD (pRICD) [37] and spectator RICD (sRICD) [37–42]. In this work, we will focus on the sRICD signal: Unit A is excited from the inner valence. The vacancy is then filled by an electron from the valence and the excess energy is used to ionize the neighboring unit B (see Fig. 1). This process is usually characterized by lifetimes of several tens to hundreds of femtoseconds. After the sRICD process, the excited unit A decays via fluorescense within a few nanoseconds. AI and pRICD are competing decay channels and their effect on the sRICD signal is taken into account in the theory developed below.

We propose to initiate an sRICD process by exciting with a short XUV pulse. The system will then decay under emission of an sRICD electron. This is illustrated in Fig. 1 for electronic energies and resonance parameters corresponding to the neon dimer after an excitation to the Ne $2s^{-1}5p$ state. At a later time t_s, a second short and intense infrared (IR) laser pulse quenches the sRICD process by ionization. By varying the time delay t_s one should be able to observe the time-dependent formation of the sRICD signal, as illustrated to the right in Fig. 1 before the second laser pulse, by pump-probe spectroscopy similar to the AI process measured in Ref. [27]. At the same time, the proposed quenching would initiate an ICD process involving the excited ion A^{+*}. Due to the strong-field ionization initiating this latter process, the signals are well separated in energy. In this paper we provide the basic formulation for a purely electronic solution upon which more complex scenarios, including nuclear dynamics, will be built in future work.

II. THEORY

The relevant property for the description of the time evolution of the ICD processes is the time- and energy-differential ionization probability obtained from the time-dependent wave function $|\Psi(t)\rangle$ by $P(E_{\rm kin},t)=\sum_i |\langle E_i|\Psi(t)\rangle|^2$. Here $|E_i\rangle$

*elke.fasshauer@gmail.com

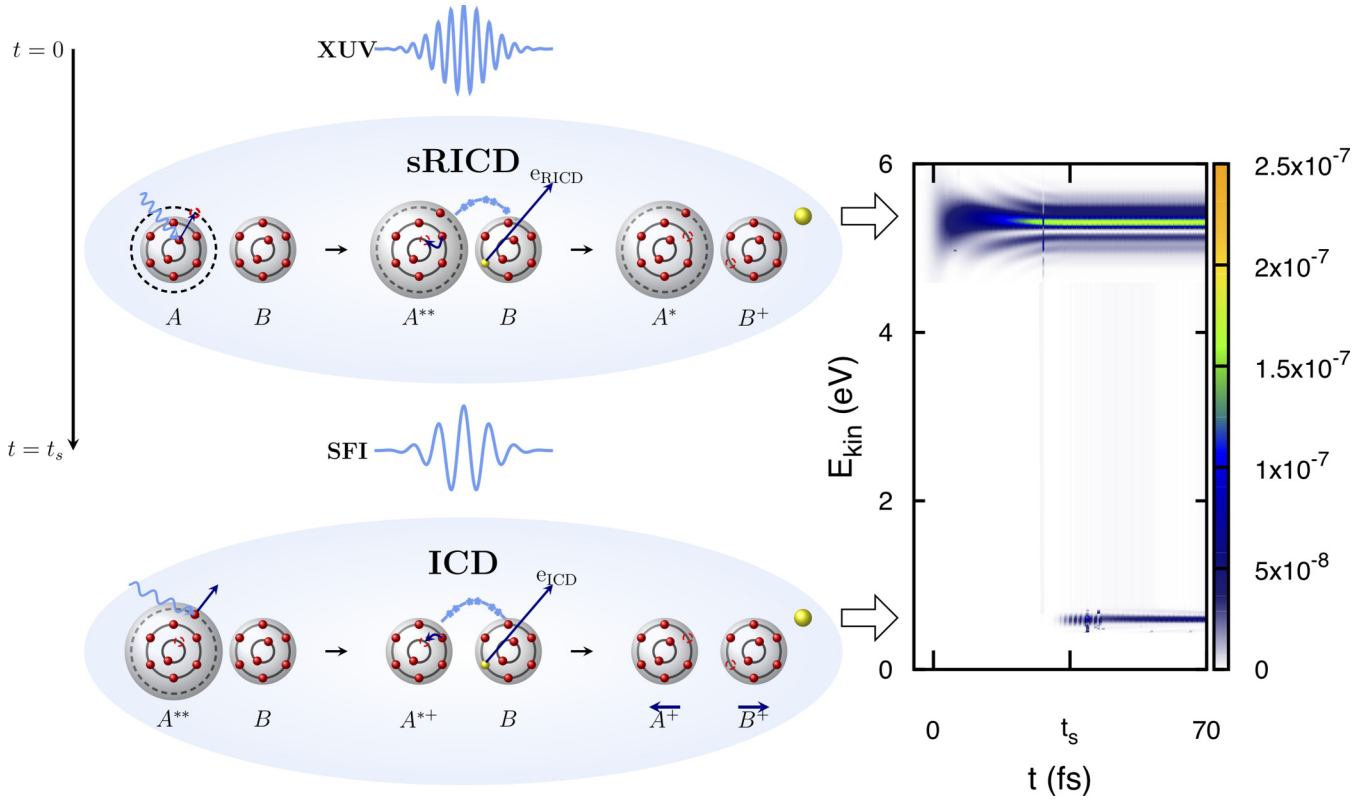

FIG. 1. Illustration [25] of the considered process. At $t = 0$, a spectator resonant interparticle Coulombic decay (sRICD) is initiated by XUV excitation. At a later time t_s, which in this example plot is 35 fs, a second strong infrared laser pulse quenches the sRICD process by ionization and thereby initiates ICD. The signals of the respective electrons with kinetic energies E_{kin} are well separated. While the sRICD appears from the start of the XUV pulse centered at $t = 0$, the ICD signal appears after the second pulse. This approach allows for a time-resolved measurement of the sRICD signal and an interference free measurement of the ICD signal. sRICD: unit A is excited from the inner valence shell. The created vacancy is filled with an electron from the outer valence and the excess energy is simultaneously transferred to B, which emits the sRICD electron. ICD: The initial state is created by removing the excited electron in A. It is then filled by an electron of the outer valence of A while the excess energy is transferred to B, which consequently emits the ICD electron. The two units are both positively charged and therefore undergo Coulomb explosion. The panel to the right illustrates typical time and energy resolved traces of sRICD and ICD electrons (see text).

denotes a continuum state with energy E_i, which entails both the kinetic energy E_{kin} of the emitted electron and the energy of the final cationic state i. These continuum states are orthogonal to all bound states of the system and amongst each other. Because the signals of the competing decay channels do not overlap, we can and will focus on the sRICD signal. Atomic units are used throughout unless stated otherwise.

We obtain the wave function of the system by solving the time-dependent Schrödinger equation $i\partial_t |\Psi(t)\rangle = H(t)|\Psi(t)\rangle$ for a model system consisting of the ground state $|G\rangle$, the resonant state $|R\rangle$ for the sRICD, and the resonant state $|I\rangle$ for the ICD process, as well as three sets of continuum states characterized by the respective final state energy of the decay process. All parameters describing a general resonant state are designated by the index r. The Hamiltonian consists of the single configuration Hamiltonian H_0, the residual configuration interaction operators V_{RICD} and V_{ICD} as well as V_o for the competing autoionization and pRICD decay channels, and the operator $H_X(t)$ of the exciting XUV pulse:

$$H(t) = H_0 + V_{\text{sRICD}} + V_o + V_{\text{ICD}} + H_X(t). \quad (1)$$

The effect of the ionizing infrared pulse is modeled by terminating the sRICD and starting the ICD process at the time of the second pulse t_s. We will come back to this point below.

A. Description of the RICD process

The sRICD process we intend to describe in a fully time-dependent manner is schematically illustrated in Fig. 2. Starting from the ground state $|G\rangle$ we excite the system with an XUV pulse with a mean photon energy Ω into the resonant state $|R\rangle$ with the corresponding energy E_R. This resonant state can then under emission of an electron either decay to the continuum state characterized by a final state of the sRICD $|E_{sR}\rangle$ with a partial lifetime of τ_{sR} or to a continuum state characterized by the shared final state of pRICD and autoionization (AI) decay $|E_o\rangle$ with a different partial lifetime τ_o. The continuum state of the sRICD couples to other continuum states under emission of a photon. This fluorescence process is usually several orders of magnitude slower than the electronic decay process and is therefore ignored in this work. Alternatively to arriving in the continuum via the decaying resonant state, a simultaneous direct excitation and ionization

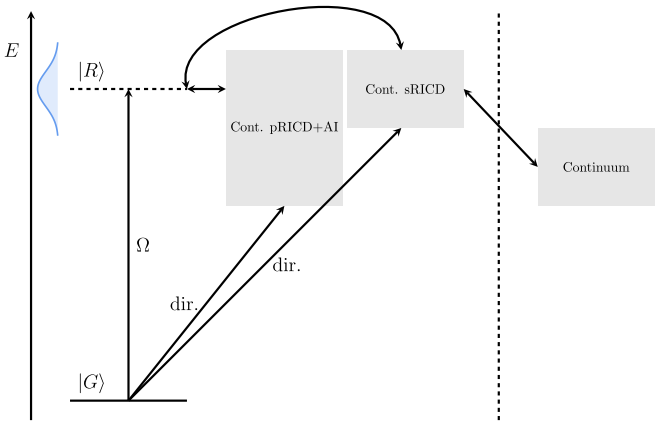

FIG. 2. Schematic illustration of the energy levels involved in the RICD process. The laser pulse with mean photon energy Ω excites the system into the resonant state $|R\rangle$ with energy E_R. The resonant state couples to two continua (denoted Cont. in the figure), one characterized by the sRICD final state and the other characterized by the pRICD and AI final state. Both channels have partial lifetimes in the order of femtoseconds. The continuum state of the sRICD process can then couple to other continuum states by emission of a photon. This fluorescence process has a lifetime $\tau_{\text{fl.}}$, which typically is in the order of nanoseconds and therefore much larger than the timescales of interest here. Alternatively, all continuum states can be reached directly by simultaneously ionizing and exciting in the case of the sRICD or single ionization in the case of the pRICD and AI. All couplings to the continuum via spontaneous radiative transitions are ignored in this work.

in the case of sRICD or a direct ionization in the case of the pRICD and AI channel, is also possible, which is denoted "dir" in the figure.

We assume low field strengths of the XUV pulse and therefore use first-order perturbation theory to describe its interaction with the system. Hence the wave function evolves according to

$$|\Psi(t)\rangle = \tilde{U}(t,t_0)\,|G(t_0)\rangle - i\int_{t_0}^{t} dt'\,\tilde{U}(t,t')H_X(t')\,|G(t')\rangle\,. \tag{2}$$

Here, $\tilde{U}(t,t_0)$ is the time evolution operator from a time t_0 until time t of the unperturbed system pertaining to the first four terms on the right-hand side of Eq. (1).

We are free to choose an energy reference and therefore set $E_G = 0$. This conveniently removes the time dependence from the ground state, since $|G(t_0)\rangle = \exp\{-iE_G t_0\}\,|G\rangle = |G\rangle$.

We introduce approximations for the time-evolution operator $\tilde{U}(t,t')$ appearing in the last term of Eq. (2). After the system has interacted with the XUV via $H_X(t')$ at time t', the system decays via the configuration interaction V. In this general discussion, V refers to the sum of all configuration-interaction terms of Eq. (1). We will specify the explicit form of V for the different cases below. In the continuum we neglect the Coulomb interaction for simplicity, which leads to the time-evolution operator

$$\tilde{U}(t,t') = U_0(t,t') - i\int_{t'}^{t} dt''\,U_0(t,t'')\,V\,\tilde{U}(t'',t'), \tag{3}$$

where $U_0(t,t')$ is the free-particle time-evolution operator.

By inserting Eq. (3) into Eq. (2) we arrive at

$$\begin{aligned}|\Psi(t)\rangle = \tilde{U}(t,t_0)\,|G\rangle &- i\int_{t_0}^{t} dt'\,U_0(t,t')H_X(t')\,|G\rangle \\ &- \int_{t_0}^{t} dt'\int_{t'}^{t} dt''\,U_0(t,t'')\,V\,\tilde{U}(t'',t')\,H_X(t')\,|G\rangle\,.\end{aligned} \tag{4}$$

The time-evolution operator $\tilde{U}(t'',t')$ in the last integral describes the contribution of the Hamiltonian $H_0 + V$. This is equivalent to the Hamilton operator used in Fano's description [43] of a decaying resonant state and below we therefore add the subscript F to the time-evolution operator and remove the tilde.

We now project on a continuum state $|E_{sR}\rangle$ characterized by the sRICD final state energy of the ionized system and the kinetic energy of the emitted electron. The first term vanishes, because of the orthogonality between bound and continuum states, and we obtain

$$\begin{aligned}\langle E_{sR}|\Psi(t)\rangle = &- i\int_{t_0}^{t} dt'\,\langle E_{sR}|U_0(t,t')H_X(t')|G\rangle \\ &- \int_{t_0}^{t} dt'\int_{t'}^{t} dt''\,\langle E_{sR}|\,U_0(t,t'')\,V \\ &\times U_F(t'',t')\,H_X(t')\,|G\rangle\,.\end{aligned} \tag{5}$$

The time-evolution operator $U_0(t,t')$ solves the time-dependent Schrödinger equation for the Hamiltonian $\vec{p}^{\,2}/2$. The corresponding wave functions with wave vector $\vec{k}$ are $|\Psi^0_{\vec{k}}(t)\rangle = |\vec{k}\rangle\exp[-i\int_{-\infty}^{t} dt'\frac{1}{2}\vec{k}^2]$. Another way of formulating a time-evolution operator is by a projection from basis functions at time t' to such of time t:

$$U_0(t,t') = \int d\vec{k}\,\left|\Psi^0_{\vec{k}}(t)\right\rangle\left\langle\Psi^0_{\vec{k}}(t')\right|\,. \tag{6}$$

At this point we only consider the kinetic energy of the emitted electron and can therefore write the projection of a general continuum state $\langle E|$ on the free-particle time-evolution operator in the following way:

$$\langle E|\,U_0(t,t') = \langle E|\,\exp[i\Phi_0(E,t,t')] \tag{7}$$

$$= \langle E|\,\exp\left[-i\int_{t'}^{t}\left(\frac{k^2}{2} + E_{\text{fin}}\right)dt'''\right], \tag{8}$$

where $k^2/2$ is the kinetic energy relative to the final state E_{fin}. The interaction V between a general resonant state $|r\rangle$ coupling to one of the continuum states is given by

$$V = \int dE'\;|E'\rangle\,V_{E'r}\,\langle r| + \int dE'\;|r\rangle\,V_{rE'}\,\langle E'|\,. \tag{9}$$

For two different final states, and therefore two continua, it reads

$$\begin{aligned}V = &\int dE_1'\;|E_1'\rangle\,V_{E_1'r}\,\langle r| + \int dE_1'\;|r\rangle\,V_{rE_1'}\,\langle E_1'| \\ &+ \int dE_2'\;|E_2'\rangle\,V_{E_2'r}\,\langle r| + \int dE_2'\;|r\rangle\,V_{rE_2'}\,\langle E_2'|\,.\end{aligned} \tag{10}$$

This case is, e.g., relevant for systems that cannot only decay via sRICD but also via autoionization or pRICD, which both yield a singly ionized system, which is the case that we investigate. At the same time, the initiating energy of the XUV laser pulse will be chosen too low to initiate an ICD process. Hence $V = V_{\mathrm{sRICD}} + V_o$ in our case.

We also insert the resolution of the identity between the Fano time-evolution $U_F(t'', t')$ operator, to be specified below, and the Hamilton operator of the XUV field using

$$\mathbb{1} = |R\rangle\langle R| + \int dE_1' \, |E_1'\rangle\langle E_1'| + \int dE_2' \, |E_2'\rangle\langle E_2'| \tag{11}$$

$$= |R\rangle\langle R| + \int dE_{sR}' \, |E_{sR}'\rangle\langle E_{sR}'| + \int dE_o' \, |E_o'\rangle\langle E_o'| \, . \tag{12}$$

By suppressing all dependences on angular momentum and using Eqs. (5), (10), and (12) we arrive at an amplitude of the sRICD process for the resonance $|R\rangle$ consisting of four terms:

$$\begin{aligned}\langle E_{sR}|\Psi(t)\rangle = &-i\int_{t_0}^{t} dt' \, \langle E_{sR}|U_0(t,t')H_X(t')|G\rangle - \int_{t_0}^{t} dt' \int_{t'}^{t} dt'' \, \langle E_{sR}|U_0(t,t'')|E_{sR}\rangle \, V_{ER} \, \langle R|U_F^R(t'',t')|R\rangle \, \langle R|H_X(t')|G\rangle \\ &- \int_{t_0}^{t} dt' \int_{t'}^{t} dt'' \int dE_{sR}' \, \langle E_{sR}|U_0(t,t'')|E_{sR}\rangle \, V_{ER} \, \langle R|U_F^R(t'',t')|E_{sR}'\rangle \, \langle E_{sR}'|H_X(t')|G\rangle \\ &- \int_{t_0}^{t} dt' \int_{t'}^{t} dt'' \int dE_o' \, \langle E_{sR}|U_0(t,t'')|E_{sR}\rangle \, V_{ER} \, \langle R|U_F^R(t'',t')|E_o'\rangle \, \langle E_o'|H_X(t')|G\rangle \, . \end{aligned} \tag{13}$$

In these expressions, $U_0(t,t')$ is the free particle time-evolution operator, whose action was specified in Eq. (8). $V_{ER} = \langle E|V|R\rangle = \sqrt{\Gamma_{sR}/(2\pi)}$ is related to the partial sRICD decay rate of the resonant state Γ_{sR} and $U_F^R(t'',t')$ is the Fano time-evolution operator, which is specific to the resonant state $|R\rangle$. The variables of the other, competing, processes are designated with the index o. The total decay width of the RICD resonant state is given by $\Gamma_R = \Gamma_{sR} + \Gamma_o$.

The terms of Eq. (13) are linked to the different pathways shown in Fig. 2 as follows. The first term of Eq. (13) describes the direct excitation and ionization to the continuum state, while the second term describes the excitation from the ground state to the resonant state followed by a decay to the continuum state. The third, indirect, term describes the direct excitation and ionization to the continuum state related to the sRICD final state, which couples to the resonant state, which then again decays into the continuum state. The last term is similar to the indirect term, but couples to the continuum of the competing pRICD and AI channels. Due to a different model system including only one final state, the latter term is not present in Eq. (11) of Ref. [44]. The interference of these different terms leads to the characteristic Fano profile [43].

We describe the interaction between the system and the exciting XUV field in the dipole approximation. Therefore, the corresponding Hamilton operator in the length gauge is given by $H_X(t') = -\mu E_X(t') = -\mu \frac{d}{dt'} A_X(t') f_X(t')$, where $E_X(t')$ denotes the time-dependent field strength of the XUV laser, while μ denotes the dipole operator, $A_X(t') = A_{0X}\cos(\Omega t')$ is the vector potential of the laser field in the direction of the linear polarization, and $f_X(t')$ is the Gaussian pulse envelope. Over the energy range of interest, we assume the transition dipole matrix element from the ground state to the continuum to be independent of the energy of the continuum state. To indicate these assumptions, we change the notation as $\langle E_i|\mu|G\rangle = \langle C_i|\mu|G\rangle$. We furthermore assume the coupling elements between the resonant and the continuum state to be real and independent of the continuum energy and therefore change the notation $V_{E_1R} \to V_R$ and $V_{E_2R} \to W_R$. Then, the Fano matrix elements, i.e., $\langle R|U_F^R(t'',t')|R\rangle$ and $\langle R|U_F^R(t'',t')|E'\rangle$ of Eq. (13), can be solved using the projection formulation of the Fano time-evolution operator and solving the resulting integral by contour integration. Hence we write the Fano time-evolution operator as

$$\begin{aligned} U_F(t'',t') &= \int d\underline{E} \, |\Psi_{\underline{E}}(t'')\rangle\langle\Psi_{\underline{E}}(t')| \\ &= \int d\underline{E} \, |\Psi_{\underline{E}}\rangle\langle\Psi_{\underline{E}}| \, \exp[-i\underline{E}(t''-t')]. \end{aligned} \tag{14}$$

The evaluation of these Fano matrix elements is given in the Appendix and for the sRICD signal we finally arrive at

$$\begin{aligned}\langle E|\Psi(t)\rangle = &\, i\langle C_{sR}|\mu|G\rangle \int_{t_0}^{t} dt' \, \exp[i\Phi_0(E_{sR},t,t')]E_X(t') \\ &+ \big(V_R\langle R|\mu|G\rangle - i\pi V_R^2\langle C_{sR}|\mu|G\rangle \\ &\quad - i\pi V_R W_R\langle C_o|\mu|G\rangle\big) \\ &\times \int_{t_0}^{t} dt' \int_{t'}^{t} dt'' \, \exp[i\Phi_0(E_{sR},t,t'')] \\ &\times \exp\left\{-i\left[E_R - i\pi\left(V_R^2 + W_R^2\right)\right](t''-t')\right\}E_X(t'). \end{aligned} \tag{15}$$

The first integral corresponds to the direct ionization process. The second integral is identical for the resonant and the two indirect terms. They have, though, different prefactors. For the case of a slowly varying envelope function $[\frac{d}{dt'} f_X(t') \approx 0]$ and only considering the absorption of an XUV photon these two integrals are solved analytically for times after the exciting pulse. The direct term is given by

$$\begin{aligned} &-\frac{A_{0X}\Omega\langle C_{sR}|\mu|G\rangle}{4} \exp[-it(E_{\mathrm{kin}} + E_{\mathrm{fin}})] \\ &\times \exp\left[-\frac{\sigma^2}{2}(E_{\mathrm{kin}} + E_{\mathrm{fin}} - \Omega)^2\right] \\ &\times \mathrm{Re}\left\{\mathrm{erf}\left[\frac{1}{\sqrt{2}\sigma}\left(\frac{T_X}{2} + i\sigma^2(E_{\mathrm{kin}} + E_{\mathrm{fin}} - \Omega)\right)\right]\right\}, \end{aligned} \tag{16}$$

where Re denotes the real value and erf denotes the error function. The resonant and indirect ionization terms without their respective prefactors are given by

$$+\frac{A_{0X}\,\Omega}{4\left[E_R - i\pi\left(V_R^2+W_R^2\right) - E_{\rm kin} - E_{\rm fin}\right]}\exp\left[-it\left[E_R - i\pi\left(V_r^2+W_R^2\right)\right]\right]\exp\left[-\frac{\sigma^2}{2}(E_R-\Omega)^2\right](\mathrm{erf}(\tau_{1,\max})-\mathrm{erf}(\tau_{1,\min}))$$
$$-\frac{A_{0X}\,\Omega}{4\left[E_R - i\pi\left(V_R^2+W_R^2\right) - E_{\rm kin} - E_{\rm fin}\right]}\exp[-it(E_{\rm kin}+E_{\rm fin})]\exp\left[-\frac{\sigma^2}{2}(E_{\rm kin}+E_{\rm fin}-\Omega)^2\right](\mathrm{erf}(\tau_{2,\max})-\mathrm{erf}(\tau_{2,\min})), \quad (17)$$

with $\tau_{1,\max}=\frac{1}{\sqrt{2}\sigma}(\frac{T_X}{2}-i\sigma^2[E_R-i\pi(V_R^2+W_R^2)-\Omega])$, $\tau_{1,\min}=-\frac{1}{\sqrt{2}\sigma}(\frac{T_X}{2}+i\sigma^2[E_R-i\pi(V_R^2+W_R^2)-\Omega])$, $\tau_{2,\max}=\frac{1}{\sqrt{2}\sigma}(\frac{T_X}{2}-i\sigma^2(E_{\rm kin}+E_{\rm fin}-\Omega))$, and $\tau_{2,\min}=-\frac{1}{\sqrt{2}\sigma}(\frac{T_X}{2}+i\sigma^2(E_{\rm kin}+E_{\rm fin}-\Omega))$. Here, σ is the standard deviation of the Gauss distribution in time and T_X is the duration of the exciting XUV pulse.

The time- and energy-differential ionization probability of the RICD process is the absolute square of the amplitude given in Eq. (15) and therefore a sum over 28 different terms (seven absolute squares and 21 mixed interference terms). Their relative contributions are determined by the Fano parameter $q=\frac{\langle R|\mu|G\rangle}{\langle C|\mu|G\rangle\pi V_R}$.

B. Transition from the resonant state of the RICD process to the initial state of the ICD process

We propose a time-resolved measurement of the RICD process, where the quenching of the RICD process by strong field ionization with an IR pulse at time t_s entails the initiation of an ICD process. Technically, this means a population transfer from the resonant state of the RICD process to the initial state of the ICD process. We assume the transition in time to be Gaussian shaped and that the ICD signal is unaffected by pulse shape effects. The transition is modeled as follows.

We determine the remaining population of the resonant state of the RICD process N_0 at the beginning of the second pulse $t=t_s-\delta t$ as

$$N_0 = \frac{|\langle R|\mu|G\rangle|^2}{4}\exp[-\sigma^2(\Omega-E_R)^2] \times \exp[-(\Gamma_{sR}+\Gamma_o)(t_s-\delta t)]. \quad (18)$$

Here, δt is chosen as $\frac{5}{2}\sigma_{\rm IR}$ with $\sigma_{\rm IR}$ being the standard deviation of the IR pulse in time. We assume the decrease of the population $N_R(t)$ in the resonant state of the RICD process $|R\rangle$ to have a Gaussian shape $f_{\rm IR}(t)$ centered around the time of the second pulse:

$$\frac{dN_R(t)}{dt} = -f_{\rm IR}(t)N_R(t) \quad (19)$$

and therefore

$$N_R(t) = N_0\exp\left[-\frac{\alpha}{2}\,\mathrm{erf}\left(-\frac{\delta t}{\sqrt{2}\sigma},\frac{t-t_s}{\sqrt{2}\sigma}\right)\right]. \quad (20)$$

Correspondingly, the population of the initial state $|I\rangle$ of the ICD process $N_R(t)$ is increased:

$$N_I(t) = N_0 - N_R(t). \quad (21)$$

The square roots of the time-dependent populations are then updated in every time step and used instead of $\langle r|\mu|G\rangle$ in the calculation of the amplitude of the ionization probability. In order to allow for a complete depopulation of the resonant state, we have chosen $\alpha=8$.

Since we assume a direct population of the resonant state of the ICD process $|I\rangle$ from the resonant state of the sRICD process $|R\rangle$ induced with a short and intense laser pulse, we assume that the terms of Eq. (13), which are mediated by the continuum, can be neglected. After the end of the ionizing pulse the amplitude of the ICD process associated with resonance $|I\rangle$ therefore reads

$$\langle E|\Psi(t)\rangle = -\int_{t_0}^{t} dt_s \int_{t_s+\delta t}^{t} dt''\ \langle E|U_0(t,t'')|E\rangle \times V_{EI}\ \langle I|U_F^I(t'',t_s)|I\rangle\sqrt{N_I}. \quad (22)$$

III. COMPUTATIONAL DETAILS

In our model system, where the nuclei are kept fixed, we evaluated Eq. (13), and simulated the time-dependent buildup of the Fano resonance for the sRICD process for parameters corresponding to those of the neon dimer at the equilibrium distance of 3.08 Å [47] after an excitation to the Ne$2s^{-1}2p^6 5p_z$ state. The parameters are given in Table I. All simulations were performed with ELDEST [48–52], where only the outer integral over t' in Eq. (15) is solved numerically. We use the Fano parameter $q=10$. The exact q value is unknown to us, but we expect it to be larger than unity due to the low probability for direct single photon ionization and excitation. Since the exact q values are unknown, we assume equal values for the two continua. We have performed calculations for a range of q parameters, of which a cut is shown in Fig. 3. The time of $t=93$ fs after the initiating excitation

TABLE I. Energies and lifetimes for the excited states Ne$2s^{-1}2p^6 np$-Ne ($n=4,5$) undergoing RICD. The resonant energies are taken from Ref. [45], the final-state energies of the sRICD Ne$2s^2 2p^5(P_{3/2,1/2})np$-Ne$2p^5(P_{3/2,1/2})$, of the pRICD and AI Ne$2s^2 2p^5(P_{3/2,1/2})$-Ne and the ICD process were averaged to give approximations of nonrelativistic energies. The lifetimes, τ, of the sRICD and pRICD+AI are from Ref. [40] and the ICD lifetime are from Ref. [46].

	$n=4$	$n=5$	pRICD + AI	ICD
E_r [eV]	47.1230		47.6930	48.4750
$E_{\rm fin}$ [eV]	41.8391	42.4138	21.6290	47.8688
$\tau[2s^{-1}(np_z)^1\Sigma_u^+]$ [fs]	112	106	206	98

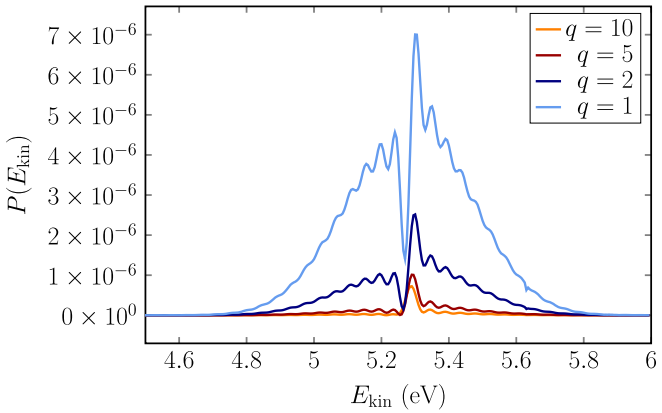

FIG. 3. Peak shape of the spectator RICD electron spectrum for 50 cycles of the exciting pulse with different values of the Fano q parameter at time $t = 93$ fs after the excitation at time $t = 0$. The Fano profile is modified by an oscillation in energy. This oscillation stems from the interference terms of the direct term with the resonance terms of $P(E_{\rm kin}, t)$ and is described by Eq. (24). The larger q, the less likely the direct path and therefore, for increasing q, the signal is damped for a given transition dipole moment into the resonant state.

was chosen to illustrate a typical behavior. It becomes evident that the basic features of the spectra are identical, even though the width and the amplitude of the signal differ. Therefore, the conclusions of this paper are independent of the choice of the q parameter.

The exciting pulse for the main results in Figs. 1 and 5 has $A_{0X} = 5 \times 10^8\,\mathrm{W/cm^2}$, $\Omega = 47.6930\,\mathrm{eV}$, and a FWHM $= 6.1$ fs corresponding to 50 cycles. This duration ensures that the bandwidth is so small that only the Ne$2s^{-1}2p^6 5p_z$ state in the neon dimer is resonantly excited.

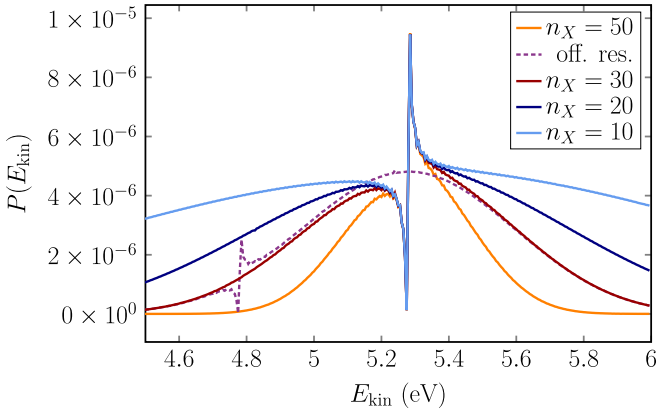

FIG. 4. Peak shape of the sRICD electron spectrum for late time $t \gg \frac{1}{\Gamma_R}$ after excitation of our system with electronic parameters corresponding to those of the $5p$ state in the neon dimer depending on the number of cycles of the exciting pulse n_X. The shape can be explained by folding the Fourier transform of the exciting pulse in time with a Fano profile. In this example, the Fano parameter is $q = 10$. Around the resonance energy, the peaks are identical. The width of the peak is decreased for an increased number of cycles n_X and therefore determined by the duration of the exciting pulse. The dashed line illustrates an excitation 0.5 eV off resonance for $n_X = 30$.

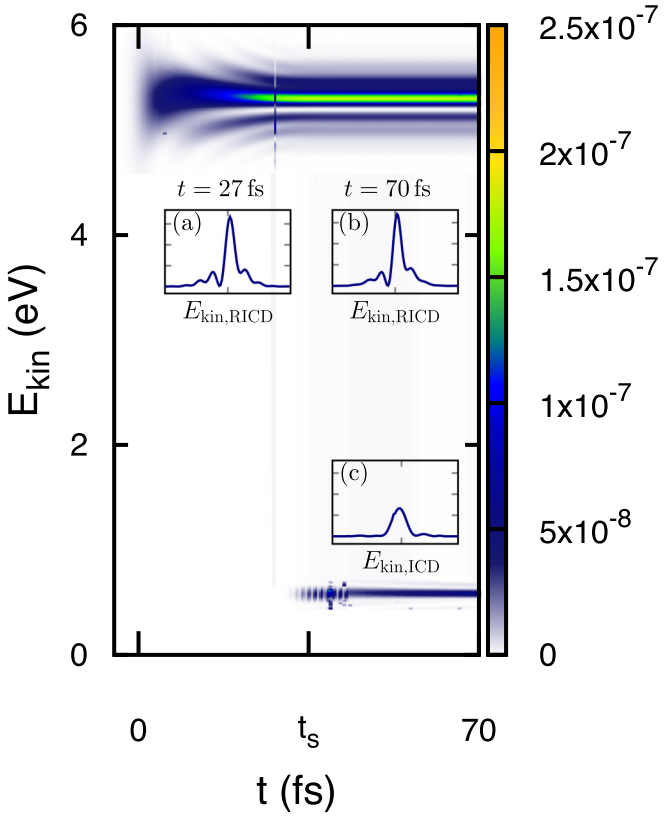

FIG. 5. Time-resolved sRICD and ICD spectrum after initial excitation at $t = 0$ and quenching the sRICD at $t = 35$ fs. The sRICD signal centered around 5.3 eV before the second pulse shows the buildup of a Fano profile, with an additional oscillation in energy $\cos[(E_{\rm kin} + E_{\rm fin} - E_r)t]$ [see (a) and text]. After depopulation of the sRICD resonant state around t_s, the signal shape remains constant [see (b)]. For the ICD signal centered around 0.6 eV shown in (c), only the resonant term of Eq. (13) contributes, which has the shape of a Voigt profile. A pump-probe spectrum can be obtained by varying t_s.

We assumed a complete population transfer from the resonant state of the sRICD process to the resonant state of the ICD process during the second ionizing pulse over a time of 15 fs as realized experimentally [27].

IV. RESULTS AND DISCUSSION

In the investigation of decay processes with short laser pulses, the shortness comes with the cost of an energy broadening. As a consequence, the kinetic-energy spectrum of an sRICD electron is given by a Fano profile centered around the kinetic energy, that corresponds to the energy of the resonant state, convoluted with a Gaussian centered around the kinetic energy, that would correspond to a direct excitation and ionization into the final state. Here, we show the Voigt profile part inherent to most terms of the absolute square of Eq. (15):

$$P(E_{\rm kin}, \infty) \propto \frac{\exp\left[-\sigma_t^2 (E_{\rm kin} + E_{\rm fin} - \Omega)^2\right]}{(E_{\rm kin} + E_{\rm fin} - E_R)^2 + \frac{\Gamma_R^2}{4}}. \qquad (23)$$

The shapes of the spectra are illustrated for different numbers of cycles n_X for the exciting pulse in Fig. 4 for a late time $t \gg \frac{1}{\Gamma_R}$. There, the mean pulse energy was chosen to be on resonance and, therefore, the Fano profile is centered on the maximum of the Gaussian. It is clearly seen how the peak is narrowed with an increased number of laser cycles in the exciting pulse. In order to only excite into a single state we choose $n_X = 50$, such that other excited states are outside $3\sigma_E$ of the energy distribution of the exciting pulse. In future investigations of the interaction between several decaying resonant states, a smaller number of cycles will be appropriate.

For the case of an off-resonant excitation, the Fano profile and the Gaussian will not be centered around the same kinetic energy of the sRICD electron and the sRICD electron peak will be damped accordingly as illustrated by the dashed line of Fig. 4 for $n_X = 30$.

By using the parameters for the neon dimer (see Table I), we simulated the time evolution of an initial excitation at $t = 0$ and quenching of the decay processes by ionization with a second laser pulse centered at the time $t = 35$ fs. The results are presented in Fig. 5. We will discuss its different characteristics separately.

The time-resolved spectrum shows two energy-separated signals within the chosen kinetic-energy range. The signal of the sRICD process is initiated with the first and the signal of the ICD process by the second laser pulse, which at the same time reduces those contributions of the sRICD signal that involve a population of the resonant state. Due to the fast depopulation of the resonant state, the signal before and after the second pulse are effectively the same [compare Figs. 5(a) and 5(b)]. This allows one to generate a full pump-probe spectrum. The competing autoionization and pRICD process would result in much higher kinetic electron energies of about 26 eV and can therefore unambigously be distinguished from the sRICD and ICD electrons shown in Fig. 5.

While the sRICD signal shows the buildup of a Fano profile [see Fig. 5(a)], and therefore interference effects, the ICD signal is an interference free Voigt profile [see Fig. 5(c)], because only the resonant term [see Eq. (22)] significantly contributes to it. This can be explained by the initiating process being ionization rather than excitation. In case of the ICD process, the final state is characterized by a doubly ionized system. A single photon double ionization with low laser intensities is very unlikely compared to a single ionization. Hence the corresponding Fano parameter would be very large and interference effects would have low amplitudes. At the same time, the kinetic-energy distribution of the two emitted electrons can be expected to be wide and not necessarily to peak at the energy of the ICD electrons, which would further marginalize the contribution of the direct pathway. As a result, the signal shape is described by the absolute square of Eq. (22), i.e., the terms of Eq. (17).

We now turn our attention from the variation of the signals in energy to their variation in time. During the buildup of the signals over time, they show oscillations in both energy and time, which are easiest seen for the ICD in the video of the Supplemental Material [53]. For the sRICD process, the variation in time can be obtained by solving the dominant part of the absolute square of Eq. (15) analytically. For the ICD process, the dominant part of the absolute square of Eq. (22) needs to be solved. In both cases, it can be shown that the signal is proportional to

$$\cos[(E_r - E_{\text{kin}} - E_{\text{fin}})t]\, \exp\left(-\frac{\Gamma_r}{2}t\right). \tag{24}$$

This equation is not specific to the decay process and therefore valid for both the sRICD and the ICD signal ($r = R, I$). The variation in energy, illustrated in Fig. 5(a), is in agreement with Ref. [54]. As can be seen from Eq. (24), the oscillation is also visible in time as shown in Fig. 6 for a fixed kinetic energy of the sRICD electron of $E_{\text{kin}} = 5.3$ eV.

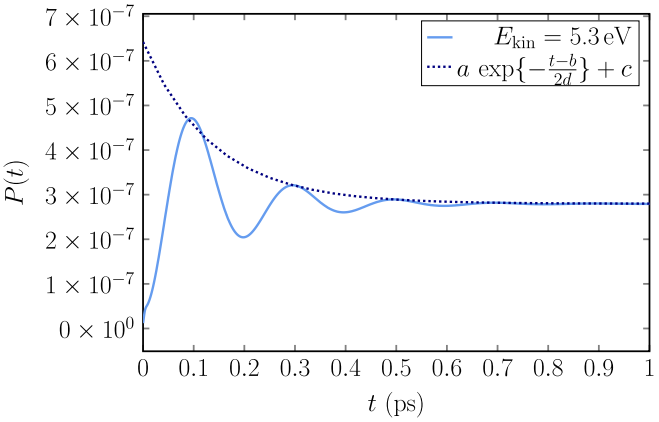

FIG. 6. Oscillation in time for observing the sRICD electron with a kinetic energy of 5.3 eV, for $n_X = 50$ and $q = 10$. This oscillation can be described by $\cos[(E_{\text{kin}} + E_{\text{fin}} - E_r)t]$. Its period is therefore dependent on the kinetic energy of the electron. It is damped in time by the decay of the resonant state $\exp(-\Gamma_r t/2)$. While the oscillations in energy are known and have been observed in energy, the oscillations in time require a process with a long enough lifetime to be observed around the resonance energy.

In order to be observed, such an oscillation requires long enough lifetimes of the resonant state. The comparably slow sRICD process offers the opportunity to observe and utilize it. An oscillation in time has recently been observed experimentally for an AI process [55]. In both the latter and in our case, a discrepancy between the actual and the fitted lifetime is observed. Given the analytical expressions of this work, we are able to understand this discrepancy. The kinetic energy in Fig. 6 is slightly higher than the kinetic energy corresponding to the resonant state. The further away from the resonance this energy is chosen, the shorter the period of this oscillation. The oscillation is exponentially damped by the lifetime of the decaying state. However, the dynamics of the system are more complex than shown in Eq. (24), because some terms of the resonant and indirect contributions are damped by $\exp(-\Gamma_r t)$ while others are damped by $\exp(-\Gamma_r t/2)$, which can be seen by evaluating the time dependence of the absolute square of Eq. (15). This behavior is effectively only observed in the beginning of the decay, because its contribution becomes small within a short time. Therefore, a fit of the maxima at longer times, where the parts damped by $\exp(-\Gamma_r t)$ can be neglected, to the function $a \exp[-(t-b)/2d] + c$ gives a good estimate of the lifetime $d \approx \tau_r$. The fit in Fig. 6, where the first maximum was omitted, yields a lifetime of

68 fs . The effective overall lifetime of the excited resonant state used as input parameter for the simulations is given by $\frac{1}{\tau_{\text{eff}}} = \frac{1}{\tau_{\text{sRICD}}} + \frac{1}{\tau_o}$ and $\tau_{\text{eff}} = 70\,\text{fs}$ using the parameters given in Table I. The value determined from the fit is slightly lower than this effective lifetime but still matches it very well. This kind of fit can therefore be used to determine the lifetime of the electronic decay process.

V. SUMMARY

We have presented a time-dependent theoretical description of the sRICD and ICD processes investigated with short laser pulses for a model system with frozen nuclei. We suggest sRICD as the primary process. We then imagine that it is possible to quench the sRICD process by a strong laser pulse and thereby initiate the ICD process interference free. We have shown an oscillation of the ionization probability in time, which is general for electronic decay processes. For processes with comparably long lifetimes, such as the ICD processes, this oscillation allows for a new way of measuring the lifetime of the underlying processes. Moreover, the basic formulation opens the door for future investigations in controlling the decay processes and to guide time-resolved experimental studies.

ACKNOWLEDGMENTS

The research of E.F. was supported by the Villum Foundation. The research of L.B.M. was supported by the Villum Kann Rasmussen Centre of Excellence QUSCOPE—Quantum Scale Optical Processes.

APPENDIX: FANO MATRIX ELEMENTS

1. One continuum final state

The time-independent wave function $|\Psi_{\underline{E}}\rangle$ is a solution to the same Hamiltonian as considered in Ref. [43]. We therefore have the same solution

$$|\Psi_{\underline{E}}\rangle = a(\underline{E})\,|r\rangle + \int dE' b_{E'}(\underline{E})\,|E'\rangle\,, \tag{A1}$$

with coefficients

$$a(\underline{E}) = -\frac{V_r}{\sqrt{[\underline{E} - E_r - F(\underline{E})]^2 + \pi^2 V_r^4}}, \tag{A2}$$

$$b_{E'}(\underline{E}) = \frac{V_r a(\underline{E})}{\underline{E} - E'} - \frac{\underline{E} - E_r - F(\underline{E})}{\sqrt{[\underline{E} - E_r - F(\underline{E})]^2 + \pi^2 V_r^4}}\delta(\underline{E} - E'). \tag{A3}$$

Here, $F(\underline{E})$ is a small shift in the energy position of the resonant state $|r\rangle$, which is of second order in V and which we neglect in the following.

The Fano matrix elements of Eq. (13) involving the Fano time-evolution operator can now be solved by contour integration in the negative complex half-plane, where a_{-1} is the first-order residue and we use that $\langle r|r\rangle = 1$, $\langle E|E'\rangle = \delta(E - E')$, and $\langle E|r\rangle = 0$:

$$\langle r|U_F(t'', t')|r\rangle = \int d\underline{E}\, \exp[-i\underline{E}(t'' - t')]\,|a(\underline{E})|^2 \tag{A4}$$

$$= V_r^2 \int d\underline{E}\, \frac{\exp[-i\underline{E}(t'' - t')]}{(\underline{E} - E_r)^2 + \pi^2 V_r^4} \tag{A5}$$

$$= V_r^2 \int d\underline{E}\, \frac{\exp[-i\underline{E}(t'' - t')]}{(\underline{E} - E_r + i\pi V_r^2)\,(\underline{E} - E_r - i\pi V_r^2)} \tag{A6}$$

$$= V_r^2\, \exp[-iE_r(t'' - t')] \int d\tilde{E}\, \frac{\exp[-i\tilde{E}(t'' - t')]}{(\tilde{E} + i\pi V_r^2)\,(\tilde{E} - i\pi V_r^2)} \tag{A7}$$

$$= 2\pi i\, V_r^2 \exp\big[-iE_r\big(t'' - t'\big)\big]\, a_{-1} \tag{A8}$$

$$= \exp[-i(E_r - i\pi V_r^2)(t'' - t')], \tag{A9}$$

$$\int dE'\, \langle r|U_F(t'', t')|E'\rangle = \int d\underline{E} \int dE'\, \exp[-i\underline{E}(t'' - t')]\, a(\underline{E}) b^*_{E'}(\underline{E}) \tag{A10}$$

$$= V_r^2 \int d\underline{E}\, \frac{(\underline{E} - E_r)\exp[-i\underline{E}(t'' - t')]}{(\underline{E} - E_r)^2 + \pi^2 V_r^4} \tag{A11}$$

$$= V_r^2 \int d\underline{E}\, \frac{(\underline{E} - E_r)\exp[-i\underline{E}(t'' - t')]}{(\underline{E} - E_r + i\pi V_r^2)\,(\underline{E} - E_r - i\pi V_r^2)} \tag{A12}$$

$$= V_r^2 \exp[-iE_r(t''-t')] \int d\tilde{E}\ \frac{\tilde{E}\exp[-i\tilde{E}(t''-t')]}{\left(\tilde{E}+i\pi V_r^2\right)\left(\tilde{E}-i\pi V_r^2\right)} \tag{A13}$$

$$= 2\pi i V_r^2 \exp[-iE_r(t''-t')]\, a_{-1} \tag{A14}$$

$$= -i\pi V_r \exp\left[-i\left(E_r - i\pi V_r^2\right)(t''-t')\right]. \tag{A15}$$

2. Two continuum final states

The time-independent wave function $|\Psi_{\underline{E}}\rangle$ is a solution to the same Hamiltonian as considered in Ref. [43]. After neglecting $F(\underline{E})$ as before we therefore have the same solutions

$$|\Psi_{\underline{E}}\rangle = a(\underline{E})\,|r\rangle + \int dE_1' b_{E_1'}(\underline{E})\,|E_1'\rangle + \int dE_2' b_{E_2'}(\underline{E})\,|E_2'\rangle\,, \tag{A16}$$

with coefficients

$$a(\underline{E}) = -\frac{\sqrt{V_r^2+W_r^2}}{\sqrt{(\underline{E}-E_r)^2+\pi^2\left(V_r^2+W_r^2\right)^2}}, \tag{A17}$$

$$b_{E_1'}(\underline{E}) = \frac{V_r a(\underline{E})}{\sqrt{V_r^2+W_r^2}(\underline{E}-E_1')} - \frac{\underline{E}-E_r}{\sqrt{(\underline{E}-E_r)^2+\pi^2\left(V_r^2+W_r^2\right)^2}}\delta(\underline{E}-E_1'), \tag{A18}$$

$$c_{E_2'}(\underline{E}) = \frac{W_r a(\underline{E})}{\sqrt{V_r^2+W_r^2}(\underline{E}-E_2')} - \frac{\underline{E}-E_r}{\sqrt{(\underline{E}-E_r)^2+\pi^2\left(V_r^2+W_r^2\right)^2}}\delta(\underline{E}-E_2'). \tag{A19}$$

The Fano integrals can now be solved by contour integration in the negative complex half-plane, where a_{-1} is the first-order residue and we use that $\langle r|r\rangle = 1$, $\langle E|E'\rangle = \delta(E-E')$, and $\langle E|r\rangle = 0$:

$$\langle r|U_F(t'',t')|r\rangle = \left(V_r^2+W_r^2\right)\int d\underline{E}\ \exp[-i\underline{E}(t''-t')]\,|a(\underline{E})|^2 \tag{A20}$$

$$= \left(V_r^2+W_r^2\right)\int d\underline{E}\ \frac{\exp[-i\underline{E}(t''-t')]}{(\underline{E}-E_r)^2+\pi^2\left(V_r^2+W_r^2\right)^2} \tag{A21}$$

$$= \left(V_r^2+W_r^2\right)\int d\underline{E}\ \frac{\exp[-i\underline{E}(t''-t')]}{\left[\underline{E}-E_r+i\pi\left(V_r^2+W_r^2\right)\right]\left[\underline{E}-E_r-i\pi\left(V_r^2+W_r^2\right)\right]} \tag{A22}$$

$$= \left(V_r^2+W_r^2\right)\exp[-iE_r(t''-t')]\int d\tilde{E}\ \frac{\exp[-i\tilde{E}(t''-t')]}{\left[\tilde{E}+i\pi\left(V_r^2+W_r^2\right)\right]\left[\tilde{E}-i\pi\left(V_r^2+W_r^2\right)\right]} \tag{A23}$$

$$= 2\pi i\left(V_r^2+W_r^2\right)\exp[-iE_r(t''-t')]\,a_{-1} \tag{A24}$$

$$= \exp\{-i\left[E_r - i\pi\left(V_r^2+W_r^2\right)\right](t''-t')\}, \tag{A25}$$

$$\int dE'\,\langle r|U_F(t'',t')|E'\rangle = \int d\underline{E}\int dE'\ \exp[-i\underline{E}(t''-t')]\,a(\underline{E})b_{E'}^*(\underline{E}) \tag{A26}$$

$$= V_r\int d\underline{E}\ \frac{(\underline{E}-E_r)\exp[-i\underline{E}(t''-t')]}{(\underline{E}-E_r)^2+\pi^2\left(V_r^2+W_r^2\right)^2} \tag{A27}$$

$$= V_r\int d\underline{E}\ \frac{(\underline{E}-E_r)\exp[-i\underline{E}(t''-t')]}{\left[\underline{E}-E_r+i\pi\left(V_r^2+W_r^2\right)\right]\left[\underline{E}-E_r-i\pi\left(V_r^2+W_r^2\right)\right]} \tag{A28}$$

$$= V_r\exp[-iE_r(t''-t')]\int d\tilde{E}\ \frac{\tilde{E}\exp[-i\tilde{E}(t''-t')]}{\left[\tilde{E}+i\pi\left(V_r^2+W_r^2\right)\right]\left[\tilde{E}-i\pi\left(V_r^2+W_r^2\right)\right]} \tag{A29}$$

$$= 2\pi i V_r\exp[-iE_r(t''-t')]\,a_{-1} \tag{A30}$$

$$= -i\pi V_r\exp\{-i\left[E_r - i\pi\left(V_r^2+W_r^2\right)\right](t''-t')\}. \tag{A31}$$

[1] L. S. Cederbaum, J. Zobeley, and F. Tarantelli, Giant Intermolecular Decay and Fragmentation of Clusters, Phys. Rev. Lett. **79**, 4778 (1997).

[2] S. Marburger, O. Kugeler, U. Hergenhahn, and T. Möller, Experimental Evidence for Interatomic Coulombic Decay in Ne Clusters, Phys. Rev. Lett. **90**, 203401 (2003).

[3] R. Santra, J. Zobeley, L. S. Cederbaum, and N. Moiseyev, Interatomic Coulombic Decay in van der Waals Clusters and Impact of Nuclear Motion, Phys. Rev. Lett. **85**, 4490 (2000).
[4] U. Hergenhahn, Interatomic and intermolecular Coulombic decay: The early years, J. Electron Spectrosc. Relat. Phenom. **184**, 78 (2011).
[5] T. Jahnke, Interatomic and intermolecular Coulombic decay: The coming of age story, J. Phys. B: At., Mol., Opt. Phys. **48**, 082001 (2015).
[6] E. Fasshauer, Non-nearest neighbor ICD in clusters, New J. Phys. **18**, 043028 (2016).
[7] E. Faßhauer, N. V. Kryzhevoi, and M. Pernpointner, Possible electronic decay channels in the ionization spectra of small clusters composed of Ar and Xe: A four-component relativistic treatment, J. Chem. Phys. **133**, 014303 (2010).
[8] E. Fasshauer, M. Pernpointner, and K. Gokhberg, Interatomic decay of inner-valence ionized states in ArXe clusters: Relativistic approach, J. Chem. Phys. **138**, 014305 (2013).
[9] E. Fasshauer, M. Förstel, S. Pallmann, M. Pernpointner, and U. Hergenhahn, Using ICD for structure analysis of clusters: A case study on coexpanded Ne-Ar clusters, New J. Phys. **16**, 103026 (2014).
[10] M. Förstel, M. Mucke, T. Arion, T. Lischke, M. Pernpointner, U. Hergenhahn, and E Fasshauer, Long-range interatomic Coulombic decay in ArXe clusters: Experiment and theory, J. Phys. Chem. C **120**, 22957 (2016).
[11] E. Fasshauer, M. Förstel, M. Mucke, T. Arion, and U. Hergenhahn, Theoretical and experimental investigation of electron transfer mediated decay in ArKr clusters, Chem. Phys. **482**, 226 (2017).
[12] I. B. Müller and L. S. Cederbaum, Ionization and double ionization of small water clusters, J. Chem. Phys. **125**, 204305 (2006).
[13] N. V. Kryzhevoi and L. S. Cederbaum, Using pH value to control intermolecular electronic decay, Angew. Chem. Int. Ed. **50**, 1306 (2011).
[14] S. D. Stoychev, A. I. Kuleff, and L. S. Cederbaum, Intermolecular Coulombic decay in small biochemically relevant hydrogen-bonded systems, J. Am. Chem. Soc. **133**, 6817 (2011).
[15] N. V. Kryzhevoi and L. S. Cederbaum, Nonlocal effects in the core ionization and Auger spectra of small ammonia clusters, J. Phys. Chem. B **115**, 5441 (2011).
[16] B. Oostenrijk, N. Walsh, J. Laksman, E. P. Mansson, Ch. Grunewald, S. L. Sorensen, and M. Gisselbrecht, The role of charge and proton transfer in fragmentation of hydrogen-bonded nanosystems: The breakup of ammonia clusters upon single photon multi-ionization, Phys. Chem. Chem. Phys. **20**, 932 (2018).
[17] P. H. P. Harbach, M. Schneider, S. Faraji, and A. Dreuw, Intermolecular Coulombic decay in biology: The initial electron detachment from $FADH^-$ in DNA photolyases, J. Phys. Chem. Lett. **4**, 943 (2013).
[18] V. Stumpf, K. Gokhberg, and L. S. Cederbaum, The role of metal ions in x-ray-induced photochemistry, Nat. Chem. **8**, 237 (2016).
[19] B. Boudaïffa, P. Cloutier, D. Hunting, M. A. Huels, and L. Sanche, Resonant formation of DNA strand breaks by low-energy (3 to 20 eV) electrons, Science **287**, 1658 (2000).
[20] E. Brun, P. Cloutier, C. Sicard-Roselli, M. Fromm, and L. Sanche, Damage induced to DNA by low-energy (0–30 eV) electrons under vacuum and atmospheric conditions, J. Phys. Chem. B **113**, 10008 (2009).
[21] X. Pan, P. Cloutier, D. Hunting, and L. Sanche, Dissociative Electron Attachment to DNA, Phys. Rev. Lett. **90**, 208102 (2003).
[22] F. Martin, P. D. Burrow, Z. Cai, P. Cloutier, D. Hunting, and L. Sanche, DNA Strand Breaks Induced by 0–4 eV Electrons: The Role of Shape Resonances, Phys. Rev. Lett. **93**, 068101 (2004).
[23] E. Surdutovich and A. V. Solov'yov, Double strand breaks in DNA resulting from double ionization events, Eur. Phys. J. D **66**, 206 (2012).
[24] E. Alizadeh, T. M. Orlando, and L. Sanche, Biomolecular damage induced by ionizing radiation: The direct and indirect effects of low-energy electrons on DNA, Annu. Rev. Phys. Chem. **66**, 379 (2015).
[25] E. Fasshauer, doi:10.6084/m9.figshare.7808294.v2.
[26] F. Krausz and M. Ivanov, Attosecond physics, Rev. Mod. Phys. **81**, 163 (2009).
[27] A. Kaldun, A. Blättermann, V. Stooß, S. Donsa, H. Wei, R. Pazourek, S. Nagele, C. D. Ott, C. Lin, J. Burgdörfer, and T. Pfeifer, Observing the ultrafast buildup of a Fano resonance in the time domain, Science **354**, 738 (2016).
[28] V. Gruson, L. Barreau, A. Jimenez-Galan, F. Risoud, J. Caillat, A. Maquet, B. Carre, F. Lepetit, J.-F. Hergott, T. Ruchon, L. Argenti, R. Taieb, F. Martin, and P. Salieres, Attosecond dynamics through a Fano resonance: Monitoring the birth of a photoelectron, Science **354**, 734 (2016).
[29] A. I. Kuleff and L. S. Cederbaum, Tracing Ultrafast Interatomic Electronic Decay Processes in Real Time and Space, Phys. Rev. Lett. **98**, 083201 (2007).
[30] K. Schnorr, A. Senftleben, M. Kurka, A. Rudenko, L. Foucar, G. Schmid, A. Broska, T. Pfeifer, K. Meyer, D. Anielski, R. Boll, D. Rolles, M. Kübel, M. F. Kling, Y. H. Jiang, S. Mondal, T. Tachibana, K. Ueda, T. Marchenko, M. Simon, G. Brenner, R. Treusch, S. Scheit, V. Averbukh, J. Ullrich, C. D. Schröter, and R. Moshammer, Time-Resolved Measurement of Interatomic Coulombic Decay in Ne_2, Phys. Rev. Lett. **111**, 093402 (2013).
[31] F. Trinter, J. B. Williams, M. Weller, M. Waitz, M. Pitzer, J. Voigtsberger, C. Schober, G. Kastirke, C. Müller, C. Goihl, P. Burzynski, F. Wiegandt, T. Bauer, R. Wallauer, H. Sann, A. Kalinin, L. Ph. H. Schmidt, M. Schöffler, N. Sisourat, and T. Jahnke, Evolution of Interatomic Coulombic Decay in the Time Domain, Phys. Rev. Lett. **111**, 093401 (2013).
[32] K. Schnorr, A. Senftleben, G. Schmid, S. Augustin, M. Kurka, A. Rudenko, L. Foucar, A. Broska, K. Meyer, D. Anielski, D. Anielski, R. Boll, D. Rolles, M. Kübel, M. F. Kling, Y. H. Jiang, S. Mondal, T. Tachibana, K. Ueda, T. Marchenko, M. Simon, G. Brenner, R. Treusch, S. Scheit, V. Averbukh, J. Ullrich, T. Pfeifer, C. D. Schröter, and R. Moshammer, Time-resolved study of ICD in Ne dimers using FEL radiation, J. Electron Spectrosc. Relat. Phenom. **204**, 245 (2015).
[33] U. Frühling, F. Trinter, F. Karimi, J. B. Williams, and T. Jahnke, Time-resolved studies of interatomic Coulombic decay, J. Electron. Spectrosc. Relat. Phenom. **204**, 237 (2015).
[34] T. Mizuno, P. Cörlin, T. Miteva, K. Gokhberg, A. Kuleff, L. S. Cederbaum, T. Pfeifer, A. Fischer, and R. Moshammer, Time-resolved observation of interatomic excitation-energy transfer in argon dimers, J. Chem. Phys. **146**, 104305 (2017).

[35] T. Takanashi, N. V. Golubev, C. Callegari, H. Fukuzawa, K. Motomura, D. Iablonskyi, Y. Kumagai, S. Mondal, T. Tachibana, K. Nagaya, T. Nishiyama, K. Matsunami, P. Johnsson, P. Piseri, G. Sansone, A. Dubrouil, M. Reduzzi, P. Carpeggiani, C. Vozzi, M. Devetta, M. Negro, D. Facciala, F. Calegari, A. Trabattoni, M. C. Castrovilli, Y. Ovcharenko, M. Mudrich, F. Stienkemeier, M. Coreno, M. Alagia, B. Schütte, N. Berrah, O. Plekan, P. Finetti, C. Spezzani, E. Ferrari, E. Allaria, G. Penco, C. Serpico, G. De Ninno, B. Diviacco, S. Di Mitri, L. Giannessi, G. Jabbari, K. C. Prince, L. S. Cederbaum, Ph. V. Demekhin, A. I. Kuleff, and K. Ueda, Time-Resolved Measurement of Interatomic Coulombic Decay Induced by Two-Photon Double Excitation of Ne_2, Phys. Rev. Lett. **118**, 033202 (2017).

[36] Q. Jing and L. B. Madsen, Dynamics of interatomic Coulombic decay in neon dimers by XUV-pump–XUV-probe spectroscopy, Phys. Rev. A **99**, 013409 (2019).

[37] K. Gokhberg, V. Averbukh, and L. S. Cederbaum, Interatomic decay of inner-valence-excited states in clusters, J. Chem. Phys. **124**, 144315 (2006).

[38] S. Barth, S. Joshi, S. Marburger, V. Ulrich, A. Lindblad, G. Öhrwall, O. Björneholm, and U. Hergenhahn, Observation of resonant interatomic Coulombic decay in Ne clusters, J. Chem. Phys. **122**, 4 (2005).

[39] T. Aoto, K. Ito, Y. Hikosaka, E. Shigemasa, F. Penent, and P. Lablanquie, Properties of Resonant Interatomic Coulombic Decay in Ne Dimers, Phys. Rev. Lett. **97**, 243401 (2006).

[40] S. Kopelke, K. Gokhberg, L. S. Cederbaum, and V. Averbukh, Calculation of resonant interatomic Coulombic decay widths of inner-valence-excited states delocalized due to inversion symmetry, J. Chem. Phys. **130**, 144103 (2009).

[41] A. Knie, A. Hans, M. Förstel, U. Hergenhahn, P. Schmidt, Ph. Reiß, Ch. Ozga, B. Kambs, F. Trinter, J. Voigtsberger, D. Metz, T. Jahnke, R. Dörner, A. I. Kuleff, L. S. Cederbaum, P. V. Demekhin, and A. Ehresmann, Detecting ultrafast interatomic electronic processes in media by fluorescence, New. J. Phys. **16**, 102002 (2014).

[42] A. Hans, L. B. Ltaief, M. Förstel, Ph. Schmidt, Ch. Ozga, Ph. Reiß, X. Holzapfel, C. Küstner-Wetekam, F. Wiegandt, F. Trinter, U. Hergenhahn, T. Jahnke, R. Dörner, A. Ehresmann, Ph. V. Demekhin, and A. Knie, Fluorescence cascades evoked by resonant interatomic Coulombic decay of inner-valence excited neon clusters, Chem. Phys. **482**, 165 (2017).

[43] U. Fano, Effects of configuration interaction on intensities and phase shifts, Phys. Rev. **124**, 1866 (1961).

[44] M. Wickenhauser, J. Burgdörfer, F. Krausz, and M. Drescher, Time Resolved Fano Resonances, Phys. Rev. Lett. **94**, 023002 (2005).

[45] A. Kramida, Yu. Ralchenko, J. Reader, and NIST ASD Team, NIST atomic spectra database (version 5.6.1), online, 2018.

[46] A. Ghosh and N. Vaval, Geometry-dependent lifetime of interatomic Coulombic decay using equation-of-motion coupled cluster method, J. Chem. Phys. **141**, 234108 (2014).

[47] A. Bondi, van der Waals volumes and radii, J. Phys. Chem. **68**, 441 (1964).

[48] E. Fasshauer, ELDEST version 2.0.3, Programme for the time-resolved investigation of electronic decay processes, doi:10.5281/zenodo.3700062, 2020.

[49] E. Jones, T. Oliphant, P. Peterson *et al.*, SciPy: Open source scientific tools for Python, 2001.

[50] T. E. Oliphant, Python for scientific computing, Comput. Sci. Eng. **9**, 10 (2007).

[51] K. J. Millman and M. Aivazis, Python for scientists and engineers, Comput. Sci. Eng. **13**, 9 (2011).

[52] E. Fasshauer, input file, doi:10.6084/m9.figshare.7808348.v1, 2019.

[53] See Supplemental Material at http://link.aps.org/supplemental/10.1103/PhysRevA.101.043414 for video of the time-resolved spectrum sRICD and ICD spectrum, where the second pulse quenches the sRICD process after 100 fs.

[54] M. Wickenhauser, Ph.D. thesis, Vienna University of Technology, 2006.

[55] D. Busto, L. Barreau, M. Isinger, M. Turconi, C. Alexandridi, A. Harth, S. Zhong, R. J. Squibb, D. Kroon, S. Plogmaker, M. Miranda, A. Jimenez-Galan, L. Argenti, C. L. Arnold, R. Feifel, F. Martin, M. Gisselbrecht, A. L'Huillier, and P. Salieres, Time-frequency representation of autoionization dynamics in helium, J. Phys. B: At., Mol., Opt. Phys. **51**, 044002 (2018).

PAPER • OPEN ACCESS

Non-nearest neighbour ICD in clusters

To cite this article: E Fasshauer 2016 *New J. Phys.* **18** 043028

New Journal of Physics
The open access journal at the forefront of physics

Deutsche Physikalische Gesellschaft DPG
IOP Institute of Physics

Published in partnership with: Deutsche Physikalische Gesellschaft and the Institute of Physics

OPEN ACCESS

RECEIVED
9 December 2015

REVISED
17 March 2016

ACCEPTED FOR PUBLICATION
23 March 2016

PUBLISHED
19 April 2016

PAPER

Non-nearest neighbour ICD in clusters

E Fasshauer

Centre for Theoretical and Computational Chemistry, Department of Chemistry, University of Tromsø—The Arctic University of Norway, N-9037 Tromsø, Norway

E-mail: elke.fasshauer@uit.no

Keywords: interatomic coulombic decay, neon clusters, NeAr clusters, lifetimes, bulk and surface atoms, decay widths, icosahedral versus cuboctahedral structure

Abstract

Interatomic Coulombic decay (ICD) is an electronic decay process of excited, ionized systems. It has been shown to occur in a multitude of small and large systems. The effects of more than one possible decay partner are discussed in detail illustrated by simulated ICD electron spectra of NeAr clusters and pure Ne clusters. Hereby, the mostly underestimated contribution of decay with non-nearest neighbours is highlighted. In the neon clusters, the lifetime of the bulk atoms is found to be in excellent agreement with experiment (Jahnke *et al* 2004 *Phys. Rev. Lett.* **93** 173401) while the lifetimes of the surface atoms differ significantly. Hence, the experimental lifetime can not purely be explained by the effect of the number of neighbours. We propose the possibility to investigate the transition from small clusters to the solid state by using the ICD electron spectra to distinguish between icosahedral and cuboctahedral cluster structures.

1. Introduction

The Interatomic Coulombic decay (ICD) is an electronic decay process of an atom or molecule with a sub-outer-valence vacancy involving atoms or molecules of the environment. The decay process is initiated by the creation of the vacancy, which can be achieved in different ways, out of which direct ionization, excitation, an Auger decay and radioactive decay are the most common ones. They are connected to different members of the family of ICD-like processes such as the electron transfer mediated decay (ETMD), the Resonance ICD, the ICD of multiply charged species like after an Auger decay and the classical ICD (see [1, 2] and references therein). In this paper the classical ICD of a sub-outer-valence vacancy in an atom or a molecule (a unit A) will be discussed. After creation of the vacancy in A, it is filled by an electron of the same unit and the excess energy (often called the energy of a virtual photon (vp) ω_{vp}) is transferred to a decay partner B, which subsequently gets ionized:

$$A^{*+} + B \rightarrow A^{+} + B^{+} + e^{-}_{\mathrm{ICD}}.$$

In the final state, the two units A and B are both positively charged, repell each other and thereby undergo a Coulomb explosion. This process was predicted theoretically [3], later the first experimental evidence was found in [4, 5] and the experimental prove was given by Jahnke *et al* [6]. Since then it has been studied in a multitude of different systems such as small and large rare gas clusters [7–15], clusters of small molecules [16–20], quantum dots [21], proteins [22], it is expected to play a role in DNA damage in radiation therapy [23] and may be used to destroy malign tissue [24, 25].

In order to undergo ICD and this process to be observable, two criteria have to be fulfilled: the energy and the coupling criterion. The energy criterion is a rephrasing of the energy conservation stating that a decay can only happen if the energy suffices. In case the energy of the doubly ionized final state is higher than the energy of the singly ionized initial state, the ICD is energetically forbidden. The coupling criterion requires the decay process to be sufficiently efficient to outperform other decay pathways such as radiative decay by emission of a photon or coupling to the nuclear degrees of freedom in molecules. The corresponding property is the decay width $\Gamma = \frac{\hbar}{\tau}$, which is inversely proportional to the lifetime τ and proportional to the decay rate $\frac{1}{\tau}$.

The ICD process was so far mostly discussed for the case of decay partners in the direct vicinity, because the decay with decay partners further away were considered to be negligible due to their decay width. Therefore, the decay was studied in clusters up to 13 neon atoms of equal interatomic distances considering the initial ionization of only the central atom and not the other ones [9]. The largest cluster had a cuboctahedral structure. In this study, a higher than linear dependence of the decay width on the number of neighbours was observed. A linear dependence would be expected for equal decay partners at equal distances from the initially ionized atom in the same environment. Since the decay width in the asymptotic limit shows an $1/\omega_{vp}^4$-behaviour on the energy of the vp, which is decreased for a stabilized final state, this additional feature can be related to the better energetic stabilization of the doubly ionized final state in larger clusters [26].

It was shown in earlier studies [15, 26–28] that decay pathways with decay partners at larger distances need to be included for larger systems for two reasons:

(i) In cluster structures more than one pair of units can consist of the same atom types and have the same interatomic distance. Hence, they are indistinguishable in the spectrum. Since the decay rate as well as the peak intensity is proportional to the number of such pairs, the peaks stemming from several pairs are favoured compared to other ones at similar distances. Therefore, peaks stemming from decays with distant decay partners can be visible in ICD spectra of clusters [15].

(ii) The opening of ICD-like decay channels depends on the interatomic distance, which is characteristic for every atom pair. A channel being closed at the distance to the most direct neighbours might be open for interaction partners at slightly larger distances. If this particular decay channel is more efficient than other decay channels being open for the decay with direct neighbours, it can still be visible in the spectrum or even outperform the slower decay mechanism and hence they have to be taken into account. We have shown this for the case of ICD versus the ETMD3 process in mixed ArXe clusters [26, 28].

Especially in the biological systems, in which ICD is discussed to play an important role [23–25] the DNA is surrounded by multiple moving water molecules which can act as decay partners. Therefore, understanding the effect of non-nearest neighbour decay will be crucial to study these systems. However, this feature of non-nearest neighbour ICD has so far not been addressed by itself and we will fill the gap in this paper.

For a test system we choose rare gas clusters. These are favourable for the investigation of basic features both from a theoretical and an experimental point of view. Their spherical symmetry and their very localized orbitals allow for an comparably easy theoretical description of the decay processes. The experimental techniques to produce rare gas clusters are well established via variety of experimental and theoretical studies [5, 29–31]. This makes these clusters a convenient target with controlled and predictable cluster conditions available at sufficient target densities for extended time periods as required in the here described experiments. At the same time, the structure of the clusters reveals an interesting matter of research. Small, ideal clusters exhibit an icosahedral structure while large clusters have a cuboctahedral structure, which infinitely extended, yields the solid state face-centered-cubic (fcc) structure. In the solid state, every single atom is surrounded by twelve other atoms in the same distance. Surface atoms or even atoms at edges and vertices are rare compared to the number of atoms in the bulk. However, in small clusters most atoms are surface atoms and are therefore surrounded by less than the optimal 12 atoms. In the icosahedral cluster structure the interatomic distances between different layers are shorter than between atoms of the same layer. Therefore, this structure is favourable in small clusters with a large surface-to-bulk ratio. Together with the structure change from icosahedral to cuboctahedral the clusters' properties gradually change towards those of solids and conductivity as well as magnetizability can be observed [32]. It is still unclear at which cluster size the favourable structure changes from an icosahedral to an cuboctahedral structure. Numbers in the range of 800–3000 atoms have been reported [33, 34]. We propose to use the ICD to be a possible tool to distinguish between icosahedral and cuboctahedral cluster structures using the different distance patterns in the cluster structures.

We will therefore first introduce the theoretical concepts in section 2, present the computational details in section 3, discuss the distance dependency of the ICD in general in section 4 and then discuss the NeNe ICD part of the ICD spectra of NeAr clusters [15] in section 5.1. Here we will discuss the peaks and their origin in detail and thereby raise the question, what a *nearest neighbour* is supposed to be. From our conclusions we propose the possibility to distinguish cluster structures of ideal icosahedral and cuboctahedral structures using ICD spectra in section 5.2.

2. Theoretical background

In order to simulate the ICD electron spectra for a given cluster structure, the kinetic energies of the ICD electrons E_{ICD} and the corresponding decay widths of all pairs have to be determined. The ICD electron energies

Table 1. Experimental values for the single ionization potentials [15] used for the estimation of the decay widths.

Indicator	Value
SIP(Ne2s)	47.75 eV
SIP(Ne2p)	21.10 eV
SIP(Ar3p)$_{c<3}$	15.40 eV
SIP(Ar3p)$_{c\geqslant 3}$	15.20 eV

are given by the differences between the initial state and the final state energies E_{in} and E_{fin}, respectively. The initial state energy is given by the single ionization potential (SIP) of the sub-valence electron of the entire system and the final state energy is given by the double ionization potential. In the asymptotic limit, which is a reasonably good approximation for weakly bound systems, the initial state energy is approximated by the SIP of the initially ionized unit X_{in} and the final state energy can be approximated by the sum over the SIPs of the electron donating unit X_{D} and the electron emitting unit X_{E} ionized in the final state as well as the Coulomb repulsion between two point charges at the interatomic distance R

$$E^{\beta}_{\mathrm{ICD}} = E^{\beta}_{\mathrm{in}} - E^{\beta}_{\mathrm{fin}}, \tag{1}$$

$$E_{\mathrm{in}} = \mathrm{SIP}(X_{\mathrm{in}}), \tag{2}$$

$$E^{\beta}_{\mathrm{fin}} = \mathrm{SIP}(X^{\beta}_{\mathrm{D}}) + \mathrm{SIP}(X^{\beta}_{\mathrm{E}}) + \frac{1}{R}. \tag{3}$$

Here, β denotes the selected decay channel.

Following Wentzel [35], Feshbach [36, 37] and Fano [38] the decay width is given by

$$\Gamma_{\beta}(E_{\mathrm{res}}) = 2\pi \; |\langle |\Phi_{\mathrm{in}}|H_{\mathrm{f}}|\chi_{\beta}|\rangle|^2. \tag{4}$$

Here, the bound and ionized initial state is described by $|\Phi_{\mathrm{in}}\rangle$ and the final continuum state of a particular decay channel β is given by $|\chi_{\beta}\rangle$. Its challenging description involving both bound and continuum states can amongst others be achieved by the FanoADC-Stieltjes approach, where a subset of the 2-hole-1-particle (2h1p) functions within the algebraic diagrammatic construction (ADC) are used to mimic the final state function $|\chi_{\beta}\rangle$. By these means calculated discrete energies and corresponding transitions moments are then used to construct a continuous function, which is evaluated at the resonance energy approximated by the single ionization potential corresponding to the initial state E_{in}. For a more detailed description of the method and comparison to other approaches see [39, 40] and references therein.

3. Computational details

The cluster structures used were constructed to have an ideal icosahedral or fcc geometry with optional additional incomplete outermost shells. These are based on the van der Waals radii for neon $r_{\mathrm{Ne}} = 1.54$ Å and argon $r_{\mathrm{Ar}} = 1.88$ Å [41]. In case of the NeAr clusters two of those cluster structures from [15], where the theoretical and experimental argon content in the cluster, the NeAr-ICD to total ICD ratio and the peak position of the NeAr-ICD peak matched best for a given manifold (set) of clusters produced under certain experimental conditions, have been chosen. These are $C_{\mathrm{Ar}} = 3$, $C_{\mathrm{Ne}} = 1$, $S_{\mathrm{Ne}} = 7$ for set 3 and $C_{\mathrm{Ar}} = 2$, $C_{\mathrm{Ne}} = 1$, $S_{\mathrm{Ne}} = 13$ for set 5 where we used the same nomenclature as in [15]. Hence, C_{Ar} denotes the edge length of the argon core, C_{Ne} denotes the number of complete neon shells around the argon core and S_{Ne} denotes the number of triangular surfaces additionally covered by neon atoms.

The calculations to obtain the ICD electron spectra of all cluster structures were performed with the program HARDRoC [42] based on the decomposition of the cluster into pairs. Every pair with the same distance is treated equally. This includes the assumption that every neon atom is ionized with the same probability [15, 43]. It uses experimental ionization energies shown in table 1 and curves fitted to the decay width of the NeNe ICD of [10] and the NeAr decay widths of [15]. These fitted curves yield lifetimes $\tau = \frac{\hbar}{\Gamma}$ at the corresponding equilibrium distances of $\tau_{\mathrm{NeNe}} = 60$ fs and $\tau_{\mathrm{NeAr}} = 44$ fs.

4. Decay with decay partners at different distances

To fully understand the spectra of clusters with several possible initially ionized atoms with multiple decay partners it is necessary to understand the properties of the decay of a single pair of atoms. As can be seen from

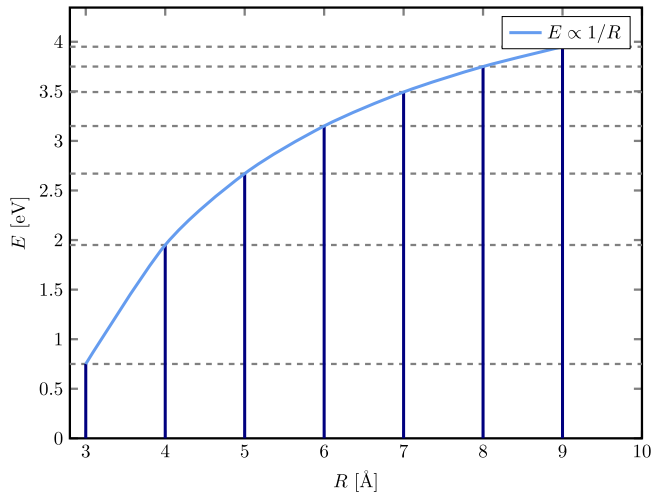

Figure 1. Kinetic energy of the ICD electron depending on the interatomic distance of the two atoms in an isolated pair involved in the decay within the asymptotic approximation. The kinetic energy shows a $1/R$ behaviour and hence distance changes at small distances lead to larger changes in the kinetic energy than at larger distances.

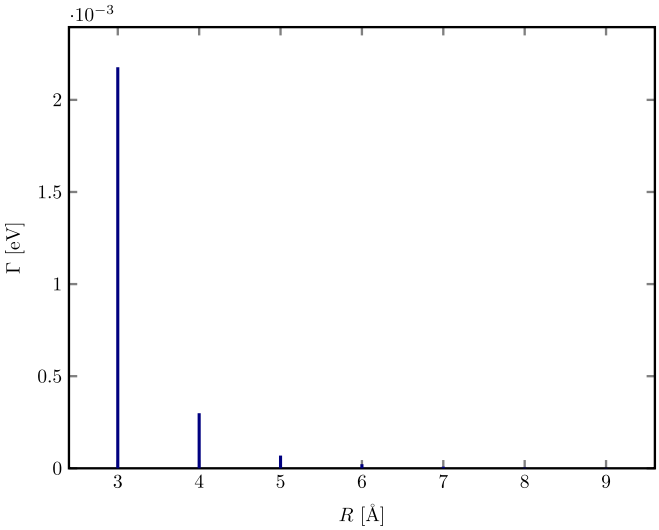

Figure 2. Decay widths for different interatomic distances following an asymptotic $1/R^6$-behaviour. For distances larger than twice the shortest distance considered the peaks are not visible in this plot.

equations (1)–(3), the kinetic energy of the ICD electron follows an $1/R$-behaviour shown in figure 1 for the case of a neon dimer at different distances.

From this diagram it can already be seen that the kinetic energies stemming from equidistant peaks of 3, 4, 5, … , 9 Å are not equidistant in their energy difference but rather decrease for an increasing interatomic distance.

The corresponding decay widths Γ depending on the interatomic distance are shown in figure 2. They show an asymptotic $1/R^6$-behaviour such that the decay widths from an interatomic distance of 7 Å on are too small to be seen in the figure. This means that in case of a neon dimer with an internuclear distance of 3 Å, a decay with one decay partner at twice the internuclear distance of the neon dimer is very unlikely, but that interactions with decay partners at shorter distances can not in general be neglected.

A similar picture is given by the hypothetical ICD-electron spectrum for decay partners at distances of 3, 4, …, 9 Å shown in figure 3. Here, the kinetic energy of the ICD electron is depicted on the abscissa while the decay width Γ is plotted on the ordinate. Since the decay width is proportional to the decay rate and hence the decay probability, these spectra can directly be compared to experimental ICD electron spectra.

The first and dominant peak stems from the decay with a decay partner at a distance of 3 Å. The energy distance to the next peak stemming from a decay with a decay partner with an internuclear distance of 4 Å is found at a 1.20 eV higher kinetic energy and the energy difference to the next peak stemming from a 5 Å distant

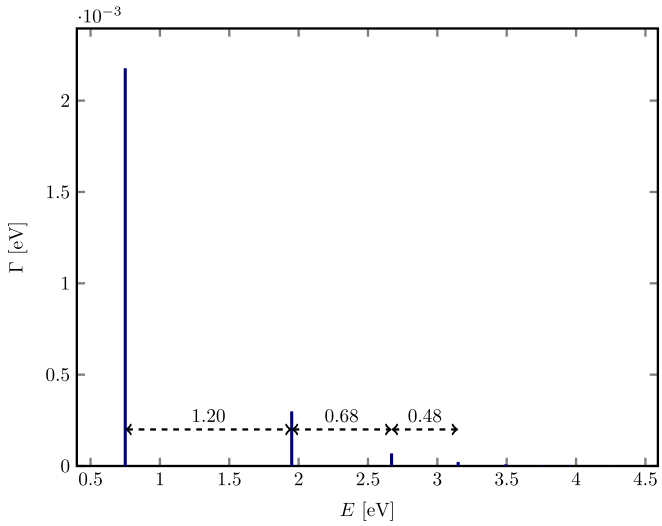

Figure 3. ICD electron spectrum for interaction partner distances of 3 , 4 , 5 , … ,9 Å. The energy difference between equidistant interaction partners decreases with increasing distance. For the case of Ne_2 pairs these energy differences between the peaks stemming from different interatomic distances are given by: 3 Å, 4 Å → 1.20 eV, 4 Å, 5 Å → 0.68 eV and 5 Å, 6 Å → 0.48 eV. This means that the spectrum is better resolved for smaller distances and that small distance changes like vibrations will mainly affect this lower energy part of the spectrum.

decay partner is further 0.68 eV higher. The increase of kinetic energy of the ICD electron is caused by a decrease of Coulomb repulsion between the interaction partners in the final state and therefore, the additional excess in energy is converted into kinetic energy of the emitted ICD electron. The energy difference between the peaks shown in figure 3 decreases with an increasing distance of decay partners and at the same time the kinetic energy of the ICD electron. This means that for small interatomic distances and comparably low kinetic energies of the ICD electron, the energy spectrum has a higher resolution of the interatomic distances. Therefore, a peak structure might be visible for the decay with nearest neighbours (or the closest atoms with energetically allowed decay channels) but not necessarily for all different kinds of interaction partners at larger distances.

5. ICD in clusters

5.1. NeAr clusters

After ionization from the Ne2s, a heteronuclear NeAr cluster can decay via two competing pathways:

$$\mathrm{Ne}(2s^{-1}) + \mathrm{Ne} \rightarrow \mathrm{Ne}(2p^{1}) + \mathrm{Ne}(2p^{-1}) + e^{-}_{\mathrm{ICD}},$$
$$\mathrm{Ne}(2s^{-1}) + \mathrm{Ar} \rightarrow \mathrm{Ne}(2p^{-1}) + \mathrm{Ar}(3p^{-1}) + e^{-}_{\mathrm{ICD}}$$

in which the excess energy gained by filling the Ne2s vacancy is transferred to either another neon atom or to an argon atom. Since the lifetimes of the NeNe-ICD and the NeAr-ICD are of the same order of magnitude, both are visible in the secondary electron spectrum (see figure 2 of [15]). The two signals are well separated in energy and both consist of a main peak and a shoulder at higher kinetic energies of the ICD electron. We earlier showed a clear geometry dependence of peak intensity relation of the NeNe-ICD and NeAr-ICD and utilized this property to determine the structure of heteroatomic rare gas clusters [15].

The peak structure of one main peak and a shoulder at higher energies has been discussed for the NeAr before. Theoretical investigations indicate that the shape might be caused by different vibrational levels of the NeAr dimer ($v = 0, 1, 2$) being populated prior to the initial ionization, because the calculated lifetimes of the intermediate states were too short to allow for nuclear dynamics [44]. There, the ratio of the population of the three vibrational levels 10:5:4 was chosen to yield a spectrum close to the experimental spectrum of NeAr clusters. However, recent experimental results of the ICD in the NeAr dimer show a symmetric peak without a shoulder [45]. In order to explain this, the authors assume a bond contraction of the $Ne^{+}Ar$ to happen prior to the decay. This nuclear rearrangement would contradict the theoretically predicted lifetime of the system and they therefore propose the prior value to be wrong and give an estimate for a higher lifetime. We would like to emphasize the possibility that mainly the vibrational ground state was populated at the temperatures at which the experiment was conducted and that the theoretically predicted lifetimes are correct. Since the shoulder appears in the spectrum of clusters only and not in the dimer spectra, we interpret these experimental results of

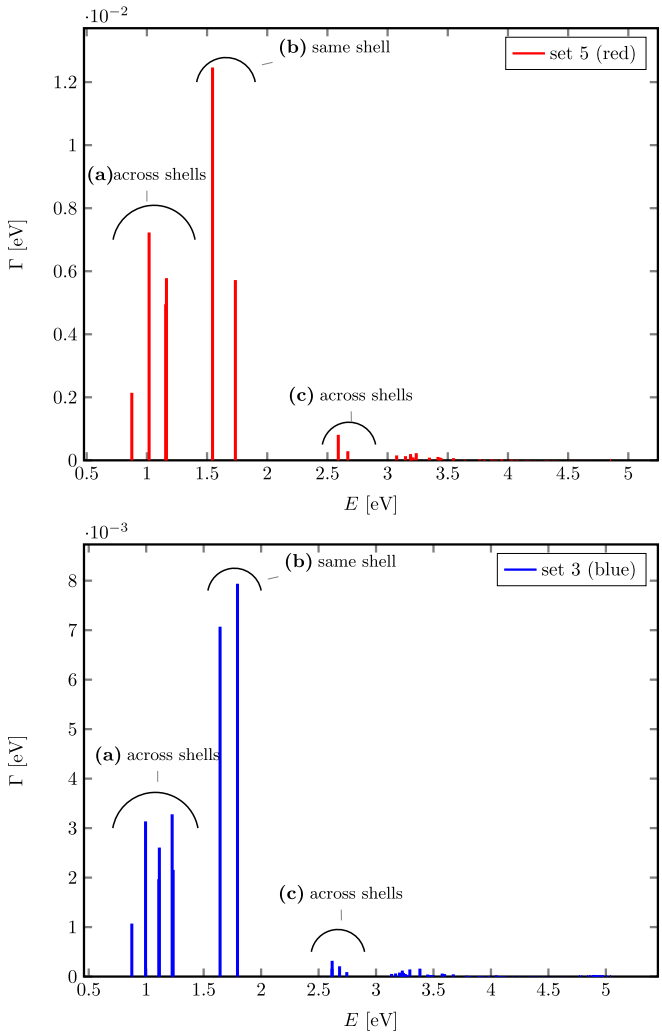

Figure 4. ICD spectra for the NeNe-ICD part of the structures of set 3 and set 5 of the NeAr clusters in [15] plotted as stick spectra. The different peak groups resemble different pair types within the NeAr clusters. The lowest energy peaks ((a)) refer to nearest neighbours of different shells, the peak group (b) refers to nearest neighbours within one shell and the peak group (c) refers to next-nearest neighbours between adjacent shells. The other peaks contain both peaks stemming from pairs within the same shell as well as pairs consisting of atoms of different shells. In this representation the contribution of the peaks around 3 eV is easily underestimated. After folding the spectrum with many close lying small peaks they will add up to yield a visible peak or shoulder (compare [15]).

the dimer to confirm our findings, that the shoulder stems from ICD with interaction partners of the next shell [15].

In the neon dimer several vibrational states of the ionized initial state are involved in the decay [7]. It has furthermore been shown, that the experimentally determined lifetime of $\tau_{\mathrm{NeNe}} = 150 \pm 50$ fs [46] is only in agreement with those theoretical lifetime calculations that explicitly include nuclear dynamics of the intermediate state [47]. However, the early lifetime measurements in neon clusters with a mean cluster size of $< N > = 900$ atoms show a lifetime of 30 fs for surface atoms and 6 fs for bulk atoms. This lifetime decrease is caused by the possibility to decay with several decay partners. Nuclear dynamics occur in the range of tens of femtoseconds in the dimer. Additionally, the driving force for a bond contraction after the initial ionization is higher in dimers than in clusters, where one bond contraction usually leads to several bond elongations. Therefore, we consider the influence of nuclear dynamics on the lifetime to be sufficiently small to be able to neglect them in clusters in a first description [5, 9]. In the following, we will focus on the NeNe-ICD part of the ICD electron spectra of the NeAr clusters and analyze them in more detail.

In figure 4 the ICD electron spectra for the NeNe-ICD part of heterogeneous clusters are shown as stick spectra for set 3 and set 5. Hereby, we stick to the naming and the color code of [15]. Both spectra exhibit a similar pattern of peak groups. The groups are found around 1.0 eV (group (a)), around 1.7 eV (group (b)), around 2.6 eV (group (c)) and from 3 to 4 eV. The peak groups can be assigned to atom pairs within the cluster. For group (a) the peaks stem from decays between two nearest neighbour atoms of two different shells, while group (b) stems from the decay partners being nearest neighbours in the same shell. Group (c) can be assigned to

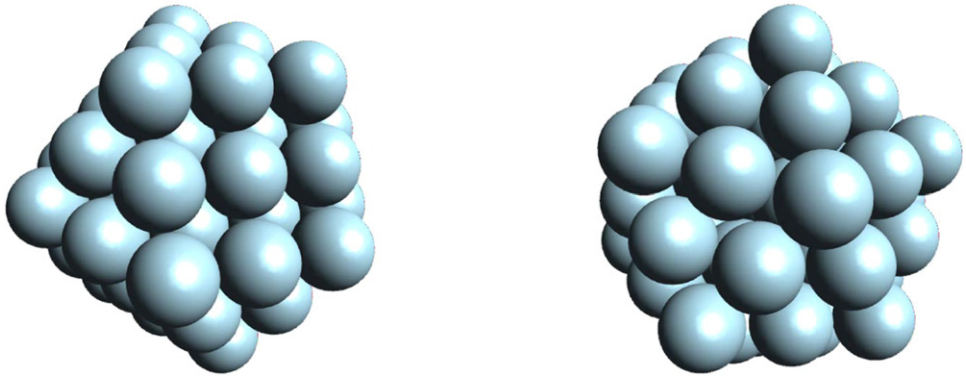

Figure 5. Cluster structures of the 55 atom Ne clusters with cuboctahedral structure (left) and icosahedral structure (right).

Table 2. Calculated decay widths and lifetimes of bulk and surface atoms for icosahedral and cuboctahedral clusters of 55 and 923 atoms.

		Atoms	Γ (meV)	τ (fs)
Icosahedral	Bulk	55	125	5.3
	Surface	55	67	9.8
	Bulk	923	126	5.2
	Surface	923	81	8.1
Cuboctahedral	Bulk	55	140	4.7
	Surface	55	78	8.4
	Bulk	923	147	4.5
	Surface	923	95	7.0

non-nearest neighbours in adjacent shells and the other peaks stem from a mixture of pairs which cannot unambigiously be categorized because different kinds of peaks intersect each other.

Obviously, the peak groups have a fine structure which originates from different positions of the decay partners within a shell (face, egde or vertex). For the investigated ideal icosahedral structures, these pairs of group (a) are from low to high kinetic energies: vertex–vertex, edge–edge, edge–face and face–face. Due to vibrational broadening of the peaks the experimental observation of this fine structure is unlikely in neon clusters.

Concluding these findings, there is not neccessarily only one kind of nearest neighbours in clusters. Even the next-nearest neighbours are closer to twice the interatomic distance of the closest pair with an open decay channel. Therefore, also non-nearest decay partners need to be taken into account in order to simulate ICD spectra of clusters. It can be considered safe to neglect decay partners at sufficiently larger distances than twice the closest interatomic distance between decay partners with open channels.

5.2. Neon clusters: icosahedral versus cuboctahedral structure of clusters

We study two cluster structures (shown in figure 5), where one has an idealized icosahedral and the other one has an idealized cuboctahedral structure for clusters of both 55 and 923 atoms. They hence consist of 13 (561) core and 42 (362) surface atoms.

It was predicted theoretically and proven experimentally that the lifetimes of ionized bulk atoms is shorter than of ionized surface atoms due to the smaller number of direct neighbours of surface atoms [5, 9]. The experimentally determined lifetimes are $\tau_{\mathrm{surf}} = 30$ fs and $\tau_{\mathrm{bulk}} = 6 \pm 1$ fs [5]. For our 55 and 923 atom cluster the decay widths and lifetimes are listed in table 2.

In all cases, our results confirm the shorter lifetimes of the bulk atoms compared to the surface atoms. Both for the icosahedral and for the cuboctahedral cluster structure the lifetime of the bulk atoms is almost independent of the cluster size and the difference is maximum 0.2 fs. This can be explained by the very similar environments of bulk atoms in smaller and larger clusters. The lifetimes of the surface atoms however are smaller for the larger cluster sizes. In small clusters, the number of face surface atoms is small compared to the number of edge and vertex atoms in the surface. The larger the clusters are, the larger is the relative number of the surface atoms. These surface atoms in face positions have more direct neighbours than atoms in vertex

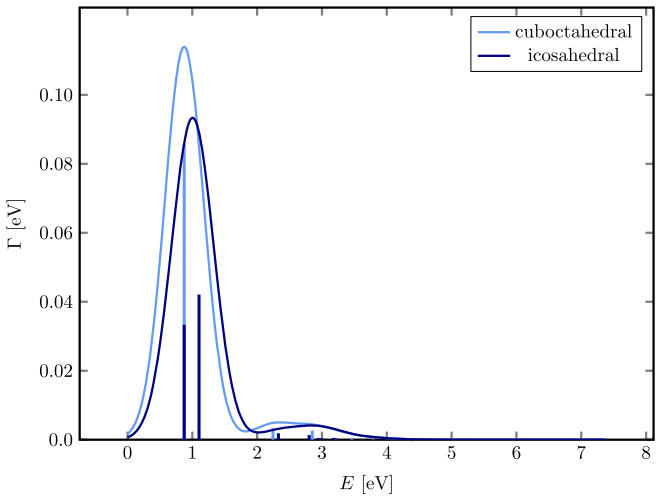

Figure 6. ICD spectra of pure neon clusters consisting of 55 atoms in icosahedral and cuboctahedral structure. In clusters with an ideal cuboctahedral structure all interatomic distances are the same and hence only one peak for each shell around any atom in the cluster is to be expected. In ideal icosahedral clusters the interatomic distances between atoms within the same shell and between atoms in neighbouring atoms are different. Therefore two peaks for interactions partners at different distances can be expected. This feature might help to experimentally identify the underlying structure of clusters.

positions. Therefore, our estimated lifetime of the average surface atoms in the small clusters should be slightly larger than in larger clusters.

For both the icosahedral and the cuboctahedral cluster structures the lifetimes of the bulk atoms are in excellent agreement with experiment. However, the theoretical lifetimes of the surface atoms are significantly smaller than the experimental lifetime. Assuming that the experimental lifetimes are correct, we have to consider three error sources: (1) the nuclear motion excluded in our approach, (2) different cluster structures, and (3) a different stabilization of charges between the inner-valence ionized and the outer-valence ionized atom compared to the bulk.

Cluster structures with larger interatomic distances of the surface atoms between each other and the core atoms would explain the higher experimental lifetimes of the surface atoms. These could be caused by non-ideal structures due to the clusters' temperature.

It remains to discuss the influence of the different charge stabilizations of inner- and outer-valence vacancies. The decay width is proportional to $\frac{1}{\omega_{\mathrm{vp}}^4}$ where the energy of the vp is given by

$$\omega_{\mathrm{vp}} = \mathrm{SIP}(X_{\mathrm{in}}) - \mathrm{SIP}(X_{\mathrm{D}}). \tag{5}$$

If the stabilization difference of the inner-valence vacancy between the bulk and the surface atoms is larger than the corresponding difference of the outer-valence vacancy, the transferred energy is increased in case of the surface atoms ($\omega_{\mathrm{vp,surf}} > \omega_{\mathrm{vp,bulk}}$). As a consequence, the decay width is decreased and the lifetime is increased. Unfortunately, only the initial state energy differences are to be found in the literature [5]. Hence, a validation of this cause is currently not possible.

Before discussing the ICD spectra of the icosahedral and cuboctahedral cluster structures shown in figure 6, we would like to recall that clusters with an icosahedral structure have shorter interatomic distances between shells than within the same shell. In terms of the ICD, different groups of nearest neighbours exist, one within the same shell and one between adjacent shells. This is characteristic for icosahedral cluster structures. Cuboctahedral cluster structures on the other hand are characterized by only one interatomic distance. Therefore, icosahedral cluster structures should be distinguishable from cuboctahedral clusters by the number of peaks, which can be seen in figure 6.

Two experimental ICD electron spectra of clusters with a mean cluster size $<N>$ of 70 and 209 atoms are available in the literature [4, 48]. The first experimental spectrum for clusters with $<N> = 70$ shows a very broad ICD electron peak without an unambiguously assignable peak structure, whereas the later results show a main peak of ICD electrons and a smaller peak at slightly higher kinetic energies (at around 3 eV) that was not even assigned to be an ICD peak in the original work. This peak corresponds to the decay with non-nearest neighbours in the adjacent shell. However, a further peak structure is not visible.

Whether or not the cluster structures would be distinguishable in experiment will depend on the vibrational broadening of the peaks, the experimental resolution and difference of the interatomic distances and hence the energy difference of the peaks in the spectrum of the icosahedral structure. In this proof-of-principle discussion

we chose neon clusters for comparison with experiment but for the distinction of cluster structures it might be recommendable to choose atoms with larger internuclear distances in clusters.

6. Summary

We have discussed two of the three aspects one needs to take into account to simulate the ICD spectrum of rare gas clusters properly. Due to the nature of clusters, a neon atom ionized in the inner-valence will have several decay partners at different distances. The larger the interatomic distance is the higher is the kinetic energy of the ICD electrons which will yield a multitude of peaks in the spectrum. These are then weighted by the decay width, which depends on the interatomic distance of the decay partners but also needs to be scaled by the number of pairs of the same distance. The manifold of all different decay events will then yield the spectrum.

When applying these aspects to cluster structures, one finds that not only the nearest neighbours contribute to the spectrum, but several other decay partners do as well. Decay partners until a distance of at least twice the distance of the clostest decay partners should be taken into account. In clusters with an icosahedral cluster structure this is especially important because the smallest interatomic distance between atoms of the same and atoms of different layers is different, but both distances are comparable. This leads to a different number of peaks in the spectra which might help to distinguish between clusters of icosahedral and cuboctahedral cluster structure.

While the theoretical lifetime of the bulk atoms show an excellent agreement with experiment, the lifetimes of the surface atoms differ significantly. This deviation might be caused by different static cluster structures than taken into account in this work, by different energetic stabilization of charges or by nuclear dynamics. Which of these reasons explains the experiment can not be determined at the moment. Experimentally determined photoelectron spectra of the outer valence of high resolution in neon clusters would help to solve this puzzle.

Acknowledgments

Funding from the Research Council of Norway through a Centre of Excellence Grant (Grant No. 179568/V30) is gratefully acknowledged.

References

[1] Hergenhahn U 2011 Interatomic and intermolecular coulombic decay: the early years *J. Electron Spectrosc. Relat. Phenom* **184** 78
[2] Jahnke T 2015 Interatomic and intermolecular Coulombic decay: the coming of age story *J. Phys. B: At. Mol. Opt. Phys.* **48** 082001
[3] Cederbaum L S, Zobeley J and Tarantelli F 1997 Giant intermolecular decay and fragmentation of clusters *Phys. Rev. Lett.* **79** 4778
[4] Marburger S, Kugeler O, Hergenhahn U and Möller T 2003 Experimental evidence for interatomic coulombic decay in Ne clusters *Phys. Rev. Lett.* **90** 203401
[5] Öhrwall G *et al* 2004 Femtosecond interatomic coulombic decay in free neon clusters: large lifetime differences between surface and bulk *Phys. Rev. Lett.* **93** 173401
[6] Jahnke T *et al* 2004 Experimental observation of interatomic Coulombic decay in neon dimers *Phys. Rev. Lett.* **93** 163401
[7] Santra R, Zobeley J, Cederbaum L S and Moiseyev N 2000 Interatomic Coulombic decay in van der Waals clusters and impact of nuclear motion *Phys. Rev. Lett.* **85** 4490
[8] Santra R, Zobeley J, Cederbaum L S and Tarantelli F 2001 Intermolecular Coulombic decay of clusters *J. Electron Spectrosc. Relat. Phenom.* **41** 114–6
[9] Santra R, Zobeley J and Cederbaum L S 2001 Electronic decay of valence holes in clusters and condensed matter *Phys. Rev.* B **64** 245104
[10] Averbukh V and Cederbaum L S 2006 Calculation of interatomic decay widths of vacancy states delocalized due to inversion symmetry *J. Chem. Phys.* **125** 094107
[11] Lundwall M *et al* 2007 Self-assembled heterogeneous argon/neon core-shell clusters studied by photoelectron spectroscopy *J. Chem. Phys.* **126** 214706
[12] Jahnke T *et al* 2010 Ultrafast energy transfer between water molecules *Nat. Phys.* **6** 139
[13] Förstel M, Arion T and Hergenhahn U 2013 Measuring the efficiency of interatomic Coulombic decay in Ne clusters *J. Electron Spectrosc. Relat. Phenom.* **191** 16
[14] Mucke M, Arion T, Förstel M, Lischke T and Hergenhahn U 2015 Competition of inelastic electron scattering and interatomic Coulombic decay in Ne clusters *J. Electron Spectrosc. Relat. Phenom.* **200** 232
[15] Fasshauer E, Förstel M, Pallmann S, Pernpointner M and Hergenhahn U 2014 Using ICD for structure analysis of clusters: a case study on coexpanded Ne–Ar clusters *New J. Phys.* **16** 103026
[16] Zobeley J, Cederbaum L S and Tarantelli F 1998 Highly excited electronic states of molecular clusters and their decay *J. Chem. Phys.* **108** 9737
[17] Pernpointner M, Knecht S and Cederbaum L S 2006 Ionization spectra and electronic decay in small iodide clusters: fully relativistic results *J. Chem. Phys.* **125** 034309
[18] Müller I B and Cederbaum L S 2006 Ionization and double ionization of small water clusters *J. Chem. Phys.* **125** 204305
[19] Kryzhevoi N V and Cederbaum L S 2011 Using pH value to control intermolecular electronic decay *Angew. Chem., Int. Ed.* **50** 1306
[20] Ghosh A, Pal S and Vaval N 2013 Study of interatomic Coulombic decay of Ne(H2O)n ($n = 1, 3$) clusters using equation-of-motion coupled-cluster method *J. Chem. Phys.* **139** 064112
[21] Bande A 2013 Electron dynamics of interatomic coulombic decay in quantum dots induced by a laser field *J. Chem. Phys.* **138** 214104

[22] Harbach P H P, Schneider M, Faraji S and Dreuw A 2013 Intermolecular coulombic decay in biology: the initial electron detachment from FADH-in DNA photolyases *J. Phys. Chem. Lett.* **4** 943
[23] Alizadeh E, Orlando T M and Sanche L 2015 Biomolecular damage induced by ionizing radiation: the direct and indirect effects of low-energy electrons on DNA *Annu. Rev. Phys. Chem.* **66** 379
[24] Gokhberg K, Kolorenč P, Kuleff A I and Cederbaum L S 2014 Site- and energy-selective slow-electron production through intermolecular Coulombic decay *Nature* **505** 661
[25] Trinter F *et al* 2014 Resonant Auger decay driving intermolecular Coulombic decay in molecular dimers *Nature* **505** 664
[26] Fasshauer E, Pernpointner M and Gokhberg K 2013 Interatomic decay of inner-valence ionized states in ArXe clusters: relativistic approach *J. Chem. Phys.* **138** 014305
[27] Kryzhevoi N V, Averbukh V and Cederbaum L S 2007 High activity of helium droplets following ionisation of systems inside those droplets *Phys. Rev.* B **76** 094513
[28] Fasshauer E, Förstel M, Mücke M, Pernpointner M and Hergenhahn U in preparation
[29] Hagena O F and Obert W 1972 Cluster formation in expanding supersonic jets: effect of pressure, temperature, nozzle size, and test gas *J. Chem. Phys.* **56** 1793–802
[30] Hagena O F 1981 Nucleation and growth of clusters in expanding nozzle flows *Surf. Sci.* **106** 101
[31] Hagena O F 1987 Condensation in free jets: comparison of rare gases and metals *Z. Phys.* D **4** 291
[32] Benfield R E 1992 Mean coordination numbers and the non-metal-metal transition in clusters *J. Chem. Soc. Faraday Trans.* **88** 1107
[33] Hartke B 2002 Structural transitions in clusters *Angew. Chem., Int. Ed.* **41** 1468
[34] Pahl E, Calvo F, Koči L and Schwerdtfeger P 2008 Accurate melting temperatures for neon and argon from ab initio Monte Carlo simulations *Angew. Chem., Int. Ed.* **47** 8207
[35] Wentzel G 1927 Über strahlungslose quantensprünge *Z. Physik.* **43** 524
[36] Feshbach H 1958 Unified theory of nuclear reactions *Ann. Phys.* **5** 357
[37] Feshbach H 1962 A unified theory of nuclear reactions: II *Ann. Phys* **19** 287
[38] Fano U 1961 Effects of configuration interaction on intensities and phase shifts *Phys. Rev.* **124** 1866–78
[39] Averbukh V and Cederbaum L S 2005 Ab initio calculation of interatomic decay rates by a combination of the fano ansatz, Green's-function methods, and the stieltjes imaging technique *J. Chem. Phys.* **123** 204107
[40] Fasshauer E, Kolorenč P and Pernpointner M 2015 Relativistic decay widths of autoionization processes: the relativistic fanoadc-stieltjes method *J. Chem. Phys.* **142** 144106
[41] Bondi A 1964 van der Waals volumes and radii *J. Phys. Chem.* **68** 441
[42] Fasshauer E 2013 HARDRoC, hunting asymptotic relativistic decay rates of clusters (http://www.pci.uni-heidelberg.de/tc/usr/elke/hardroc/html/main.html)
[43] Fasshauer E 2014 Investigation of relativistic effects in electronic decay processes in small and large noble gas clusters by ab initio and new simulation approaches *PhD thesis* University of Heidelberg
[44] Scheit S, Averbukh V, Meyer H-D, Zobeley J and Cederbaum L S 2006 Interatomic Coulombic decay in a heteroatomic rare gas cluster *J. Chem. Phys.* **124** 154305
[45] O'Keeffe P *et al* 2014 Experimental investigation of the interatomic Coulombic decay in NeAr dimers *Phys. Rev.* A **90** 042508
[46] Schnorr K *et al* 2013 Time-resolved measurement of interatomic Coulombic decay in Ne_2 *Phys. Rev. Lett.* **111** 093402
[47] Schnorr K *et al* 2015 Time-resolved study of ICD in Ne dimers using FEL radiation *J. Electron Spectrosc. Relat. Phenom.* **204** 245
[48] Barth S, Marburger S, Kugeler O, Ulrich V, Joshi S, Bradshaw A M and Hergenhahn U 2006 The efficiency of interatomic Coulombic decay in Ne clusters *Chem. Phys.* **329** 246

Multiconfigurational time-dependent Hartree method for fermions: Implementation, exactness, and few-fermion tunneling to open space

Elke Fasshauer*
Centre for Theoretical and Computational Chemistry, Department of Chemistry, University of Tromsø—The Arctic University of Norway, N-9037 Tromsø, Norway

Axel U. J. Lode†
Department of Physics, University of Basel, Klingelbergstrasse 82, CH-4056 Basel, Switzerland
(Received 10 October 2015; revised manuscript received 2 November 2015; published 21 March 2016)

We report on an implementation of the multiconfigurational time-dependent Hartree method (MCTDH) for spin-polarized fermions (MCTDHF). Our approach is based on a mapping for operators in Fock space that allows a compact and efficient application of the Hamiltonian and solution of the MCTDHF equations of motion. Our implementation extends, builds on, and exploits the recursive implementation of MCTDH for bosons (R-MCTDHB) package. Together with R-MCTDHB, the present implementation of MCTDHF forms the MCTDH-X package. We benchmark the accuracy of the algorithm with the harmonic interaction model and a time-dependent generalization thereof. These models consider parabolically trapped particles that interact through a harmonic interaction potential. We demonstrate that MCTDHF is capable of solving the time-dependent many-fermion Schrödinger equation to an arbitrary degree of precision and can hence yield *numerically exact* results even in the case of Hamiltonians with time-dependent one-body and two-body potentials. We study the problem of two initially parabolically confined and charged fermions tunneling through a barrier to open space. We demonstrate the validity of a model proposed previously for the many-body tunneling to open space of bosonic particles with contact interactions [Proc. Natl. Acad. Sci. USA **109**, 13521 (2012)]. The many-fermion tunneling can be built up from sequentially happening single-fermion tunneling processes. The characteristic momenta of these processes are determined by the chemical potentials of trapped subsystems of smaller particle numbers: The escaped fermions convert the different chemical potentials into kinetic energy. Using the two-body correlation function, we present a detailed picture of the sequentiality of the process and are able to tell tunneling from over-the-barrier escape.

DOI: 10.1103/PhysRevA.93.033635

I. INTRODUCTION

The time-dependent many-body Schrödinger equation for interacting fermions governs systems from many different fields ranging from electron dynamics in molecules [1] in quantum or theoretical chemistry, over graphene [2] and (fractional) quantum Hall states [3] in condensed matter, to the physics of quantum computation [4], quantum simulation [5], and quantum dots and mesoscopic structures and interactions thereof [6–8], to name but a few. A general approach to deal with the time-dependent many-body Schrödinger equation for interacting fermionic particles is hence of great and general interest, especially also in view of the recent experimental demonstration of deterministic production of few-fermion systems [9] and their detailed investigation [10–12] in the context of ultracold atoms.

However, the solution of Schrödinger's equation for many-body systems presents a formidable and in most cases not analytically tractable problem. The exceptions to this statement include the Lieb-Liniger [13] and Tonks-Girardeau [14] models for one-dimensional bosonic particles and the harmonic interaction model for fermionic or bosonic particles of any spatial dimension [15–17]. To date, unfortunately, no way has been found to scrutinize these or other analytical models to obtain solutions for the time-dependent Schrödinger equation for a general problem setting. Numerical methods that solve the Schrödinger equation are thus needed. Such numerical approaches also face limitations as the Hilbert space of many-body systems is growing exponentially with the particle number. Among the first approaches to the time-dependent many-body problem were so-called mean-field methods, which reduce the intractably large problem by transforming the time-dependent many-body Schrödinger equation (TDSE) to an effective one-body problem. This transformation can be done in different ways. One approach is to make a mean-field ansatz for the state of the system and to derive the equations of motion for it by employing a time-dependent variational principle [18,19]: Demanding the stationarity of the functional action with respect to small variations of the parameters of said mean-field ansatz and demanding the solution to obey constraints (like, for instance, normalization) yields the equations of motion for the parameters (the time-dependent orbital[s]) in the mean-field ansatz. In the case of distinguishable particles, one obtains the time-dependent Hartree-type or self-consistent field equations [18]. For indistinguishable bosons, these equations of motion are called time-dependent Gross-Pitaevskii equation [20,21] for a single-orbital ansatz and time-dependent multiorbital mean-field equations [22] for a multiorbital ansatz. For fermions they are named time-dependent Hartree(-Fock) equations [23]. All these equations have in common that they prescribe the time evolution of a single ([anti]symmetrized) product of

*elke.fasshauer@uit.no
†axel.lode@unibas.ch

one-particle states or, in short, of one configuration. They therefore cannot describe correlations between the particles and their dynamics adequately since that necessitates multiple configurations.

In order to straightforwardly go beyond the mean-field approach one allows not only one but all possible time-dependent configurations to contribute to the ansatz. One arrives, after a similar variational derivation as for the mean-field theories, at the multiconfigurational time-dependent Hartree approach (MCTDH) [24–26] for distinguishable particles, the MCTDH for bosons in the case of indistinguishable bosons [27,28] (for a dedicated version for the double-well special case, see Ref. [29], and for the multilayer MCTDH for bosons generalization, see Ref. [30]), or the MCTDH for fermions (MCTDHF) [31–36] in the case of indistinguishable fermions, which is also often referred to as multiconfigurational time-dependent Hartree-Fock. The generalization to multiconfigurational ansätze and hence improved accuracy comes at a price: The number of (symmetrized) basis states increases exponentially with the number of particles considered. The improvement in accuracy, however, can be crucial in order to describe the ongoing quantum dynamics, since it incorporates the evolution of correlations between the particles or degrees of freedom in the system. Moreover, the ansatzes of MCTDH, MCTDH for bosons, and MCTDHF form a formally complete set of the respective many-body Hilbert spaces. Therefore, these methods can in principle provide the *exact* solution of the full TDSE when a convergence with respect to the number of variational parameters in the description is achieved. This has been demonstrated for the bosonic case in Refs. [37–39] and the fermionic case in, for instance, Ref. [36].

Herein, we report on the implementation of MCTDHF that relies on the equivalence of many-body Hamiltonians in Fock space to a mapping [40] that helps us to optimally scrutinize the sparsity of the Hamiltonian in configuration space.

We demonstrate how the algorithm converges to the exact solutions of the TDSE for the case of spin-polarized fermions even for Hamiltonians with time-dependent one- and two-body potentials. We show the convergence and exactness of the algorithm, we test it with the exactly solvable harmonic interaction model (HIM) and its time-dependent generalization (TDHIM) [37,38]. Thereby, we demonstrate MCTDHFs capability to describe both ground states as well as many-body dynamics with a time-dependent Hamiltonian, including time-dependent one-body potentials and interactions, accurately.

We investigate charged fermions tunneling to open space from an initial parabolic confinement similar to recent experimental realizations [9,10]. We thereby verify a model for the many-boson tunneling to open space [41] to also hold in the fermionic case. We prepare a system of $N = 2$ charged, spin-polarized fermions in the ground state of a parabolic trap. By subsequently transforming the potential to an open configuration with a barrier, we allow the fermions to escape to open space by tunneling. We monitor the process with the time evolution of the momentum distributions and the one-body and two-body correlation functions.

We implemented the solution of MCTDHF equations of motion extending and exploiting our previous recursive implementation of the MCTDH for bosons, the R-MCTDHB package [42]. The resulting software is now capable of solving the time-dependent many-body Schrödinger equation for general indistinguishable particles. We name the resulting software MCTDH-X, since it computes the dynamics of multi-configurational wave functions of $X = \mathrm{F}$ fermions and $X = \mathrm{B}$ bosons. The MCTDH-X software is distributed under a copy-left license through the website [43] and provides numerically exact results for bosons—as shown in Refs. [37,38]—and—as shown below—numerically exact results for fermions.

Let us mention here that the present study considers long-range interactions in partially large grids. The evaluation of the respective two-body operators relies crucially on the so-called interaction-matrix evaluation via successive transforms algorithm introduced in Refs. [38,39]. Without this algorithm the present and many recent investigations of realistic solutions of the TDSE as, for instance, in Refs. [37,38,44–46] would have been impossible.

The structure of this paper is as follows: In Sec. II, we introduce the TDSE, derive the MCTDHF equations of motion, describe our implementation of it, and show its accuracy. Section III discusses charged fermion tunneling to open space dynamics and Sec. IV gives conclusions and an outlook.

II. THEORY, IMPLEMENTATION, AND EXACTNESS

A. Time-dependent Schrödinger equation and Hamiltonian

The problem we aim to solve with the MCTDHF is the time-dependent Schrödinger equation for N spin-polarized interacting fermionic particles. The TDSE reads

$$i\,\partial_t|\Psi\rangle = \hat{H}|\Psi\rangle. \tag{1}$$

Here, the wave function $|\Psi\rangle$ and the Hamiltonian $\hat{H}$ depend on all the particle coordinates $\vec{r}_1,\ldots,\vec{r}_N$ and time t. We investigate systems with at most two-body operators in the Hamiltonian:

$$\hat{H} = \sum_k \hat{h}(\vec{r}_k;t) + \sum_{j<k} \hat{W}(\vec{r}_j,\vec{r}_k,t). \tag{2}$$

Here, $\hat{h}(\vec{r}) = \frac{1}{2}\partial_{\vec{r}}^2 + V(\vec{r},t)$, is the one-body Hamiltonian and $\hat{W}(\vec{r},\vec{r}',t)$ represents the two-body interactions. Both terms are generally time-dependent. In this work, we employ dimensionless units throughout: The dimensionless Hamiltonian, Eq. (2), is obtained by dividing the dimension-full Hamiltonian by $\frac{\hbar^2}{mL^2}$ (m is the mass of the considered Fermions and L is a conveniently chosen length scale).

In second quantization, one uses field operators to represent the many-body problem:

$$\hat{\Psi}(\vec{r},t) = \sum_k \hat{a}_k(t)\phi_k(\vec{r};t). \tag{3}$$

The functions $\phi_k(\vec{r},t)$ are an orthonormal set of time-dependent single-particle states or orbitals that build up a fully antisymmetrized basis of the N-fermion Hilbert space. Consequently, the Hamiltonian of Eq. (2) reads

$$\hat{H} = \sum_{kq} h_{kq}(t)\hat{a}_k^\dagger\hat{a}_q + \frac{1}{2}\sum_{ksql} W_{ksql}(t)\hat{a}_k^\dagger\hat{a}_s^\dagger\hat{a}_l\hat{a}_q. \tag{4}$$

Here, we used the following notations for the one-body and two-body matrix elements h_{kq} and W_{ksql}, respectively:

$$h_{kq}(t) = \int d\vec{r}\,\phi_k^*(\vec{r},t)\hat{h}(\vec{r},t)\phi_q(\vec{r},t),$$
$$W_{ksql}(t) = \iint d\vec{r}'d\vec{r}\,\phi_k^*(\vec{r}',t)\phi_s^*(\vec{r},t)\hat{W}(\vec{r}',\vec{r},t)\phi_q(\vec{r},t)\phi_l(\vec{r}',t). \tag{5}$$

In the following we will make use of the matrix elements of the reduced one- and two-body density matrices,

$$\rho_{kq}(t) = \langle\Psi|\hat{a}_k^\dagger\hat{a}_q|\Psi\rangle, \qquad \rho_{kslq}(t) = \langle\Psi|\hat{a}_k^\dagger\hat{a}_s^\dagger\hat{a}_l\hat{a}_q|\Psi\rangle, \tag{6}$$

respectively, as well as the reduced one-body and two-body densities [47,48]

$$\rho^{(1)}(\vec{r},\vec{r}',t) = \sum_{kq}\rho_{kq}\phi_k^*(\vec{r}',t)\phi_q(\vec{r},t), \text{ and}$$
$$\rho^{(2)}(\vec{r}_1,\vec{r}_2,\vec{r}_1',\vec{r}_2',t) = \sum_{kslq}\rho_{kslq}\phi_k^*(\vec{r}_1',t)\phi_s^*(\vec{r}_1,t)\phi_l(\vec{r}_2',t)\phi_q(\vec{r}_2,t), \tag{7}$$

respectively. Now, all prerequisites for the derivation of the MCTDHF equations of motion are defined and we can proceed by doing so.

B. MCTDHF equations of motion

To derive the equations of motion of MCTDHF, we first formulate a general multiconfigurational ansatz for the wave function. Then, we use the time-dependent variational principle [19] to minimize the error in describing the solution of the TDSE with said ansatz. The ansatz is obtained by truncating the field operator in Eq. (3) from an infinite to a finite sum of M operators $\{\hat{a}_k(t)\}_{k=1}^M$. Consequently, some expressions in Sec. II A become finite sums [cf. Eqs. (3), (4), and (8)] or have a finite set of indices [cf. Eqs. (5) and (6)].

The wave function corresponding to a field operator in a finite set of M time-dependent orbitals [see Eq. (3)] is the ansatz for MCTDHF and reads

$$|\Psi\rangle = \sum_{\vec{n}} C_{\vec{n}}(t)|\vec{n};t\rangle = \sum_{\vec{n}} C_{\vec{n}}(t)\prod_{i=1}^{M}(\hat{a}_k^\dagger(t))^{n_k}|\text{vac}\rangle. \tag{8}$$

Here, a vector notation $\vec{n} = (n_1,\ldots,n_M)$ for the occupation numbers was invoked. In total, this ansatz contains $N_{\text{conf}} = \binom{M}{N}$ terms and as many time-dependent coefficients $C_{\vec{n}}(t)$. The occupation number states or configurations $\{|\vec{n};t\rangle\}$ are fully antisymmetrized products of the orbitals $\{\phi_k(\vec{r};t)\}_{k=1}^M$. The N_{conf} coefficients and M orbitals are the variational parameters in the derivation of the MCTDHF equations of motion. The functional action of the TDSE [Eq. (1)] reads as follows [19]:

$$\mathcal{S} = \int dt\left(\langle\Psi|\hat{H} - i\partial_t|\Psi\rangle + \sum_{ij}\mu_{ij}(t)(\langle\phi_i|\phi_j\rangle - \delta_{ij})\right). \tag{9}$$

Here, the orthonormality of the orbitals $\{\phi_k(x;t)\}_{k=1}^M$ is ensured by the Lagrange multipliers $\mu_{ij}(t)$ in $\mathcal{S}$. From demanding the stationarity of this functional action with respect to variations of the coefficients $C_{\vec{n}}(t)$ and the orbitals $\{\phi_k(\vec{r},t)\}_{k=1}^M$,

$$\partial_{C_{\vec{n}}^*(t)}\mathcal{S}\left[\{C_{\vec{n}}(t)\},\{\phi_k(\vec{r},t)\}_{k=1}^M\right] \overset{!}{=} 0 \;\; \forall\,\vec{n};$$
$$\partial_{\phi_k^*(\vec{r},t)}\mathcal{S}\left[\{C_{\vec{n}}(t)\},\{\phi_k(\vec{r},t)\}_{k=1}^M\right] \overset{!}{=} 0 \;\; \forall\,k, \tag{10}$$

the equations of motion for the orbitals and the coefficients of the MCTDHF are obtained. To simplify the resulting equations of motion and without loss of generality we use an invariance property of the ansatz [Eq. (8)] (see Refs. [24,26]) and set $\langle\phi_k|i\partial_t|\phi_q\rangle = 0$. For details of the derivation, see, for instance, Refs. [34–36]. The obtained coefficients' equations of motion read

$$\mathcal{H}(t)\mathcal{C}(t) = i\partial_t\mathcal{C}(t); \quad \mathcal{H}_{\vec{m}\vec{m}'}(t) = \langle\vec{m};t|\hat{H}|\vec{m}';t\rangle. \tag{11}$$

Here, $\mathcal{C}(t)$ collects all coefficients $C_{\vec{n}}(t)$ in a vector. The indexing of this vector is a key part of the implementation of MCTDHF and is described in the following subsection. The orbitals' equations of motion read

$$i\partial_t\phi_j(\vec{r},t) = \hat{\mathbf{P}}\left(\hat{h}\phi_j(\vec{r},t) + \sum_{k,s,q,l=1}^{M}\{\rho(t)\}_{jk}^{-1}\rho_{kslq}(t)\hat{W}_{sl}(\vec{r},t)\phi_q(\vec{r},t)\right),$$
$$\hat{\mathbf{P}} = \mathbf{1} - \sum_{j'=1}^{M}|\phi_{j'}\rangle\langle\phi_{j'}|. \tag{12}$$

The projector $\hat{\mathbf{P}}$ emerges in the derivation from the Lagrange multipliers introduced in the functional action, Eq. (9), to ensure the orthonormality of the orbitals. The local time-dependent potentials $\hat{W}_{sl}(\vec{r};t) = \int d\vec{r}'\phi_s^*(\vec{r}',t)\hat{W}(\vec{r},\vec{r}',t)\phi_l(\vec{r}',t)$ were defined. Equations (11) and (12) form the core of the MCTDHF. The number of coefficients' equations [Eq. (11)] is $\binom{M}{N}$ and the number orbitals' equations [Eq. (12)] is M. In the latter equation (12), the main computational effort is to compute $\mathcal{O}(M^4)$ two-body terms (containing ρ_{kslq}). With this scaling of the problem size, $\mathcal{O}(10)$ fermions are tractable at present without further optimization of the MCTDH-X software. We note that the equations of motion, (11) and (12), are of the same shape as the orbital equations of motion in the case of bosons [34]. The coefficients' and orbitals' equations form a coupled, integro-differential, and generally nonlinear set: The evaluation of Eq. (11) for the coefficients $C_{\vec{n}}(t)$ necessitates the matrix elements $W_{ksql}(t)$ and $h_{kq}(t)$ [Eq. (5)] computed from the current set of orbitals $\{\phi_k(\vec{r},t)\}_{k=1}^M$. The propagation of Eq. (12) for the orbitals $\{\phi_k(\vec{r},t)\}_{k=1}^M$ necessitates the matrix elements $\rho_{kq}(t)$ and $\rho_{kslq}(t)$ [Eq. (6)] computed from the present set of coefficients $C_{\vec{n}}(t)$. We move on and describe our implementation of MCTDHF.

C. Hamiltonian as a mapping in configuration space

Our MCTDHF implementation relies on a mapping for operators in Fock space as described in Ref. [40] and takes maximal advantage of the sparsity of the Hamiltonian in Fock

basis [Eq. (11)]. We use the address

$$I(h_1,\ldots,h_{k_\mu}) = 1 + \sum_{j=1}^{k_\mu} \binom{N + k_\mu - h_j}{k_\mu + 1 - j} \tag{13}$$

to index all occupation number states of N fermions in M orbitals. Here k_μ is the number of holes, i.e., 0 occupation numbers in the configuration $\vec{n}$, and h_j are the positions of these holes. Importantly, the indexing defined by Eq. (13) allows us to write the coefficients $C_{\vec{n}}(t)$ in a compact vector notation $\mathcal{C}(t)$ as done in the MCTDHF coefficients equation of motion, Eq. (11), above. We continue by illustrating how a general set of operators' actions can be cast in a compact and intuitive form by scrutinizing the indexing in Eq. (13). The action of any of the operators that appear in the Hamiltonian Eq. (4) applied to a given configuration $|\vec{n}_1;t\rangle$ will yield a modified configuration $\alpha|\vec{n}_2;t\rangle$. Evidently, α depends on the occupation numbers $\vec{n}_1$ and on the applied creation and annihilation operators. Since all the configurations have an index assigned through Eq. (13), it is sufficient to know three numbers to apply *any* operator: (i) the index I_1 of $|\vec{n}_1;t\rangle$, (ii) the index I_2 of $|\vec{n}_2;t\rangle$, and (iii) the prefactor α. Let us consider the generic one-body operators $\hat{a}_4^\dagger\hat{a}_1$ and $\hat{a}_6^\dagger\hat{a}_3$ and the configuration $|\vec{n}_1;t\rangle = |1,1,1,0,1,0,0,1,0\rangle$ as an example. One finds

$$\hat{a}_4^\dagger\hat{a}_1|1,1,1,0,1,0,0,1,0\rangle = |0,1,1,1,1,0,0,1,0\rangle;$$

and $$\hat{a}_6^\dagger\hat{a}_3|1,1,1,0,1,0,0,1,0\rangle = (-1)|1,1,0,0,1,1,0,1,0\rangle.$$

In our example, we have $N = 5, M = 9$ and the number of holes is $k_\mu = 4$. Consequently, for $\hat{a}_4^\dagger\hat{a}_1$ with $I_1 = I(4,6,7,9) = 8$, we find $I_2 = I(1,6,7,9) = 73$ and $\alpha = 1$ from Eq. (13). For $\hat{a}_6^\dagger\hat{a}_3$ with $I_1 = 8$, we find $I_2 = I(3,4,7,9) = 26$ and $\alpha = (-1)$. For many operators' actions on a configuration one finds that the respective prefactor α is zero and one does therefore not have to consider the action of the operator on that configuration. In order to minimize the effort in the evaluation of the MCTDHF coefficients equations of motion (11), we therefore only save the triples I_1, I_2, α when $\alpha \neq 0$ in a dedicated custom data type in our implementation of Eq. (11). The data type is constructed with the following recipe: For every one- or two-body operator in the Hamiltonian (4), we analyze for every I_1 if α is zero. If so, we move on to the next configuration. Only if α is nonzero, I_1, I_2, and α are stored. The resulting set of triplets (I_1, I_2, α) for every operator in the Hamiltonian (4), for all configurations $|\vec{n}_1;t\rangle$, constitutes the most compact (and hence memory-efficient) way of applying the Hamiltonian to a given vector $\mathcal{C}(t)$ of coefficients. This allows for a faster evaluation of the coefficients equation of motion and for the handling of configuration spaces with a larger number of coefficients.

D. Benchmark with the time-dependent harmonic interaction model

The HIM and TDHIM are models that are exactly solvable when a coordinate transform from Cartesian to center-of-mass and relative coordinates is applied to their Hamiltonians. Solutions are known for any spatial dimension and for bosonic and fermionic systems [15]. The existence of exact solutions distinguishes the HIM models from other example problems such as, for instance, the helium atom (cf. Ref. [36]), for which approximate solutions with a very high accuracy are available—but not exact ones.

Since the HIM and TDHIM Hamiltonians present a correlated many-body problem in Cartesian coordinates, these models are a good test for the accuracy of the MCTDHF algorithm which, of course, also works in Cartesian coordinates. Benchmarks have been performed previously in the case of the MCTDH for bosons with the HIM and its time-dependent generalization, the TDHIM in Refs. [37,38]. Let us mention here that the TDHIM presents a much tougher problem for the algorithm than typical physical problems like the tunneling to open space discussed in Sec. III because the TDHIM Hamiltonian has time-dependent one- and two-body terms. In a study of the eigenstates of the HIM, we found that MCTDHF yields results with an arbitrarily large accuracy, see Supplemental Material [49].

In this section, we asses the correctness of our implementation and the formal exactness of MCTDHF with the fermionic versions of the TDHIM.

To arrive at a time-dependent generalization of the HIM, the TDHIM, we chose a Hamiltonian with time-dependent trapping frequency $\omega \equiv \omega_{\mathrm{TD}}(t)$ and time-dependent interparticle interaction $K \equiv K_{\mathrm{TD}}(t)$. The obtained TDHIM Hamiltonian $\hat{H}'$ reads [37,38]

$$\hat{H}'(t) = \sum_{i=1}^{N}\left[-\frac{1}{2}\partial_{\vec{r}}^2 + \frac{1}{2}\omega_{\mathrm{TD}}(t)^2\vec{r}^2\right] + K_{\mathrm{TD}}(t)\sum_{i<j}^{j=N}(\vec{r}_i - \vec{r}_j)^2. \tag{14}$$

We now adopt the strategy in the Refs. [37,38] and set

$$\omega_{\mathrm{TD}}(t) = \omega[1 + f(t)]; \quad K_{\mathrm{TD}}(t) = K\left[1 - \frac{\omega_0^2}{2NK}f(t)\right]. \tag{15}$$

With this choice, we apply the coordinate transformations to relative $\vec{x}_j = \frac{1}{\sqrt{j(j+1)}}\sum_{i=1}^{j}(\vec{r}_{j+1} - \vec{r}_i)$, $\quad j = 1,\ldots,N-1$ and center-of-mass coordinates $\vec{x}_N = \sum_{i=1}^{N}\vec{r}_i$. We obtain

$$\hat{H}'_{\mathrm{rel}} = \sum_{i=1}^{N-1}\left(-\frac{1}{2}\partial_{\vec{x}_i}^2 + \frac{1}{2}\delta_N^2\vec{x}_i^2\right); \quad \delta_N = \sqrt{\omega^2 + 2NK}. \tag{16}$$

$$\hat{H}'_{\mathrm{CM}}(t) = -\frac{1}{2}\partial_{\vec{x}_N}^2 + \frac{1}{2}\omega(t)^2\vec{x}_N^2. \tag{17}$$

It is important to note that due to our choice of $\omega(t)$ and $K(t)$, the Hamiltonian of the relative problem is time-independent and identical to the one obtained for the HIM, i.e., when setting $f(t) \equiv 0$ in Eqs. (14) and (15); see also Ref. [49]. Moreover, the Hamiltonian of the center-of-mass problem $\hat{H}'_{\mathrm{CM}}(t)$ defines the following time-dependent, but *one-body* problem that can be easily solved numerically exactly [50]:

$$i\partial_t|\Psi_{\mathrm{CM}}(t)\rangle = \hat{H}'_{\mathrm{CM}}(t)|\Psi_{\mathrm{CM}}(t)\rangle. \tag{18}$$

The obtained time-dependent energy reads

$$\begin{aligned} E_{\mathrm{TDHIM}}(t) &= \epsilon_{\mathrm{rel}} + \epsilon'_{\mathrm{CM}}(t), \\ \epsilon'_{\mathrm{CM}}(t) &= \langle\Psi|\hat{H}'_{\mathrm{CM}}|\Psi\rangle. \end{aligned} \tag{19}$$

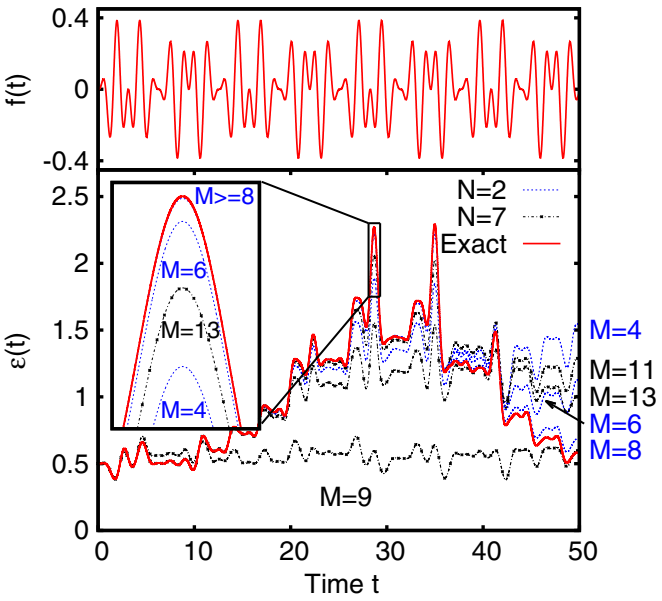

FIG. 1. Convergence of the MCTDHF for the TDHIM model for $N = 2$ and $N = 7$. The upper panel shows the time-dependent parameter $f(t)$ modulating both interactions and the frequency of the parabolical trap [cf. Eqs. (14) and (15)]. The lower panel depicts the computed results for the time-dependent energy $\epsilon'_{\mathrm{CM}}(t)$ for the exact solution (solid red line) and MCTDHF(M) for increasing numbers of orbitals M for two (blue dashed lines) and seven fermions (black dashed-dotted line with points). Fast convergence of the MCTDHF(M) predictions for $\epsilon'_{\mathrm{CM}}(t)$ to the exact value is observed for the present case of almost erratically time-dependent one- and two-body parts in the Hamiltonian when M is increased. We find that the MCTDHF prediction for $\epsilon'_{\mathrm{CM}}(t)$ is indistinguishable from the exact energy for $M = 10$ in the case of $N = 2$ and for $M = 15$ for the case of $N = 7$. All quantities shown are dimensionless.

Since our choice for $K(t)$ and $\omega_{\mathrm{TD}}(t)$ keeps $\delta_N = \sqrt{\omega^2 + 2NK}$ time-independent and identical to the δ_N in the case of the time-independent HIM Hamiltonian, $\epsilon_{\mathrm{rel}} = D\sum_{i=1}^{N-1}[\frac{2i+1}{2}\delta_N]$ remains also unchanged and time-independent (see Ref. [49]). For computational convenience, we use the same parameters as in Refs. [37,38], $K_0 = 0.5$ and $\omega = 1$ with $f(t) = \sin(t)\cos(2t)\sin(0.5t)\sin(2t)$. We plot the exact solution for $\epsilon'_{\mathrm{CM}}(t)$ in Fig. 1 together with the MCTDHF predictions for $N = 2$ and $N = 7$ fermions for various numbers of orbitals M.

We find that the MCTDHF(M) prediction converges to the exact result $\epsilon'_{\mathrm{CM}}(t)$ rapidly for increasing M. This is analogous to the convergence of MCTDH for bosons for the TDHIM model as shown in Refs. [37,38]. We note here that in the cases where the energies obtained from MCTDHF(M) are identical to the exact one, a further increase of M does not change the predictions of the method anymore: The wave function's time evolution converges and represents a *numerically exact* solution to the time-dependent Schrödinger equation. Importantly, the occupations of the least occupied orbitals remain negligibly small in the case of a converged solution of the TDSE with MCTDHF(M). This renders a practical criterion for the convergence and numerical exactness of MCTDHF(M) for any given application.

III. TUNNELING TO OPEN SPACE OF FEW-FERMION SYSTEMS

There is outstanding experimental progress in the deterministic production of few-fermion systems [9] and detailed investigations on their properties [10–12]. Of particular interest is here that these experiments with few-fermion systems consider situations where one or several of the particles are escaping from an initial confinement to open space. The theoretical work entailing the above experiments deals mostly with the issue of the decay rates with respect to the possible different decay channels for fermions with internal structure; see, for instance, Refs. [51,52]. The correlation functions and their evolution have, however, not been systematically investigated yet. This motivates us to apply MCTDHF to the problem of initially parabolically confined fermions that are allowed to tunnel through a potential barrier to open space. We stress here that our simulations below consider a system with a similar one-body potential as the few-fermion systems in the experiments of the Heidelberg group [9,10], but both the two-body potential and the constituents of the system differ from the experimental realization: In our simulations Coulomb and not contact interactions are considered and the constituents we consider are spin-polarized fermions and not fermions with an internal degree of freedom. We adopt our scheme to model the process from previous work on bosons tunneling to open space [38,41,53]: The system is initialized in the interacting ground state of a parabolic potential (time $t < 0$). Subsequently, at time $t \geqslant 0$, the potential is transformed to an open form with a barrier that allows for the system to tunnel to open space. For the sake of simplicity and convenience of computations, we use the same potential $V(\vec{r},t)$ without a threshold as Refs. [38,41,53]. See Fig. 2(a) for a plot. As interparticle interaction $\hat{W}(\vec{r},\vec{r}')$ we use the regularized Coulomb interaction from Ref. [8],

$$\hat{W}(\vec{r},\vec{r}') = \frac{\lambda_0}{\sqrt{|\vec{r}-\vec{r}'|^2 + \alpha^2 e^{-\beta|\vec{r}-\vec{r}'|}}}, \tag{20}$$

where we set $\alpha = 0.1$ and $\beta = 100$, also as in Ref. [8].

Since the following considerations are for one spatial dimension, we are going to use the labels x and k synonymously for the vectors $\vec{r}$ and $\vec{k}$, respectively. We restrict the present study to the case of $N = 2$ fermions because the potential $V(x,t > 0)$'s barrier [cf. Fig. 2(a)] is too small for larger particle numbers to still speak of a tunneling process: For the case of $N = 3$ the energy per particle is comparable to the height of the barrier. Let us emphasize that we checked the results in the following for their convergence with respect to the number of orbitals M in our computations and found that $M = 6$ orbitals yield an essentially exact description.

In the following, we study the dynamics for $N = 2$ fermions for the case $\lambda_0 = 1.0$ and $\lambda_0 = 0.5$ and investigate if the model for the many-boson tunneling process in Ref. [41,54] is predictive also for fermions. This model decomposes the one-dimensional Hilbert space into "IN" and "OUT" regions and considers single-particle ejection processes from the viewpoint of energies. When a particle is ejected from IN to OUT, the subsystem which is left behind remains with an energy $E_{IN}(N-1) = E_{IN}(N) - \mu_1$. Here, μ_1 is the first chemical potential [see Fig. 2(b)], $E_{IN}(N)$ is the numerical result of the two-fermion system, and $E_{IN}(N-1)$ is the analytical result

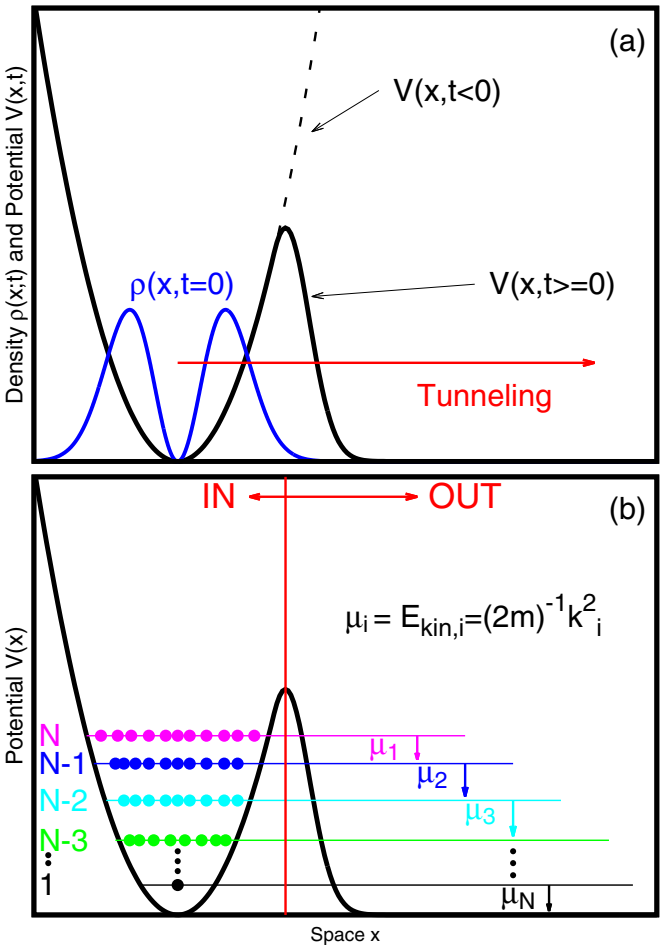

FIG. 2. Scheme and model for the fermion tunneling to open space process. (a) The setup used to study how initially parabolically confined (black dashed line) fermions tunnel to open space when the potential is transformed to its open form (solid black line). For reference, an initial density is sketched (blue line). After the transformation of the potential, the system becomes unbound and tunnels through the barrier to open space. (b) Model for the tunneling process. The one-dimensional Hilbert space is split into IN and OUT regions at the maximum of the barrier (vertical red line). The many-fermion process can be built up from concurrently happening single-fermion tunneling processes: Each fermion escapes into OUT with a characteristic momentum. This characteristic momentum is in turn defined by the chemical potentials μ_i of the harmonically trapped, interacting system in the IN region before the ejection. Neglecting interactions in the OUT region, one obtains momenta $k_i = \sqrt{2m\mu_i}$. (The figure is adapted from Refs. [38,41], and all quantities shown are in dimensionless units.)

for the single-fermion ground state of the harmonic oscillator, $E_{IN}(1) = 0.5$, since N is 2. The emitted particle in the OUT region has the energy μ_1 at its disposal, which it converts to kinetic energy. Since the potential $V(x,t > 0)$ is zero in almost all of the OUT region, the emitted particle can approximately be considered as free and its kinetic energy is therefore given by $\mu_1 = \frac{k_1^2}{2m}$. Consequently, a characteristic momentum $k_1 = \sqrt{2m\mu_1}$ will manifest in the momentum distribution $\rho(k,t) = \sum_{jq} \rho_{jq} \tilde{\phi}_j^*(k;t)\tilde{\phi}_q(k;t)$. Here, $\tilde{\phi}_q(k;t)$ denotes the Fourier transform of the orbital $\phi_q(x;t)$. The second emitted particle has the second chemical potential $\mu_2 = E_{IN}(N-1) - E_{IN}(N-2)$, with $E_{IN}(N-2) = 0$, to convert it to kinetic energy upon its ejection. This results in a second characteristic momentum $k_2 = \sqrt{2m\mu_2}$ in the momentum distribution $\rho(k,t)$. By continuously applying this idea, the N-body tunneling process can be reconstructed by concurrently happening single-particle tunneling processes; cf. Fig. 2(b).

The momenta obtained from the model for the $N = 2$ and $\lambda_0 = 1.0$ case are $k_1 = 2.103$ and $k_2 = 1.0$. For the $N = 2$, $\lambda_0 = 0.5$ case, we find $k_1 = 1.931$ and $k_2 = 1.0$. We plot the exact time evolution of the momentum density $\rho(k,t)$ in Fig. 3. We find that the model for the tunneling process—albeit originally devised for bosonic particles with a contact interparticle interaction potential—predicts the momenta of the fermions with Coulomb interactions emitted to open space with a remarkable degree of accuracy; see Figs. 3(b) and 3(c). Upon closer inspection of Fig. 3(b), we find a peak structure in the momentum distribution in between $k_1 = 2.103$ and $k_2 = 1.0$. This structure corresponds to a correlated pair ejection (see correlation functions $g^{(1)}$ and $g^{(2)}$ below) as the energy of the whole system $E_{IN}(N = 2) = 2.712$ is sufficiently over the height of the barrier (2.226) for $\lambda_0 = 1.0$. Furthermore, one gets a good estimate of the momentum of the process, k_{red}, with the assumption that a particle with energy $\mu_1 + \mu_2 = E_{IN}(N = 2)$ and the reduced mass $\kappa = \frac{1}{2}$ was ejected:

$$k_{\mathrm{red}} = \sqrt{2\kappa E_{IN}(N = 2)}.$$

One finds $k_{\mathrm{red}} = 1.613$ for $\lambda_0 = 1$ and $k_{\mathrm{red}} = 1.538$ for $\lambda_0 = 0.5$. Since there is no clear feature around k_{red} in the momentum distribution $\rho(k,t)$ in Fig. 3(c) for the case of $\lambda_0 = 0.5$, we infer that in that case the total energy of the system is not sufficiently over the barrier for the correlated two-body ejection to happen. Let us remark here that this is an interesting difference to the tunneling dynamics of the bosonic systems investigated in Refs. [38,41,54]. We leave it as subject of further investigations to determine if and how the emergence of k_{red} in the momentum distribution is modified for a larger number of fermions or bosons with the same Coulomb interactions as in the present study. We infer from the remarkable agreement of the predicted momenta and the momentum peaks in $\rho(k,t)$ in Fig. 3 that the bulk of the many-fermion tunneling to open space process is—like its many-boson counterpart—built up by single-particle processes with characteristic momenta $k_1, k_2, \ldots$ determined by chemical potentials $\mu_1, \mu_2, \ldots$ of trapped subsystems of decreasing particle number $N, N-1, \ldots$.

We move on to investigate the dynamics of the one-body correlation functions in momentum space $|g^{(1)}(k,k';t)|^2$ and in real space, $|g^{(1)}(x,x';t)|^2$. The definition of $g^{(1)}$ is [47]

$$g^{(1)}(\xi,\xi',t) = \frac{\rho^{(1)}(\xi,\xi',t)}{\sqrt{\rho^{(1)}(\xi,\xi,t)\rho^{(1)}(\xi',\xi',t)}},$$

where $\xi = k$ for the momentum space correlation function and $\xi = x$ for the real-space correlation function. The reduced one-body densities in momentum space, $\rho^{(1)}(k,k',t)$, are obtained from Eq. (8) by applying a Fourier transform to the orbitals. In the case of uncorrelated particles characterized by the momenta k and k' or coordinates x and x', the correlation function is 1, while it is 0 for correlated particles. Its pattern allows us to analyze whether the particles tunnel sequentially or not (see in this context also the two-body correlation $g^{(2)}$

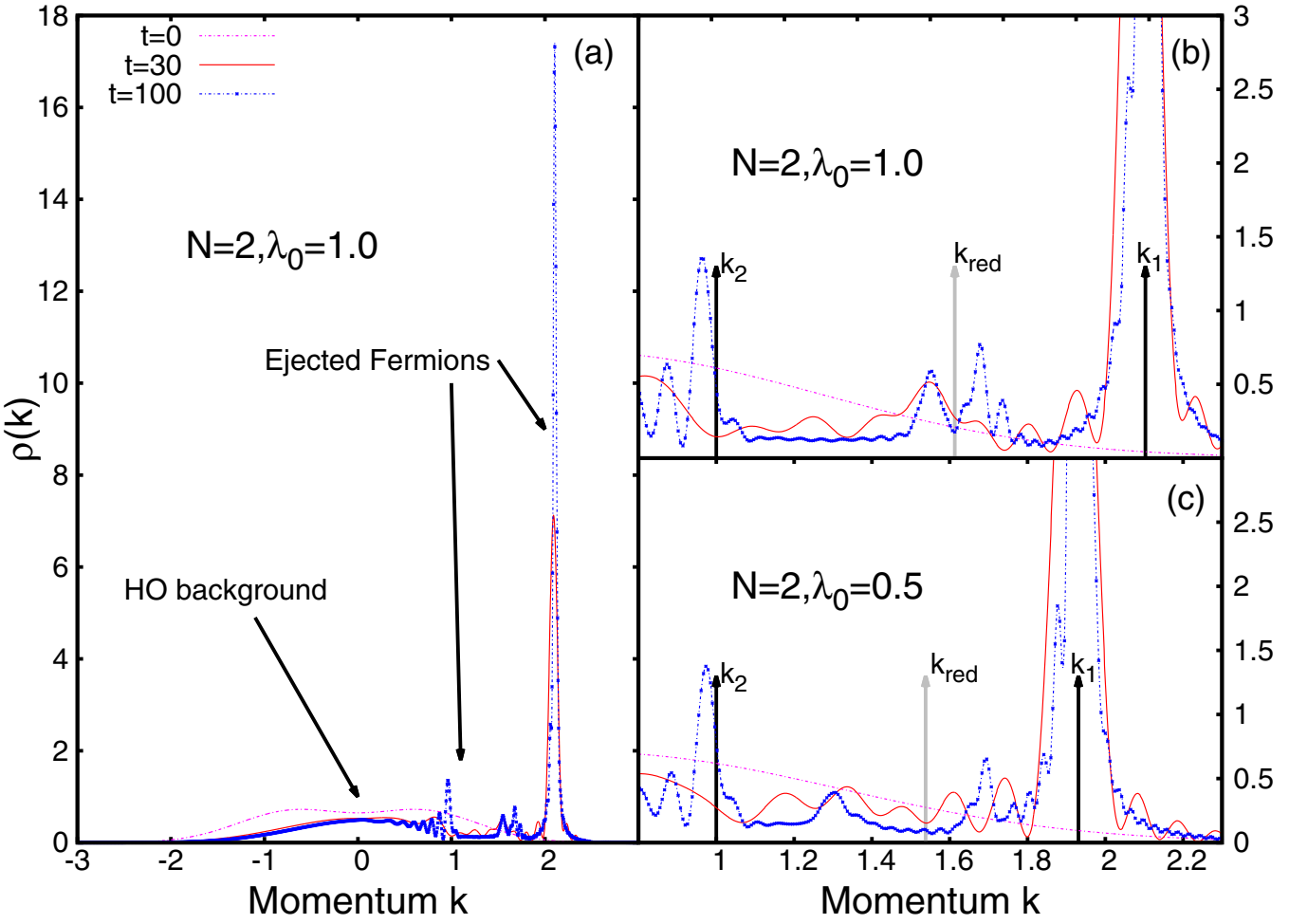

FIG. 3. Comparison of characteristic momenta of two-fermion tunneling to open space to model predictions. Panel (a) shows the overall momentum distributions $\rho(k)$ at times $t = 0,30,100$ in the time evolution of the tunneling process for $N = 2$ and $\lambda_0 = 1.0$. Centered around $k = 0$, the momentum distributions have a broad feature corresponding to the trapped fraction of the system (cf. harmonic oscillator [HO] background label). The particles that escape to open space correspond to the peaks which emerge in the momentum distributions with time. These peaks' momentum distributions are enlarged for $\lambda_0 = 1.0$ in panel (b) and for $\lambda_0 = 0.5$ in panel (c). According to the model in Fig. 2(b), the characteristic fermion ejection momenta are defined by the chemical potentials μ_i of the harmonically trapped, interacting system. The obtained momenta $k_i = \sqrt{2m\mu_i}$ are shown as black arrows in panels (b) and (c). The position of the main peaks agrees very well with the prediction of the model, k_1,k_2. The additional structure in the case of the stronger interactions in panel (b) can be attributed to a correlated two-body escape process (see text for further discussion). The momentum associated with this process is $k_{\rm red} = \sqrt{2\kappa(\mu_1 + \mu_2)} = 1.613$, where $\kappa = \frac{1}{2}$ is the reduced mass of the two-fermion system [see gray arrow in panel (b)]. For the weaker interactions $\lambda_0 = 0.5$ in panel (c), the two-fermion tunneling or escape seems to be less favorable, since no clear features are seen at the respective momentum $k_{\rm red} = 1.538$. All quantities shown are dimensionless. See text for further discussion.

below). From the value of the correlation function $g^{(1)}$, it can further be inferred whether certain points in space (x,x') or combinations of momenta (k,k') correspond to the same ($|g^{(1)}| = 1$) or to different ($|g^{(1)}| = 0$) orbitals.

As a first observation (left column of Fig. 4), we find that the correlation of the initial state of the fermionic systems is much stronger than in the bosonic counterpart investigated in Refs. [38,41], which is essentially uncorrelated, i.e., $|g^{(1)}|^2 \approx 1$. Throughout the tunneling process, we find an emergence of a line structure of correlations in $|g^{(1)}(k,k';t)|^2$ around the momenta k_1,k_2 at which particles are ejected from the well to open space; see top right panel of Fig. 4. We deduce from this line structure that the tunneling process can be controlled by adjusting the potential in the outer region in analogy to the bosonic tunneling to open space process [41,54]. Upon detailed comparison of the emergent line structure with respect to the bosonic case [41] in which the lines are simply marked by $|g^{(1)}| \to 0$, the following interesting difference is found: At the second momentum k_2 one actually finds $|g^{(1)}(k_2,k)| \approx 1$ which is enclosed by lines at a small distance ι with $|g^{(1)}(k_2 \pm \iota,k)| < 1$ (cf. black arrows and their vicinity in top right panel of Fig. 4). The different correlation properties of k_1 and k_2 hint that the fermions traveling at these velocities are sitting in different orbitals. This indicates that the two fermions escape sequentially. For an investigation of the reasons for this difference to the case of the bosonic tunneling to open space, where the single-particle processes happen concurrently, see the discussion of the two-body correlations below.

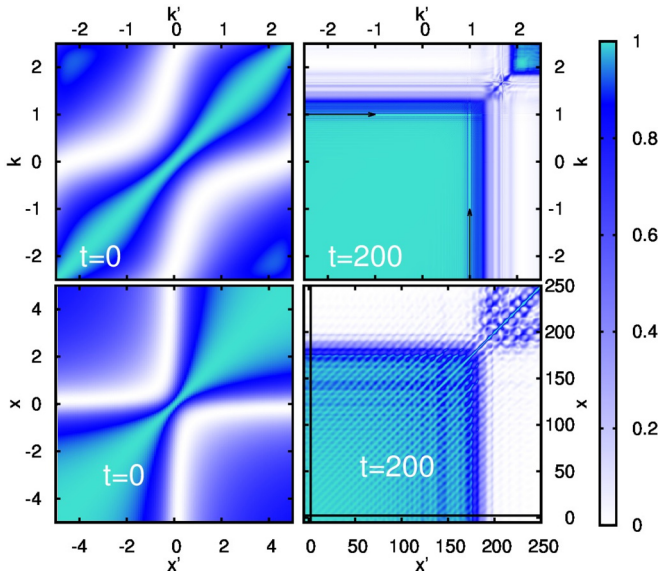

FIG. 4. Spatial and momentum one-body correlation functions of fermion tunneling to open space. We plot the correlation functions $|g^{(1)}(x',x;t)|^2$ and $|g^{(1)}(k',k;t)|^2$ in real and momentum space in the top and bottom rows, respectively, for the $\lambda_0 = 1$ case. In comparison to the bosonic case (see Refs. [41,54]), we observe a generally more strongly correlated behavior in both real and momentum space for the ground states depicted in the left column. In the momentum correlations (top left and top right panels), a line structure emerges at the momenta corresponding to the escaping fermions, k_1,k_2 with time. While the fermions that still reside in the well at $k \approx k' \approx 0$ are almost uncorrelated ($|g^{(1)}|^2 \approx 1$), the fermion escaping with momentum k_1 is uncorrelated with those at rest ($|g^{(1)}(k' \approx k_1, k \approx 0; t = 200)|^2 \approx 0$, see upper right panel). Interestingly, the fermion escaping with k_2 is correlated with the one at rest ($|g^{(1)}(k' \approx k_2, k \approx 0; t = 200)|^2 \approx 1$, see black arrows in top right panel). However, the k_2 velocity is embedded by thin lines where $|g^{(1)}(k' = k_2 \pm \epsilon, k; t = 200)|^2 < 1$ (see dark lines next to the arrows in the top right panel). The periodic structure in the real-space correlation in the bottom right panel reflects the momentum correlations in the top right panel. To guide the eye, we mark the top of the barrier by the black lines. The difference in the escape velocities k_1,k_2 leads to a strong spatial correlation (see rectangular areas with $|g^{(1)}(x,x';t = 200)|^2 \approx 0$ on the off-diagonal of the bottom right panel). All quantities shown are dimensionless; see text for further discussion.

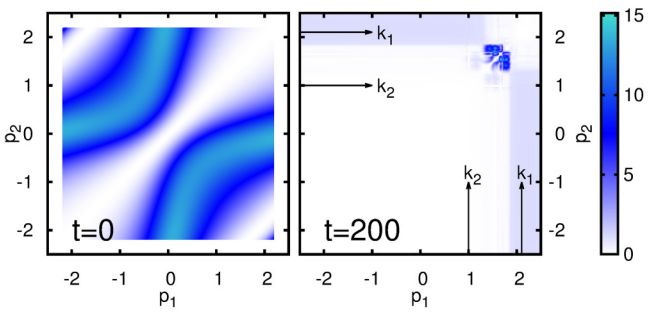

FIG. 5. Momentum two-body correlation functions of fermion tunneling to open space. We plot the correlation functions $g^{(2)}(p_1,p_2,p_1,p_2;t)$ in momentum space, for the $\lambda_0 = 1$ case for times $t = 0$ (left) and $t = 200$ (right). In both panels, the Pauli exclusion principle is manifest, since $g^{(2)}(p,p,p,p) = 0$. For the initial state in the left panel, we find large values of $g^{(2)}(p_1,p_2,p_1,p_2)$, where $|g^{(1)}(p_1,p_2)|^2$ is small and vice versa (cf. top left panel of Fig. 4). This also vaguely holds for the $t = 200$ plot (cf. top right panel of Fig. 4). In the right panel at $t = 200$, the black arrows mark the escape momenta obtained from our model and the momentum distributions (cf. Fig. 3). The $p_{1/2} = k_2 = 1$ tunneling at $p_{1/2} = k_2 = 1.0$ is anticorrelated or antibunched ($g^{(2)} < 1$), whereas the tunneling at $k = 2.103$ is correlated or bunched ($g^{(2)} > 1$). The found correlated pair tunneling process emerges as a strongly bunched structure on the diagonal around $k_{\mathrm{red}} = 1.613$, i.e., $g^{(2)}(k_{\mathrm{red}},k_{\mathrm{red}},k_{\mathrm{red}},k_{\mathrm{red}}) \gg 1$. All quantities shown are dimensionless; see text for further discussion.

The momenta k_1,k_2 are reflected in $|g^{(1)}(x,x';t)|^2$ as periodic structures. The large difference between k_1 and k_2 causes one of the fermions to escape much more quickly than the other. This leads to a strong correlation, i.e., $|g^{(1)}(x,x';t)|^2 \approx 0$ on the off diagonal (cf. white "rectangles" on the off diagonal in the bottom right panel of Fig. 4). Moreover, this strong correlation on the off diagonal of $g^{(1)}$ can be interpreted as a feature of the process being sequential.

Since the overall features in the momentum distributions (peaks corresponding to chemical potentials) and the one-body correlation functions (line structure in k space) are quite similar in the cases of fermions and bosons, we conclude that (i) the model in Fig. 2 initially put forward for bosons is indeed also predictive for the case of fermions and (ii) the process for fermions is likely to allow for a control by the threshold value of the potential $T = \lim_{x\to\infty} V(x,t > 0)$ in the same way as it does for bosons [54]: By changing the threshold T, the peaks in the momentum distribution can be shifted and are turned off when T becomes larger than the chemical potential corresponding to the respective process. The newly discovered feature of correlated two-body escape as well as the found differences in the time evolution of the one-body correlation function are motivating for a more detailed investigation of the process using the two-body correlation.

$$g^{(2)}(\xi_1,\xi_2,\xi_1',\xi_2',t) = \frac{\rho^{(2)}(\xi_1,\xi_2,\xi_1',\xi_2',t)}{\sqrt{\rho^{(1)}(\xi_1,\xi_1,t)\rho^{(1)}(\xi_2,\xi_2,t)\rho^{(1)}(\xi_1',\xi_1',t)\rho^{(1)}(\xi_2',\xi_2',t)}}.$$

Here, $\rho^{(2)}$ is the reduced two-body density [cf. Eq. (8)]. In Fig. 5, we depict a plot of $g^{(2)}$ in momentum space ($\xi = p$) for the case of $\lambda_0 = 1.0$. As a first observation, we find that the two-body correlation function in momentum space exhibits a structure which is complementary to the one-body correlation function $g^{(1)}$ in momentum space (top row of Fig. 4): Wherever $g^{(1)}(p_1,p_2)$ is comparatively large, $g^{(2)}(p_1,p_2,p_1,p_2)$ is comparatively small, and vice versa. Moreover, we can decipher the details of the mechanism of the two-body tunneling to open space: A particle escaping

with $p_1 = k_1 = 2.103$ is bunched with the other particle not having the same momentum, i.e., $g^{(2)}(k_1,a,k_1,a) > 1$ only for $a \neq k_1$ and 0 otherwise (see arrows at $k_1 = 2.103$ in Fig. 5). This means that it is likely that the second particle travels at a different velocity if the first one is found traveling at k_1. Moreover, a particle traveling at velocity $p_1 = k_2 = 1.0$ is bunched with the other particle having the momentum k_2, i.e., $g^{(2)}(k_2,a,k_2,a) > 1$ only for $a \approx k_1$ and 0 otherwise. This underlines the sequential nature of the process: The second particle at k_2 can start its escape only once the other particle has already escaped with the momentum k_1 (see arrows at $k_2 = 1.0$ in Fig. 5). Moreover, the two-body correlation function demonstrates clearly that the peaks in the momentum distributions at k_{red} (cf. top right panel of Fig. 3) indeed correspond to a correlated two-body escape: Two particles escape with similar momenta as $g^{(2)}(p_1,p_2,p_1,p_2)$ exhibits strong bunching on the diagonal around $p_1 \approx p_2 \approx k_{\mathrm{red}}$. This bunching feature in $g^{(2)}$ on the diagonal disappears for the cases in which the peaks around k_{red} are absent in the momentum distributions, i.e., for $\lambda_0 = 0.5$ and $\lambda_0 = 0$ (not shown). This corroborates the finding that the two-body escape we see is indeed an over-the-barrier effect and not tunneling.

IV. CONCLUSIONS AND OUTLOOK

In the present work, we have demonstrated that the MCTDHF theory and algorithm are capable of solving general time-dependent many-fermion problems to an arbitrary degree of accuracy; i.e., we have shown the *numerical exactness* of MCTDHF for the spin-polarized case. We found exponentially converging ground-state energy eigenvalues for the eigenstates of the harmonic interaction model. By solving the time-dependent harmonic interaction model with MCTDHF we demonstrated that even with erratically time-dependent one-body and two-body terms in the Hamiltonian, an exact solution of the time-dependent Schrödinger equation can still be obtained.

We further studied the tunneling to open space process of few-fermion systems composed of charged spin-polarized particles. We assess the validity of a model put forward for the process for bosons with a contact interaction potential also in the present case of fermions interacting with a regularized Coulomb interaction. The prediction of the model for the escape momenta of the fermions is remarkably accurate. From a comparison of the momentum distributions and one-body correlation functions in the process with the model, we infer that the many-fermion tunneling to open space process is built up from sequentially happening single-particle processes whose characteristic momenta $k_1,k_2,\ldots$ emerge from the chemical potentials $\mu_1,\mu_2,\ldots$ of trapped subsystems of decreasing particle number $N,N-1,\ldots$. For the case, where the total energy of the system is sufficiently above the barrier height of the single-particle potential, we find an additional signature in the momentum distributions, which is associated with a correlated two-body escape process. Using the one-body and two-body correlation functions, we were able to demonstrate the sequentiality of the process and that the discussed two-body process corresponds to an over-the-barrier escape and not tunneling.

To scrutinize and investigate the emergent features in the correlation functions for a larger number of particles and other types of interactions are subjects of future work.

As further future applications of our MCTDHF implementation, we envisage for instance studies of statistical relaxation and chaos [55,56], quantum turbulence [57], and vortices [58] as well as Hubbard Hamiltonians [59], electronic decay processes [8], and high-harmonic-order generation [60].

ACKNOWLEDGMENTS

Benchmark results made available by and helpful discussions with Hans-Dieter Meyer as well as the hospitality of Vanderlei S. Bagnato and Marios C. Tsatsos in the CePOF of the IFSC, Saõ Carlos, Saõ Paulo, Brazil, are gratefully acknowledged. Computation time on the CRAY XC40 Hornet/Hazel Hen clusters at the HLRS Stuttgart is gratefully acknowledged. A.U.J.L. gratefully acknowledges financial support by the Swiss SNF and the NCCR Quantum Science and Technology. E.F. gratefully acknowledges funding from the Research Council of Norway (RCN) through CoE Grant No. 179568/V30 (CTCC). Helpful discussions with Christoph Bruder are acknowledged.

[1] E. Deumens, A. Diz, R. Longo, and Y. Öhrn, Time-dependent theoretical treatments of the dynamics of electrons and nuclei in molecular systems, Rev. Mod. Phys. **66**, 917 (1994); H. Feldmeier and J. Schnack, Molecular dynamics for fermions, *ibid.* **72**, 655 (2000).

[2] V. N. Kotov, B. Uchoa, V. M. Pereira, F. Guinea, and A. H. C. Neto, Electron-electron interactions in graphene: Current status and perspectives, Rev. Mod. Phys. **84**, 1067 (2012).

[3] R. B. Laughlin, Quantized motion of three two-dimensional electrons in a strong magnetic field, Phys. Rev. B **27**, 3383 (1983); Anomalous Quantum Hall Effect: An Incompressible Quantum Fluid with Fractionally Charged Excitations, Phys. Rev. Lett. **50**, 1395 (1983).

[4] C. Nayak, S. H. Simon, A. Stern, M. Freedman, and S. Das Sarma, Non-Abelian anyons and topological quantum computation, Rev. Mod. Phys. **80**, 1083 (2008).

[5] M. Köhl, H. Moritz, T. Stöferle, K. Günter, and T. Esslinger, Fermionic Atoms in a Three-Dimensional Optical Lattice: Observing Fermi Surfaces, Dynamics, and Interactions, Phys. Rev. Lett. **94**, 080403 (2005); D. Greif, L. Tarruell, T. Uehlinger, R. Jördens, and T. Esslinger, Probing Nearest-Neighbor Correlations of Ultracold Fermions in an Optical Lattice, *ibid.* **106**, 145302 (2011).

[6] C. Kloeffel, P. A. Dalgarno, B. Urbaszek, B. D. Gerardot, D. Brunner, P. M. Petroff, D. Loss, and R. J. Warburton, Controlling the Interaction of Electron and Nuclear Spins in a Tunnel-Coupled Quantum Dot, Phys. Rev. Lett. **106**, 046802 (2011).

[7] F. M. Pont, A. Bande, and L. S. Cederbaum, Controlled energy-selected electron capture and release in double quantum dots, Phys. Rev. B **88**, 241304(R) (2013).

[8] A. Bande, Electron dynamics of interatomic Coulombic decay in quantum dots induced by a laser field, J. Chem. Phys. **138**, 214104 (2013).

[9] F. Serwane, G. Zürn, T. Lompe, T. B. Ottenstein, A. N. Wenz and S. Jochim, Deterministic preparation of a tunable few-fermion system, Science **332**, 336 (2011).

[10] G. Zürn, A. N. Wenz, S. Murmann, A. Bergschneider, T. Lompe, and S. Jochim, Pairing in Few-Fermion Systems with Attractive Interactions, Phys. Rev. Lett. **111**, 175302 (2013).

[11] S. Murmann, A. Bergschneider, V. M. Klinkhamer, G. Zürn, T. Lompe, and S. Jochim, Two Fermions in a Double Well: Exploring a Fundamental Building Block of the Hubbard Model, Phys. Rev. Lett. **114**, 080402 (2015).

[12] A. N. Wenz, G. Zürn, S. Murmann, I. Brouzos, T. Lompe, S. Jochim, From few to many: Observing the formation of a Fermi sea one atom at a time, Science **342**, 457 (2013).

[13] E. H. Lieb and W. Liniger, Exact analysis of an interacting Bose gas, I: The general solution and the ground state, Phys. Rev. **130**, 1605 (1963).

[14] M. D. Girardeau, E. M. Wright, and J. M. Triscari, Ground-state properties of a one-dimensional system of hard-core bosons in a harmonic trap, Phys. Rev. A **63**, 033601 (2001).

[15] M. A. Załuska-Kotur, M. Gajda, A. Orłowski, and J. Mostowski, Soluble model of many interacting quantum particles in a trap, Phys. Rev. A **61**, 033613 (2000).

[16] J. Yan, Harmonic interaction model and its applications in Bose-Einstein condensation, J. Stat. Phys. **113**, 623 (2003).

[17] L. Cohen and C. Lee, Exact reduced density matrices for a model problem, J. Math. Phys. **26**, 3105 (1985).

[18] J. Frenkel and P. A. M. Dirac, *Wave Mechanics* (Oxford University Press, Oxford, UK, 1934); P. A. M. Dirac, Note on exchange phenomena in the Thomas atom, Proc. Cambridge Phil. Soc. **26**, 376 (1930).

[19] P. Kramer and M. Saraceno, *Geometry of the Time-Dependent Variational Principle in Quantum Mechanics*, Lecture Notes in Physics 140 (Springer, Heidelberg, Germany, 1981).

[20] L. P. Pitaevskii, Vortex lines in an imperfect Bose gas, JETP **40**, 646 (1961); E. P. Gross, Structure of a quantized vortex in boson systems, Nuovo Cimento **20**, 454 (1961).

[21] L. Pitaevskii and S. Stringari, *Bose-Einstein Condensation* (Oxford University Press, New York, 2003).

[22] O. E. Alon, A. I. Streltsov, and L. S. Cederbaum, Time-dependent multi-orbital mean-field for fragmented Bose-Einstein condensates, Phys. Lett. A **362**, 453 (2007).

[23] A. D. McLachlan and M. A. Ball, Time-dependent Hartree-Fock theory for molecules, Rev. Mod. Phys. **36**, 844 (1964).

[24] H.-D. Meyer, U. Manthe, and L. S. Cederbaum, The multi-configurational time-dependent Hartree approach, Chem. Phys. Lett. **165**, 73 (1990).

[25] M. H. Beck, A. Jäckle, G. A. Worth, and H. D. Meyer, The multiconfiguration time-dependent Hartree method: A highly efficient algorithm for propagating wave packets, Phys. Rep. **324**, 1 (2000).

[26] U. Manthe, H.-D. Meyer and L. S. Cederbaum, Wave-packet dynamics within the multiconfiguration Hartree framework: General aspects and application to NOCl, J. Chem. Phys. **97**, 3199 (1992).

[27] O. E. Alon, A. I. Streltsov, and L. S. Cederbaum, Multiconfigurational time-dependent Hartree method for bosons: Many-body dynamics of bosonic systems, Phys. Rev. A **77**, 033613 (2008).

[28] A. I. Streltsov, O. E. Alon, and L. S. Cederbaum, Formation and Dynamics of Many-Boson Fragmented States in One-Dimensional Attractive Ultracold Gases, Phys. Rev. Lett. **100**, 130401 (2008).

[29] D. J. Masiello and W. P. Reinhardt, Time-dependent quantum many-body theory of identical bosons in a double well: Early-time ballistic interferences of fragmented and number entangled states, Phys. Rev. A **76**, 043612 (2007).

[30] L. Cao, S. Krönke, O. Vendrell, and P. Schmelcher, The multi-layer multi-configuration time-dependent Hartree method for bosons: Theory, implementation, and applications, J. Chem. Phys. **139**, 134103 (2013).

[31] J. Caillat, J. Zanghellini, M. Kitzler, O. Koch, W. Kreuzer, and A. Scrinzi, Correlated multielectron systems in strong laser fields: A multiconfiguration time-dependent Hartree-Fock approach, Phys. Rev. A **71**, 012712 (2005); J. Zanghellini, M. Kitzler, C. Fabian, T. Brabec, and A. Scrinzi, An MCTDHF approach to multielectron dynamics in laser fields, Laser Phys. **13**, 1064 (2003).

[32] T. Kato and H. Kono, Time-dependent multiconfiguration theory for electronic dynamics of molecules in an intense laser field, Chem. Phys. Lett. **392**, 533 (2004).

[33] M. Nest, T. Klamroth, and P. Saalfrank, The multiconfiguration time-dependent Hartree–Fock method for quantum chemical calculations, J. Chem. Phys. **122**, 124102 (2005).

[34] O. E. Alon, A. I. Streltsov, and L. S. Cederbaum, Unified view on multiconfigurational time propagation for systems consisting of identical particles, J. Chem. Phys. **127**, 154103 (2007).

[35] D. J. Haxton, K. V. Lawler, and C. W. McCurdy, Multiconfiguration time-dependent Hartree-Fock treatment of electronic and nuclear dynamics in diatomic molecules, Phys. Rev. A **83**, 063416 (2011).

[36] D. Hochstuhl, S. Bauch, and M. Bonitz, Multiconfigurational time-dependent Hartree-Fock calculations for photoionization of one-dimensional helium, J. Phys.: Conf. Ser. **220**, 012019 (2010).

[37] A. U. J. Lode, K. Sakmann, O. E. Alon, L. S. Cederbaum, and A. I. Streltsov, Numerically exact quantum dynamics of bosons with time-dependent interactions of harmonic type, Phys. Rev. A **86**, 063606 (2012).

[38] A. U. J. Lode, *Tunneling Dynamics in Open Ultracold Bosonic Systems* (Springer, Heidelberg, Germany, 2015).

[39] K. Sakmann, *Many-Body Schrödinger Dynamics of Bose-Einstein Condensates* (Springer, Heidelberg, Germany, 2011).

[40] A. I. Streltsov, O. E. Alon, and L. S. Cederbaum, General mapping for bosonic and fermionic operators in Fock space, Phys. Rev. A **81**, 022124 (2010).

[41] A. U. J. Lode, A. I. Streltsov, K. Sakmann, O. E. Alon, and L. S. Cederbaum, How an interacting many-body system tunnels through a potential barrier to open space, Proc. Natl. Acad. Sci. U.S.A. **109**, 13521 (2012).

[42] A. U. J. Lode and M. C. Tsatsos, *The Recursive Multiconfigurational Time-Dependent Hartree for Bosons package (2015)*, http://ultracold.org; http://r-mctdhb.org; http://schroedinger.org.

[43] A. U. J. Lode and M. C. Tsatsos, MCTDH-X: *The Multiconfigurational Time-Dependent Hartree for indistinguishable particles software*, http://ultracold.org; http://mctdh.bf; http://schroedinger.org (2016).

[44] A. I. Streltsov, Quantum systems of ultracold bosons with customized interparticle interactions, Phys. Rev. A **88**, 041602(R) (2013).

[45] O. I. Streltsova, O. E. Alon, L. S. Cederbaum, and A. I. Streltsov, Generic regimes of quantum many-body dynamics of trapped bosonic systems with strong repulsive interactions, Phys. Rev. A **89**, 061602(R) (2014).

[46] R. Beinke, S. Klaiman, L. S. Cederbaum, A. I. Streltsov, O. E. Alon, Many-body tunneling dynamics of Bose-Einstein condensates and vortex states in two spatial dimensions, Phys. Rev. A **92**, 043627 (2015).

[47] R. J. Glauber, The quantum theory of optical coherence, Phys. Rev. **130**, 2529 (1963).

[48] K. Sakmann, A. I. Streltsov, O. E. Alon, and L. S. Cederbaum, Reduced density matrices and coherence of trapped interacting bosons, Phys. Rev. A **78**, 023615 (2008).

[49] See Supplemental Material at http://link.aps.org/supplemental/10.1103/PhysRevA.93.033635 for a benchmark of MCTDHF with the eigenstates of the time-independent harmonic interaction model.

[50] R. Kosloff, Time-dependent quantum-mechanical methods for molecular dynamics, J. Chem. Phys. **92**, 2087 (1988); W. H. Press, S. A. Teukolsky, W. T. Vetterling, and B. P. Flannery, *Numerical Recipes in Fortran* (Cambridge University Press, Cambridge, UK, 1992).

[51] S. E. Gharashi and D. Blume, Tunneling dynamics of two interacting one-dimensional particles, Phys. Rev. A **92**, 033629 (2015).

[52] M. Rontani, Tunneling Theory of Two Interacting Atoms in a Trap, Phys. Rev. Lett. **108**, 115302 (2012).

[53] A. U. J. Lode, A. I. Streltsov, O. E. Alon, H.-D. Meyer, and L. S. Cederbaum, Exact decay and tunneling dynamics of interacting few-boson systems, J. Phys. B: At. Mol. Opt. Phys. **42**, 044018 (2009); Corrigendum, **43**, 029802 (2010).

[54] A. U. J. Lode, S. Klaiman, O. E. Alon, A. I. Streltsov, and L. S. Cederbaum, Controlling the velocities and the number of emitted particles in the tunneling to open space dynamics, Phys. Rev. A **89**, 053620 (2014).

[55] I. Březinová, A. U. J. Lode, A. I. Streltsov, O. E. Alon, L. S. Cederbaum, and J. Burgdörfer, Wave chaos as signature for depletion of a Bose-Einstein condensate, Phys. Rev. A **86**, 013630 (2012).

[56] A. U. J. Lode, B. Chakrabarti, and V. K. B. Kota, Many-body entropies, correlations, and emergence of statistical relaxation in interaction quench dynamics of ultracold bosons, Phys. Rev. A 92, 033622 (2015).

[57] M. C. Tsatsos and A. U. J. Lode, Vortex nucleation through fragmentation in a stirred resonant Bose-Einstein condensate, J. L. Temp. Phys. **181**, 171 (2015).

[58] S. E. Weiner, M. C. Tsatsos, L. S. Cederbaum, and A. U. J. Lode, Angular momentum in interacting many-body systems hides in phantom vortices, arXiv:1409.7670 [cond-mat.quant-gas] (unpublished).

[59] A. U. J. Lode and C. Bruder, Dynamics of Hubbard Hamiltonians with the multiconfigurational time-dependent Hartree for indistinguishable particles (unpublished).

[60] M. Lewenstein, Ph. Balcou, M. Yu. Ivanov, A. L'Huillier, and P. B. Corkum, Theory of high-harmonic generation in low-frequency laser fields, Phys. Rev. A **49**, 2117 (1994).

The Journal of Chemical Physics

Relativistic decay widths of autoionization processes: The relativistic FanoADC-Stieltjes method

Cite as: J. Chem. Phys. **142**, 144106 (2015); https://doi.org/10.1063/1.4917255
Submitted: 24 December 2014 . Accepted: 30 March 2015 . Published Online: 10 April 2015

Elke Fasshauer, Přemysl Kolorenč, and Markus Pernpointner

Relativistic decay widths of autoionization processes: The relativistic FanoADC-Stieltjes method

Elke Fasshauer,[1,2,a)] Přemysl Kolorenč,[3] and Markus Pernpointner[2]
[1]*Centre for Theoretical and Computational Chemistry, Department of Chemistry, University of Tromsø–The Arctic University of Norway, N-9037 Tromsø, Norway*
[2]*Theoretische Chemie, Universität Heidelberg, Im Neuenheimer Feld 229, D-69120 Heidelberg, Germany*
[3]*Institute of Theoretical Physics, Faculty of Mathematics and Physics, Charles University in Prague, V Holešovičkách 2, 180 00 Prague, Czech Republic*

(Received 24 December 2014; accepted 30 March 2015; published online 10 April 2015)

Electronic decay processes of ionized systems are, for example, the Auger decay or the Interatomic/Intermolecular Coulombic Decay. In both processes, an energetically low lying vacancy is filled by an electron of an energetically higher lying orbital and a secondary electron is instantaneously emitted to the continuum. Whether or not such a process occurs depends both on the energetic accessibility and the corresponding lifetime compared to the lifetime of competing decay mechanisms. We present a realization of the non-relativistically established FanoADC-Stieltjes method for the description of autoionization decay widths including relativistic effects. This procedure, being based on the Algebraic Diagrammatic Construction (ADC), was adapted to the relativistic framework and implemented into the relativistic quantum chemistry program package Dirac. It is, in contrast to other existing relativistic atomic codes, not limited to the description of autoionization lifetimes in spherically symmetric systems, but is instead also applicable to molecules and clusters. We employ this method to the Auger processes following the $Kr3d^{-1}$, $Xe4d^{-1}$, and $Rn5d^{-1}$ ionization. Based on the results, we show a pronounced influence of mainly scalar-relativistic effects on the decay widths of autoionization processes. © *2015 AIP Publishing LLC.* [http://dx.doi.org/10.1063/1.4917255]

I. INTRODUCTION

Electronic vacancies in the sub-outer-valence orbital of an atom or molecule created by radiation or radioactive decay are excited systems. These excited systems can decay via multiple pathways like photon emission, coupling to vibrational degrees of freedom or via electronic decay processes like the Auger decay,[1,2] or the manifold of Interatomic/Intermolecular Coulombic Decay (ICD) processes,[3,4] both being autoionization processes. The latter can occur in small[5–7] and large[4,8–11] noble gas clusters, as well as clusters of molecules like water,[12–16] ammonia,[17] or hydrogen fluoride[3,18] after exposure to synchrotron radiation, in enzymes of the human body,[19] in the mechanisms of cancer drugs,[20–25] and quantum dots in semiconductors[26] just to name a few examples.

Electronic decay processes in general can occur if two criteria, the energy and the coupling criterion, are fulfilled. To fulfill the energy criterion, the final state energy is required to be lower than the energy of the singly ionized initial state. If this is not the case, the channel defined by a certain doubly ionized final state is closed and the corresponding fragments of the channel are not observed after the decay. To fulfill the coupling criterion, the decay process needs to be fast enough to prevail over other energetically accessible decay pathways. It hence contains the information whether an energetically allowed process can be expected to be observed experimentally or not. Therefore, a typical study of autoionization processes consists of two parts.

- Determination of the kinetic energy of the secondary electron and, as a consequence, which decay channels are open.
- Calculation of the decay width $\Gamma = \frac{\hbar}{\tau}$, which is proportional to the decay rate $\frac{1}{\tau}$ and inversely proportional to the lifetime τ.

Especially in systems containing heavy elements or initial ionizations from the core region, relativistic effects play an important role and cannot be neglected. Phenomenologically, the relativistic effects can be divided into spin-orbit coupling and scalar-relativistic effects. The spin-orbit coupling requires the system to be described in terms of the total angular momentum j rather than the orbital momentum l and the spin momentum s. Thereby, the non-relativistically degenerate states of one particular l value are split into two states with $j = l \pm s$ of different energies.[27] The scalar-relativistic effects result in spatial contractions of the s and p orbitals and decontraction of d and f orbitals.[27]

Spin-orbit coupling has been shown to cause a larger number of distinguishable channels in ICD-like processes.[28] At the same time, the influence of the spin-orbit splitting using asymptotic formulas based on experimental data of the atoms was investigated. The results showed only minor deviations of the decay widths due to spin-orbit coupling in the case of all channels being open. However, this approach intrinsically includes scalar-relativistic effects, which are automatically included in the experimental data used. In order to investigate also the influence of scalar-relativistic effects and to enable a relativistic description at short bond distances, the

a)Email: Elke.Fasshauer@uit.no

purpose of this paper is to present the *ab initio* relativistic FanoADC-Stieltjes method for the determination of decay widths. From our calculations, we gain further insights into the influence of relativistic (mainly scalar-relativistic) effects on Auger processes and from these, generalize our findings for autoionization processes.

In both autoionization processes (Auger and ICD), the initial vacancy is filled with an electron of higher energy and the excess energy is transferred to another electron, which is finally emitted. Hence, the final state is characterized by a doubly charged system and an electron in the continuum. Our subject of interest is mainly the ICD-like processes. However, due to the similarity between the autoionization processes, methods developed for the description of ICD-like processes can also be applied to the Auger process, where more data from theory and experiment are available for comparison.

In this work, we therefore focus on the atomic Auger process as a model system in order to exploit basic knowledge about the influence of relativistic effects. The Auger decay process initiated by a photoionization can most generally be described by

$$A \xrightarrow{h\nu} (A^+)^* + e^-_{ph} \xrightarrow{Auger} A^{2+} + e^-_{ph} + e^-_{sec}.$$

A system A is ionized, while the photo-electron e^-_{ph} is emitted. Afterwards, the actual Auger process of the initial state A^+ can occur. An electron from an outer shell fills the vacancy and the excess energy is instantaneously transferred to another (secondary) electron e^-_{sec}, which is subsequently emitted. The final state of the decay process is to be described by a doubly charged atom A^{2+} and the secondary electron in the continuum.

The initial and final state energies can be obtained using a variety of quantum chemical approaches known in the literature as the Algebraic Diagrammatic Construction[29–32] (ADC), which is also available for a fully relativistic treatment.[33–35] On the other hand, the evaluation of decay widths Γ is a highly non-trivial problem. Analytically, it can be described by the theories of Feshbach and Fano.[36–38] However, this theory naturally incorporates the description of both bound and continuum states, which describe the initial and final state, respectively. These different kinds of states satisfy different boundary conditions, i.e., the boundary conditions of bound states being of $\mathcal{L}^2$-type and the boundary conditions of plane waves in case of the final state because of the freely moving electron. Any approach will have to stick to either $\mathcal{L}^2$-functions, plane waves or to combine these two in some way connecting the bound with the continuum functions. Either of these approaches faces difficulties in either describing the bound or the continuum states or some artificially constructed interface region.

It is most convenient to start from an $\mathcal{L}^2$-function based approach, because most quantum chemical programs are based on this kind of functions and hence the basic ingredients necessary for a decay width calculation like SCF and integral transformation are already available. The quantum chemical methods, which have been used for non-relativistic descriptions of the decay widths are the Wigner-Weisskopf theory,[39] CAP-CI (Complex Absorbing Potential based on a Configuration Interaction wavefunction),[6,40] CAP-ADC,[41] CAP/EOM-CCSD (Equation of Motion Coupled Cluster with Singles and Doubles)[42] and the FanoADC-Stieltjes method.[43] While the CAP-based methods have the most sound formal basis of the methods above, they suffer from wrong densities and populations for many-particle systems and are computationally expensive at the same time. In contrast to this, the Wigner-Weisskopf theory is based on the lowest non-vanishing order of perturbation theory and therefore computationally affordable even for large systems. However, the price for the lower computational costs is less accurate results. A compromise between accuracy and computational cost is the FanoADC-Stieltjes approach, which is based on the ADC and therefore includes higher perturbational orders and is size-consistent. For these reasons, the FanoADC-Stieltjes method was implemented in the relativistic quantum chemical program package Dirac.[44] We present first results obtained with the relativistic FanoADC-Stieltjes method in this work.

So far, relativistic decay widths were calculated using Multichannel Multi-Configurational Dirac-Fock (MMCDF).[45] However, this approach does not only highly depend on manual selection of CI (Configuration Interaction) components to be included in the description of initial and final state, it moreover is not capable of describing systems with less than spherical symmetry. This reduces the applicability of the method to atomic Auger processes, but allows us to compare our results obtained with the relativistic FanoADC-Stieltjes method for exactly this special case.

Based on the results for the Auger process following the $(n-1)d^{-1}$ ionization of the noble gases krypton, xenon, and radon, we are going to show the importance of including relativistic effects into decay width calculations based on comparisons of four-component Dirac-Coulomb (including spin-orbit coupling and scalar-relativistic effects), scalar-relativistic, and non-relativistic results.

The paper is structured as follows: in Sec. II, we explain the physical definition of the decay widths and the three compounds of the FanoADC-Stieltjes method: ADC, FanoADC, and Stieltjes imaging. We then give the computational details for our *ab initio* calculations in Sec. III and present our results for the Auger process after an initial ionization of the $(n-1)$d of krypton, xenon, and radon. We discuss the influence of relativistic effects on the decay widths of autoionization processes in Sec. IV. We then draw conclusions in Sec. V.

II. THEORY

Following Wentzel[46] and later Feshbach[36,38] and Fano,[37] the decay width of a decay process initiated by a primary ionization is given by

$$\Gamma = \sum_{\beta} 2\pi \left| \langle \Phi | \hat{V} | \chi_{\beta,\varepsilon} \rangle \right|^2 . \tag{1}$$

Here, $|\Phi\rangle$ and $|\chi_{\beta,\varepsilon}\rangle$ denote the initial and final state, respectively. $\hat{V}$ is the interaction operator of the initial and final states, which in Feshbach's definitions is known as H_{PQ}. The index β counts the different decay channels and ε denotes the energy of the final state. Equation (1) thereby connects the metastable initial and the continuum final states.

They are constructed by partitioning the Hamiltonian into two subspaces. The initial (final) state is then an eigenfunction of this initial (final) state sub-space Hamiltonian. However, finding proper solutions to both the initial and the final states on an equal footing is a non-trivial task, because they adhere to different boundary conditions. Since the final state depends on the energy of the emitted electron, any approach needs to either determine the continuum state or to mimic the final state using $\mathcal{L}^2$-functions. While the continuum functions are normalized with respect to their energy,

$$\langle \chi_\varepsilon | \chi_{\varepsilon'} \rangle = \delta(\varepsilon - \varepsilon'), \tag{2}$$

the $\mathcal{L}^2$ approach is based on a discrete set of final states $|\tilde{\chi}_{\tilde{E}}\rangle$ which adhere to different boundary conditions and are normalized with respect to space (see, e.g., Ref. 47),

$$\langle \tilde{\chi}_{\tilde{E}_i} | \tilde{\chi}_{\tilde{E}_j} \rangle = \delta_{ij}. \tag{3}$$

Because of this different normalization, the decay widths are not amenable to a direct calculation. As first proposed by Hazi,[48] for autoionization processes such difficulties can be solved by using the Stieltjes-Chebyshev moment theory also called Stieltjes imaging.[49–51] It relies on the observation that the moments of the projected final state Hamiltonian H_f,

$$\mu_k = \langle \Phi | \hat{V} H_f^k \hat{V} | \Phi \rangle, \tag{4}$$

calculated from the determined discrete pseudo-spectrum are good approximations to the moments determined from the real continuum states. This can be shown by inserting the resolution of identity for the continuum states

$$\mu_k = \sum_i \varepsilon_i^k \left| \langle \Phi | \hat{V} | \chi_{i,\varepsilon} \rangle \right|^2 + \int_{E_{thr}}^{\infty} \varepsilon^k \left| \langle \Phi | \hat{V} | \chi_\varepsilon \rangle \right|^2 \mathrm{d}\varepsilon. \tag{5}$$

Since the non-zero contribution to the coupling matrix elements in the Feshbach-Fano approach stems only from an interaction region of finite size, where the $\mathcal{L}^2$ final state functions are nonvanishing, we may replace the expansion $\sum_i |\chi_{i,\varepsilon}\rangle\langle\chi_{i,\varepsilon}| + \int \mathrm{d}\varepsilon |\chi_\varepsilon\rangle\langle\chi_\varepsilon|$ by its $\mathcal{L}^2$ approximation $\sum_j |\tilde{\chi}_{\tilde{E}_j}\rangle\langle\tilde{\chi}_{\tilde{E}_j}|$ (see Ref. 52),

$$\mu_k \approx \sum_j \tilde{E}_j^k \left| \langle \Phi | \hat{V} | \tilde{\chi}_{\tilde{E}_j} \rangle \right|^2. \tag{6}$$

Then the decay width can be determined through a series of consecutive approximations to the moments of increasing order k.

To achieve this kind of description, we choose the non-relativistic FanoADC-Stieltjes approach, described in Secs. II A–II C. Here, the ADC is used for the description of the initial and final states and the resulting discrete pseudo-spectrum is then subject to a Stieltjes imaging procedure. An exhaustive description of the method can be found in Ref. 53.

A. ADC

The ADC is a Green's function approach, which is a method for the calculation of ionization energies and electron affinities. Its advantage is the ability to determine the desired ionization energies without explicit calculation of the initial and final states, but instead obtaining their energy differences directly. Moreover, this approach is size-consistent and is hence suitable for the description of larger systems.[32]

Originally, the Green's function was formulated in the Dyson ansatz and determined using perturbation theory.[29,54] This way, both the ionization and the electron affinity part had to be included in the description. In the non-Dyson scheme, those two are separable and hence, the dimension of the problem is reduced when one is interested in either the $N+1$ (electron affinity) or the $N-1$ (ionization energy) part[31]

$$G_{pq}(\omega) = G^+_{pq}(\omega) + G^-_{pq}(\omega). \tag{7}$$

The ionization part $G^-_{pq}(\omega)$ is a function of the ionization energies ω and is transposed to give $\tilde{G}^-_{pq}(\omega) = G^-_{qp}(\omega)$. It can be cast to the compact and orthogonal form

$$\tilde{\mathbf{G}}^-(\omega) = \mathbf{x}^\dagger(\omega \mathbb{1} - \mathbf{\Omega})^{-1}\mathbf{x}, \tag{8}$$

where $\mathbf{x}$ are the spectroscopic amplitudes and $\mathbf{\Omega}$ is the diagonal matrix of energy eigenvalues. This diagonal representation can be reformulated using so-called *intermediate states* (IS),[30]

$$\tilde{\mathbf{G}}^-(\omega) = \mathbf{f}^\dagger(\omega \mathbb{1} - \mathbf{M})^{-1}\mathbf{f}. \tag{9}$$

Here, $\mathbf{M}$ denotes the ADC matrix and $\mathbf{f}$ denotes the effective transition moments.

By inspection of both Eqs. (8) and (9), the ionization energies are poles of $\tilde{\mathbf{G}}^-(\omega)$, which can be determined by solving the eigenvalue problem

$$\mathbf{MY} = \mathbf{Y\Omega}, \quad \text{with } \mathbf{Y}^\dagger\mathbf{Y} = \mathbf{1}. \tag{10}$$

The spectroscopic amplitudes $\mathbf{x}$ can then be obtained from the effective transition moments $\mathbf{f}$ as

$$\mathbf{x} = \mathbf{Y}^\dagger\mathbf{f}. \tag{11}$$

To this point, the approach is exact. For the actual construction of the ADC matrix $\mathbf{M}$ and the effective transitions moments $\mathbf{f}$, both are expanded into orders of perturbations based on the Møller-Plesset partitioned Hamiltonian,

$$\mathbf{M} = \mathbf{M}^{(0)} + \mathbf{M}^{(1)} + \mathbf{M}^{(2)} + \cdots, \tag{12}$$

$$\mathbf{f} = \mathbf{f}^{(0)} + \mathbf{f}^{(1)} + \mathbf{f}^{(2)} + \cdots. \tag{13}$$

From these, different orders of perturbation theory of the Hamiltonian can be constructed successively in terms of correlated $N-1$ particle states ($1h$, $2h1p$, …). Hereby, the truncation after the n-th order leads to ADC(n). The contributions to the different classes for different orders of ADC are shown in Figure 1.[55]

The matrix elements of ADC(2x) are explicitly given by

- $1h/1h$ ($1h$ block):

$$M^{(0)}_{kk'} = \varepsilon_k \delta_{kk'}, \tag{14}$$

$$M^{(1)}_{kk'} = 0, \tag{15}$$

$$M^{(2)}_{kk'} = -\frac{1}{2}\sum_{abl} V_{ab[kl]} V_{k'l[ab]} \times \frac{\varepsilon_a + \varepsilon_b - \varepsilon_l - \frac{1}{2}\varepsilon_k - \frac{1}{2}\varepsilon_{k'}}{(\varepsilon_a + \varepsilon_b - \varepsilon_k - \varepsilon_l)(\varepsilon_a + \varepsilon_b - \varepsilon_{k'} - \varepsilon_l)}. \tag{16}$$

	1h	2h1p
1h	0,1,2,2,3	–,–,1,1,2
2h1p	–,–,1,1,2	–,–,0,1,1

FIG. 1. Schematic illustration of an ADC(n) matrix for different orders of perturbation for $n = 0, 1, 2, 2x, 3$. In the illustration, the respective highest order contribution is shown for the different blocks. Hence, ADC(2x) is an extended ADC(2) including first order contributions to the satellite block.

- $1h/2h1p$ (coupling block):

$$M^{(1)}_{j,akl} = V_{kl[aj]}. \tag{17}$$

- $2h1p/2h1p$ (satellite block):

$$M^{(0)}_{akl,a'k'l'} = (-\varepsilon_a + \varepsilon_k + \varepsilon_l)\,\delta_{aa'}\delta_{kk'}\delta_{ll'}, \tag{18}$$

$$M^{(1)}_{akl,a'k'l'} = -\delta_{aa'}V_{k'l'[kl]} + \delta_{kk'}V_{al'[a'l]} + \delta_{ll'}V_{ak'[a'k]} - (k \leftrightarrow l). \tag{19}$$

Here, ε_r denotes the r-th Hartree Fock orbital energy. The occupied states are labelled by $i, j, k, \ldots$ and the unoccupied states are labelled by $a, b, c, \ldots$. The two-electron integrals for any combination of occupied and unoccupied orbitals labelled by p, q, r, s read as

$$V_{pqrs} = \langle\varphi_p(1)\varphi_q(2)|V(1,2)|\varphi_r(1)\varphi_s(2)\rangle \tag{20}$$

and $V_{pq[rs]} = V_{pqrs} - V_{pqsr}$.

These equations can also be used in the relativistic case based on Dirac-Hartree-Fock orbital energies as well as integrals[33,34] and using the no-pair approximation (see, e.g., Ref. 27). This approximation ensures that pair creation processes are excluded from the calculation by allowing annihilation and creation operators c_p and $c_q^\dagger$ in the spectral representation

$$G^-_{pq}(\omega) = \sum_{n\in\{N-1\}} \frac{\langle\Psi_0^N|c_q^\dagger|\Psi_n^{N-1}\rangle\langle\Psi_n^{N-1}|c_p|\Psi_0^{N-1}\rangle}{\omega + E_n^{N-1} - E_0^N - i\eta} \tag{21}$$

of Eq. (7) to operate on the space of positive energy solutions only. Since energies high enough to overcome the gap of $2mc^2$ are hardly achieved in chemistry, this approximation is reasonable.

B. FanoADC

In the FanoADC, the discrete ADC Hamiltonian is used for the construction of the pseudo-spectrum of the total decay width Γ. Due to multiple possible final states, the procedure of Feshbach[38] using projection operators for the partitioning of the Hamiltonian into an initial and a final state subspace is employed. The processes of interest start from a singly ionized initial state and end in a doubly ionized final state with an additional electron in the continuum. Therefore, the basis functions for the description of the entire final state subspace are chosen from the $2h1p$ class of configurations, where the $2h$ part is assumed to describe the doubly ionized final state and the particle represents the electron in the continuum. This approach can be justified by rewriting the spectral moments (see Eq. (6)) of the decay width Γ (Eq. (1)) explicitly

$$\tilde{\Gamma}_k = 2\pi\mu_k \tag{22}$$

$$= 2\pi\sum_j \tilde{E}_j^k\langle\Phi|\hat{V}|\tilde{\chi}_{\tilde{E}_j}\rangle\langle\tilde{\chi}_{\tilde{E}_j}|\hat{V}|\Phi\rangle \tag{23}$$

$$\approx 2\pi\sum_q \left(E_q^{2h1p}\right)^k\langle\Phi|\hat{V}|\chi_q^{2h1p}\rangle\langle\chi_q^{2h1p}|\hat{V}|\Phi\rangle. \tag{24}$$

One may interpret the set of final states as a complete basis of the final state subspace. This might be replaced by any other complete basis describing the outgoing electron. The idea of the FanoADC is to choose the manifold of $2h1p$ states describing the decay to replace this complete basis. As shown in Ref. 43, this basis is not required to yield the exact energies of the different channels as long as it spans the space of interest. The manifold of $2h1p$ states is formally not complete, but yields a proper description when the ionization of the system can be described reasonably well in the single-particle picture. Additionally, one has to consider the error introduced by using an incomplete basis set on the Hartree-Fock level and the truncation of the virtual space in the post Hartree-Fock procedure.

Not all $2h1p$ states describe energetically allowed final states. The energy conservation $E_{in} = E_{A^{2+}} + E_{e^-_{sec}}$ has to be satisfied, which is only possible for $E_{A^{2+}} < E_{in}$, where E_{in} denotes the initial state energy, $E_{A^{2+}}$ the energy of the doubly ionized part of the final state, and $E_{e^-_{sec}}$ denotes the kinetic energy of the secondary electron emitted in the process. If the energy of the doubly charged system is higher than the energy of the initial state, the process is energetically forbidden. Hence, all $2h1p$ states characterized by a $2h$ contribution with an energy higher than the initial state energy will not contribute to the final states. Instead, these $2h1p$ states can be used to improve the description of the initial state. The partitioning into initial and final state configurations can be achieved based on Hartree-Fock orbital occupations by manual choice of $2h$ configurations or in an energy-based approach as described by Averbukh.[43] In this work, we employ the partitioning by population and manually include those configurations which correspond to open channels.

The partitioning is therefore achieved as follows. All $2h1p$ configurations characterized by a $2h$ part corresponding to one of the final state configurations of possible decay channels are chosen to be part of the final state subspace. All $1h$ configurations and those $2h1p$ configurations not corresponding to a possible final state configuration are used for the description of the initial state. This leads to a resorted ADC matrix as shown in Figure 2, where the subspace of the initial state is denoted by **M**, the final state subspace by **N**, and the interaction coupling those two subsets is named **W**.

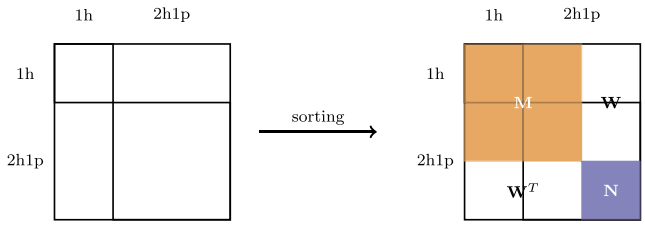

FIG. 2. Schematic illustration of the partitioning of the ADC matrix according to the projection operators of the initial and final states.

Speaking in terms of Feshbach's projection operators, where **P** denotes the projector for the final state subspace acting on the full Hamiltonian of the system **H** and $\mathbf{Q} = \mathbb{1} - \mathbf{P}$ denotes the projector for the initial state subspace, these subspaces are given by $\mathbf{M} = \mathbf{QHQ}$ and $\mathbf{N} = \mathbf{PHP}$.

The separate diagonalization of the initial and final state subspaces **M** and **N** yields the corresponding eigenvectors and eigenvalues on the diagonal of the matrices **Λ** and **Ω**,

$$\mathbf{\Lambda} = \mathbf{I}^T\mathbf{MI}, \tag{25}$$

$$\mathbf{\Omega} = \mathbf{F}^T\mathbf{NF}, \tag{26}$$

and the Hamiltonian is represented in the basis of their eigenstates as illustrated in Figure 3 with $\mathbf{V} = \mathbf{I}^T\mathbf{WF}$ being the interaction part in this new basis. It has to be noticed that **Ω** in this definition is the matrix of final state subspace eigenvalues and does not equal the eigenvalue matrix of the full ADC matrix in Eq. (8).

In general, neither of the final state energies $\bar{\omega}_q$ equals the resonance energy. Therefore, the pseudo-spectrum enters the Stieltjes calculation. For a specific choice of the initial state i, this pseudo-spectrum is given by the manifold of final state energies $\bar{\omega}_q$ and the corresponding interaction part in the basis of the initial and final subspace eigenstates $V_{i,q} = \langle\phi_i|\hat{V}|\psi_q^{2h1p}\rangle$.

C. Stieltjes imaging

In general, Gaussian quadrature is a numerical method to solve integrals. From the discrete pseudo-spectrum consisting of $\bar{\omega}_q$ and $V_{i,q} = \langle\phi_i|\hat{V}|\psi_q^{2h1p}\rangle$, N pairs of optimal abscissae $(1/\omega_i)$ and weights f_i for a Gaussian quadrature can be obtained using Chebyshev polynomials as elaborately described in Ref. 51. These are then used for the construction of inverse moments, which are preferred to normal moments because of their convergence behaviour

$$S(-k) = \int_{E_{thr}}^{\infty} \omega^{-k}\,\mathrm{d}F(\omega) = \int_{E_{thr}}^{\infty} \omega^{-k} f(\omega)\,\mathrm{d}\omega \approx \sum_{i=1}^{N}\left(\frac{1}{\omega_i}\right)^k f_i. \tag{27}$$

The inverse moments are in terms of Gaussian quadrature connected to both the distribution function $F(\omega)$ and a density function $f(\omega)$. In the particular case of interest, the density function $f(\omega)$ equals the decay width $\Gamma(E)$ (see Eq. (6)). The procedure and the background shortly explained here can be found in detail in Refs. 49, 50, 52, and 56. For convenience, we from this point on write the optimal abscissae $\frac{1}{\omega_i}$ as ε.

Having obtained the optimal abscissae and weights, the probability distribution function $F(\varepsilon)$ can be approximated. For this purpose, the so-called Stieltjes imaging is employed, where

$$F^{(n)}(\varepsilon) = \begin{cases} 0 & \varepsilon < \varepsilon_1 \\ \sum_{j=1}^{i} f_j & \varepsilon_i < \varepsilon < \varepsilon_{i+1} \\ \sum_{j=1}^{n} f_j = S(0) & \varepsilon_n < \varepsilon. \end{cases} \tag{28}$$

This procedure is based on the so-called Chebyshev inequalities

$$F^{(n)}(\varepsilon_i - 0) \le F^{(n+1)}(\varepsilon_i - 0) \le F(\varepsilon_i) \le F^{(n+1)}(\varepsilon_i + 0) \le F^{(n)}(\varepsilon_i + 0). \tag{29}$$

This means that the distribution functions obtained from the Chebyshev polynomials approaching the abscissae ε_i from below and from above give lower and upper bounds to the actual value of the distribution function at this particular point $F(\varepsilon_i)$. In fact, the mean of these two values usually is a very good approximation to the exact value

$$F^{(n)}(\varepsilon_i) = \frac{1}{2}\left[F^{(n)}(\varepsilon_i - 0) + F^{(n)}(\varepsilon_i + 0)\right]. \tag{30}$$

Since the integral was evaluated and not the density function, as such the distribution function obtained from the discrete pseudo-spectrum is normalized correctly (see Ref. 52). This distribution function is then numerically differentiated via

$$f^{(n)}(\varepsilon) = \begin{cases} \frac{1}{2}\frac{f_1}{\varepsilon_1} & \varepsilon < \varepsilon_1 \\ \frac{1}{2}\frac{f_{i+1} + f_i}{\varepsilon_{i+1} - \varepsilon_i} & \varepsilon_i < \varepsilon < \varepsilon_{i+1} \\ 0 & \varepsilon_n < \varepsilon \end{cases} \tag{31}$$

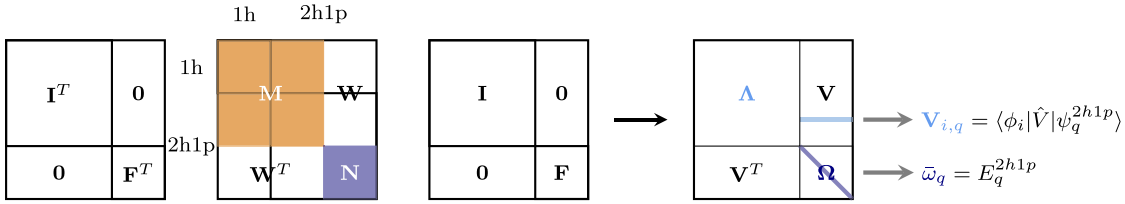

FIG. 3. Schematic illustration of the basis transformation of the full ADC matrix into the basis of initial and final states. The pseudo-spectrum is given by the manifold of $\bar{\omega}_q$ and $V_{i,q} = \langle\phi_i|\hat{V}|\psi_q^{2h1p}\rangle$.

to give $r-1$ non-zero points of the desired density function $f(\varepsilon)$, which are subsequently interpolated. In the routine of Averbukh, a monotonicity-preserving piecewise cubic Hermite spline interpolation is used for this purpose. Afterwards, the interpolated density function is evaluated for the energy of interest, which is the resonance energy E_r in case of the autoionization processes to give the decay width Γ. Finally, convergence of the decay widths with increasing orders of moments is investigated.

Unfortunately, the procedure to obtain the optimal abscissae and weights involves the subtraction of two large numbers, which leads to numerical instabilities in high order moments. Therefore, they have to be checked carefully and only trustworthy moments should be used for the evaluation of the decay widths. This can be achieved by inspection of abscissae and weights of each order. Since the decay width $\Gamma(E)$ is a smooth function, unphysical oscillations in the curve constructed from the abscissae and weights of one order of moments indicate numerical instabilities in this particular order. If this behaviour is observed, the abscissae and weights obtained from this order of moments and all higher orders are discarded. Finally, the abscissae and weights from the remaining, consecutive orders of moments enter the interpolation scheme.

III. COMPUTATIONAL DETAILS

The decay width calculations were performed using the relativistic FanoADC-Stieltjes code, which has been implemented in Dirac.[44] For each element, four-component calculations based on the Dirac-Coulomb Hamiltonian, scalar-relativistic spin-free calculations, and non-relativistic calculations were performed. Hereby, the respective cv4z basis sets of Dyall[57] were used and diffuse basis functions of the Kaufmann-Baumeister-Jungen type[58] were added at the center of the atom. For the s, p, and d-type functions, five functions were added for each orbital type and three f-type functions were added to the basis set.

The resulting moments were checked for numerical instabilities. Only those moments without numerical instabilities entered the interpolation scheme for the determination of the decay widths.

The expectation value of the radial distance $\langle r \rangle$ and orbital densities were performed using the atomic program GRASP.[59]

IV. RESULTS AND DISCUSSION

We present theoretical values for the Kr$3d^{-1}$, Xe$4d^{-1}$, and Rn$5d^{-1}$ Auger decay widths. The relativistically calculated single and double ionization potential spectra (SIPs and DIPs) for xenon are shown in Fig. 4 as representative of the three noble gases.[33–35] A more detailed population analysis of the double ionization spectrum can be found in Ref. 60. From this, the energetically accessible Auger decay channels can be deduced by comparison of the respective spectra. All doubly ionized states with an ionization energy lower than the ionization energy of the initial $(n-1)$d state can be populated after the decay. Hence, three major final state groups are found in all three cases: ns^{-2}, $ns^{-1}np^{-1}$, and np^{-2}. From the corresponding $2h$ configurations, the final state subspaces of the decay width calculations were constructed.

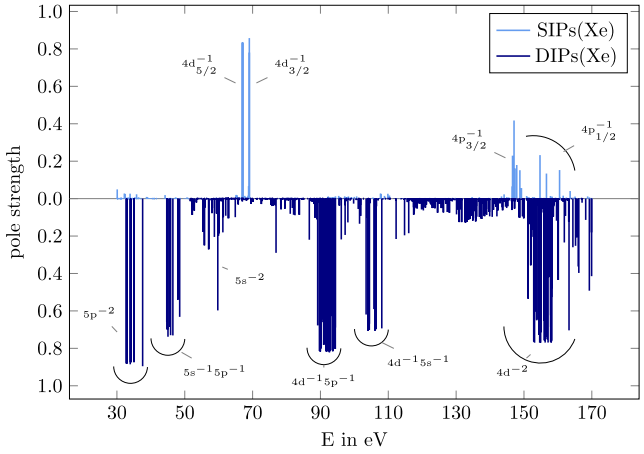

FIG. 4. Comparison of the single and double ionization spectra of the xenon atom obtained by a DC-ADC calculation. All groups of doubly ionized states with lower energies than the initially ionized Xe$4d^{-1}$ can be considered as possible final states.

Due to truncation of the full ADC matrix caused by the partitioning into initial and final state subspaces, the absolute value of the single ionization energy of the initial state used as approximation to the real part of the resonance energy loses accuracy. Even though the discrepancies are about 1–2 eV, this shift does only have a minor effect on the resulting decay widths in the results presented here, because the density functions $\Gamma(E)$ are very flat around the resonance energy. However, this shift can in general be a source of error and results obtained with the FanoADC-Stieltjes method have to be checked carefully.

The resulting decay widths and, if available, experimental and theoretically obtained decay widths for comparison are shown in Table I.

For krypton, one other set of calculated decay widths is available in the literature.[61] These calculations are based

TABLE I. Total Auger decay widths of the Kr, Xe, and Rn Rg$(n-1)\mathrm{d}^{-1}_{5/2}$, and Rg$(n-1)\mathrm{d}^{-1}_{3/2}$ and the non-relativistic Rg$(n-1)\mathrm{d}^{-1}$ initial states compared to theoretical values for krypton,[61] xenon,[62] and experimental values for xenon.[63] All widths are given in meV.

Γ	Initial state	Exp.	Theoretical	This work
Kr	$3d_{5/2}$	...	51	63
	$3d_{3/2}$	...	49	56
	$3d_{spinfree}$	...	...	62
	$3d_{nrel}$	...	...	49
Xe	$4d_{5/2}$	110–130	160	162
	$4d_{3/2}$	105–116	143	132
	$4d_{spinfree}$	...	...	168
	$4d_{nrel}$	...	...	90
Rn	$5d_{5/2}$	...	...	624
	$5d_{3/2}$	...	...	547
	$5d_{spinfree}$	...	...	686
	$5d_{nrel}$	...	...	161

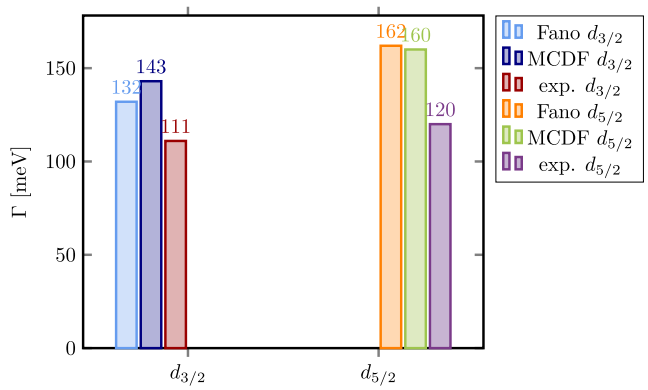

FIG. 5. Comparison of the xenon Auger decay widths from the Xe4$d_{3/2}^{-1}$ and 4$d_{5/2}^{-1}$ initial state obtained with the relativistic FanoADC in this work, the MMCDF approach,[62] and mean experimental values.[63] The calculated values are in very good agreement with each other, while both methods provide higher decay widths than the experimental ones.

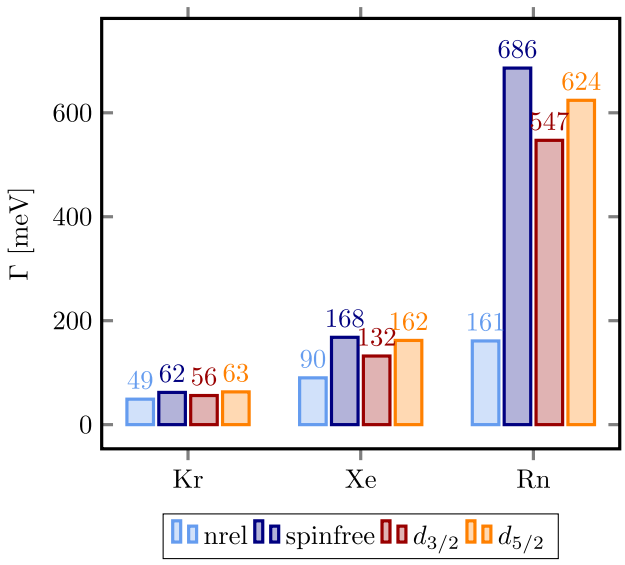

FIG. 6. Comparison of the Auger decay widths after primary ionization in the Rg$(n-1)d^{-1}$ for different Hamiltonians. The non-relativistically obtained results are lower than those obtained with the spinfree and four-component Hamiltonian. Overall, the decay width increases with the atomic number Z.

on a many-body perturbation approach including all orders of perturbation. The authors state that these results are approximately 75% of the values for calculations including perturbations up to second order only. Therefore, the second order numbers would agree well with our values obtained with the FanoADC-Stieltjes method shown in Table I. However, all integrations in this procedure rely on analytic evaluation using angular momentum algebra and are hence not applicable to non-spherical systems.

In case of Xe, both experimental and theoretical data are available in the literature. A graphical comparison of this data to our results is shown in Figure 5. The theoretical results from Ref. 62 were obtained using the MMCDF method.[45] For quantum chemists, the name of this method might be misleading, since it is by no means equivalent to Multi-Configurational Self-Consistent Field (MCSCF). MMCDF is based on an atomic Dirac-Fock calculation. For the initial state description of the xenon decay widths in Ref. 62, the pure Dirac-Fock solution is used. For the final state description, the Dirac-Fock solution is the reference state for a CI approach. Then, the excitation classes are chosen manually based on the experience of the scientist as well as by trial and error. In the case of the xenon decay widths shown in Table I and Figure 5, $5s^0 5p^6$, $5s^1 5p^5$, and $5s^2 5p^4$ configurations were included in the final state description. This resembles the space spanned by the $2h1p$ states in our FanoADC-Stieltjes approach. However, the method is generally not limited to doubly ionized states but can additionally include higher order excitations as well (see, e.g., Ref. 64). Hence, results from both the FanoADC-Stieltjes approach presented in this work and the MMCDF results of Ref. 62 include dynamic correlation in the description of the final state. However, the results obtained with the FanoADC-Stieltjes method incorporate correlation effects in the initial state description as well.

Considering the different qualities of the initial state description, the results of Ref. 62 are in excellent agreement with the results obtained with the fully relativistic four-component FanoADC-Stieltjes method. Both approaches overestimate the decay width compared to experiment. Taking into account that in this non-trivial problem of the calculation of decay widths, errors within a factor of two are to be expected, the results are in reasonably good agreement with experiment as well. Latest results of Sukhorukov indicate that the overestimation of the decay widths by both the MMCDF and the FanoADC results is due to these methods lacking the description of core polarization[65,66] first discussed by Born and Heisenberg.[67]

From Table I and Figure 6, it can be seen that only the four-component calculation is capable of describing the spin-orbit splitting which causes two different initial states. Therefore, this calculation is to be preferred. However, by employing the other schemes as well, one can learn more about the nature of the decay process.

The spinfree results with scalar-relativistic effects included are very close to the fully relativistic results for all three elements. In contrast to this, the non-relativistically obtained decay width is much smaller in all three cases. The difference increases as one goes down in the periodic table, which is summarized in Table II. In case of radon, the decay width is about four times as high as one would expect from a non-relativistic treatment.

This shows that the inclusion of at least scalar-relativistic effects is crucial in the calculation of autoionization decay widths in systems containing heavy elements. The reason for this behaviour can easily be understood, remembering that scalar-relativistic effects can phenomenologically be described as the decontraction of d and f and the contraction of s and

TABLE II. Absolute and relative increase of the decay widths due to the inclusion of scalar-relativistic effects in the calculations. The absolute decrease is given in meV.

	Kr	Xe	Rn
$\Delta_{spinfree,nrel}$	13	78	525
Increase	+27%	+87%	+326%

TABLE III. Expectation values of the electron's distance from the nucleus for the noble gases Kr, Xe, and Rn given in Å.

$\langle r \rangle$		$(n-1)\mathrm{d}_-$	$(n-1)\mathrm{d}_+$	$n\mathrm{s}$	$n\mathrm{p}_-$	$n\mathrm{p}_+$
Kr	rel	0.292	0.293	0.847	1.013	1.037
	nrel	0.291		0.862	1.033	
Xe	rel	0.460	0.466	1.008	1.186	1.245
	nrel	0.460		1.048	1.237	
Rn	rel	0.559	0.578	1.017	1.186	1.366
	nrel	0.561		1.141	1.346	

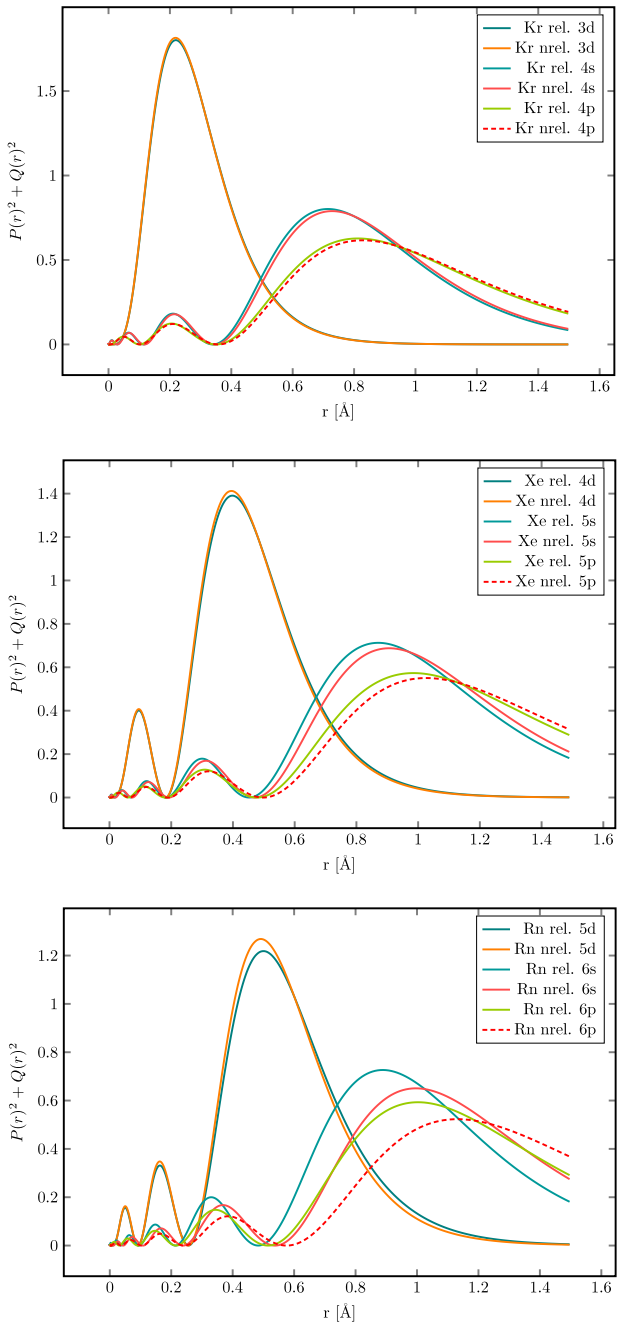

FIG. 7. Probability densities $P(r)^2+Q(r)^2$ for the orbitals participating in the Auger decay for Kr, Xe, and Rn calculated both relativistically and non-relativistically.

p orbitals, which in this case corresponds to initial and final states, respectively (see Table III and Figure 7). It can be seen that the decontraction of the d orbitals is only minor but the contraction of especially the *s* orbitals and also the *p* orbitals is remarkable and increases within the group.

Hence, the difference $\Delta\langle r \rangle = \langle r_{in} \rangle - \langle r_{fin} \rangle$ between the distance expectation values of the electron $\langle r \rangle$ from the nucleus between the orbitals describing the initial state and those orbitals describing the final states is decreased. This leads to an increased spatial overlap between the initial and final states, which in turn influences the decay width by making the s/p → d de-excitation transition more efficient. In the case at hand, the smaller $\Delta\langle r \rangle$ leads to an increase of the decay width. Likewise, a larger $\Delta\langle r \rangle$ would lead to a decrease of the decay width compared to the non-relativistic description.

This effect does not only affect the decay widths of Auger processes but also the decay widths of many other autoionization processes like the ICD or the Electron Transfer Mediated Decay (ETMD). The latter relies on an electron transfer between two units and hence can be expected to be crucially influenced by the scalar-relativistic effects reported in this work. Both will be subject to future research.

V. CONCLUSIONS

We presented the relativistic counterpart of the non-relativistically known FanoADC-Stieltjes approach. This method is able to predict decay widths including relativistic effects also for non-spherical systems, which was not possible so far, according to our knowledge, with other approaches. The calculations of ICD decay widths using the relativistic FanoADC-Stieltjes approach are going to be subject of future work.

Decay widths for the Auger process following an initial ionization from the $(n-1)$d of krypton, xenon, and radon were calculated using three different Hamiltonians. They cover the four component approach including both spin-orbit coupling and scalar-relativistic effects, the spinfree approach only including scalar-relativistic effects and the non-relativistic approach for comparison. In the results, we observe a large influence of the scalar-relativistic effects, which increases going down in the periodic table within a group. We show that these are caused by a change in overlap of the orbitals involved in the decay mainly due to the contraction of the *s* and *p* orbitals.

We predict these findings not to be unique to Auger processes but to be a general effect in autoionization processes including ICD and ETMD. Therefore, we propose further investigation of ICD and ETMD processes in systems containing heavy elements. The systems of interest for this purpose are systems with initially ionized *d* orbitals and final states containing vacancies in *s* orbitals. Also, the inverse setup with the initial vacancy in an *s* orbital and final states containing *d* vacancies can be expected to show the influence of relativistic effects. These effects are expected to be larger in ETMD than in ICD processes. However, due to the large computational cost growing with system size, one would start to study the ICD process.

ACKNOWLEDGMENTS

E.F. gratefully acknowledges funding from the Centre for Theoretical and Computational Chemistry, the DFG research unit FOR 1789, and the Deutscher Akademischer Austauschdienst. P.K. acknowledges financial support from the Czech Science Foundation (Project No. GAČR P208/12/0521).

[1]L. Meitner, Z. Phys. **9**, 131 (1922).
[2]P. Auger, C. R. Acad. Sci. **177**, 169 (1923).
[3]L. S. Cederbaum, J. Zobeley, and F. Tarantelli, Phys. Rev. Lett. **79**, 4778 (1997).
[4]S. Marburger, O. Kugeler, U. Hergenhahn, and T. Möller, Phys. Rev. Lett. **90**, 4 (2003).
[5]J. Zobeley, R. Santra, and L. S. Cederbaum, J. Chem. Phys. **115**, 5076 (2001).
[6]R. Santra, J. Zobeley, and L. S. Cederbaum, Phys. Rev. B **64**, 245104 (2001).
[7]S. Scheit, V. Averbukh, H.-D. Meyer, N. Moiseyev, R. Santra, T. Sommerfeld, J. Zobeley, and L. S. Cederbaum, J. Chem. Phys. **121**, 8393 (2004).
[8]T. Jahnke, A. Czasch, M. S. Schöffler, S. Schössler, A. Knapp, M. Käsz, J. Titze, C. Wimmer, K. Kreidi, R. E. Grisenti, A. Staudte, O. Jagutzki, U. Hergenhahn, H. Schmidt-Böcking, and R. Dörner, Phys. Rev. Lett. **93**, 4 (2004).
[9]G. Öhrwall, M. Tchaplyguine, M. Lundwall, R. Feifel, H. Bergersen, T. Rander, A. Lindblad, J. Schulz, S. Peredkov, S. Barth, S. Marburger, U. Hergenhahn, S. Svensson, and O. Björneholm, Phys. Rev. Lett. **93**, 173401 (2004).
[10]M. Lundwall, W. Pokapanich, H. Bergersen, A. Lindblad, T. Rander, G. Öhrwall, M. Tchaplyguine, S. Barth, U. Hergenhahn, S. Svensson, and O. Björneholm, J. Chem. Phys. **126**, 214706 (2007).
[11]E. Fasshauer, M. Förstel, S. Pallmann, M. Pernpointner, and U. Hergenhahn, New J. Phys. **16**, 103026 (2014).
[12]I. B. Müller and L. S. Cederbaum, J. Chem. Phys. **125**, 204305 (2006).
[13]S. D. Stoychev, A. I. Kuleff, and L. S. Cederbaum, J. Chem. Phys. **133**, 154307 (2010).
[14]P. Slavíček, B. Winter, L. S. Cederbaum, and N. V. Kryzhevoi, J. Am. Chem. Soc. **136**, 18170 (2014).
[15]T. Jahnke, H. Sann, T. Havermeier, K. Kreidi, C. Stuck, M. Meckel, M. Schöffler, N. Neumann, R. Wallauer, S. Voss, A. Czasch, O. Jagutzki, A. Malakzadeh, F. Afaneh, T. Weber, H. Schmidt-Böcking, and R. Dörner, Nat. Phys. **6**, 139 (2010).
[16]M. Mucke, M. Braune, S. Barth, M. Förstel, T. Lischke, V. Ulrich, T. Arion, U. Becker, A. Bradshaw, and U. Hergenhahn, Nat. Phys. **6**, 143 (2010).
[17]N. V. Kryzhevoi and L. S. Cederbaum, Angew. Chem., Int. Ed. **50**, 1306 (2011).
[18]J. Zobeley, L. S. Cederbaum, and F. Tarantelli, J. Chem. Phys. **108**, 9737 (1998).
[19]P. H. P. Harbach, M. Schneider, S. Faraji, and A. Dreuw, J. Phys. Chem. Lett. **4**, 943 (2013).
[20]E. Surdutovich and A. V. Solov'yov, Eur. Phys. J. D **66**, 206 (2012).
[21]H.-K. Kim, J. Titze, M. Schöffler, F. Trinter, M. Waitz, J. Voigtsberger, H. Sann, M. Meckel, C. Stuck, U. Lenz, M. Odenweller, N. Neumann, S. Schössler, K. Ullmann-Pfleger, B. Ulrich, R. Costa Fraga, N. Petridis, D. Metz, A. Jung, R. Grisenti, A. Czasch, O. Jagutzki, L. Schmidt, T. Jahnke, H. Schmidt-Böcking, and R. Dörner, Proc. Natl. Acad. Sci. U. S. A. **108**, 11821 (2011).
[22]U. Hergenhahn, Int. J. Radiat. Biol. **88**, 871 (2012).
[23]B. Boudaïffa, P. Cloutier, D. Hunting, M. A. Huels, and L. Sanche, Science **287**, 1658 (2000).
[24]X. Pan, P. Cloutier, D. Hunting, and L. Sanche, Phys. Rev. Lett. **90**, 208102 (2003).
[25]F. Martin, P. D. Burrow, Z. Cai, P. Cloutier, D. Hunting, and L. Sanche, Phys. Rev. Lett. **93**, 068101 (2004).
[26]A. Bande, K. Gokhberg, and L. S. Cederbaum, J. Chem. Phys. **135**, 144112 (2011).
[27]M. Reiher and A. Wolf, *Relativistic Quantum Chemistry* (Wiley-VCH Verlag GmbH, 2009).
[28]E. Fasshauer, M. Pernpointner, and K. Gokhberg, J. Chem. Phys. **138**, 014305 (2013).
[29]J. Schirmer, Phys. Rev. A **26**, 2395 (1982).
[30]J. Schirmer, Phys. Rev. A **43**, 4647 (1991).
[31]J. Schirmer, A. B. Trofimov, and G. Stelter, J. Chem. Phys. **109**, 4734 (1998).
[32]F. Mertins and J. Schirmer, Phys. Rev. A **53**, 2140 (1996).
[33]M. Pernpointner and A. B. Trofimov, J. Chem. Phys. **120**, 4098 (2004).
[34]M. Pernpointner, J. Chem. Phys. **121**, 8782 (2004).
[35]M. Pernpointner, J. Phys. B **43**, 205102 (2010).
[36]H. Feshbach, Ann. Phys. **5**, 357 (1958).
[37]U. Fano, Phys. Rev. **124**, 1866 (1961).
[38]H. Feshbach, Ann. Phys. **19**, 287 (1962).
[39]R. Santra and L. S. Cederbaum, Phys. Rep. **368**, 117 (2002).
[40]J. J. Sakurai, in *Modern Quantum Mechanics*, rev. ed., edited by S. F. Tuan (Addison-Wesley, 1994).
[41]N. Vaval and L. S. Cederbaum, J. Chem. Phys. **126**, 164110 (2007).
[42]A. Ghosh, N. Vaval, S. Pal, and R. J. Bartlett, J. Chem. Phys. **141**, 164113 (2014).
[43]V. Averbukh and L. S. Cederbaum, J. Chem. Phys. **123**, 204107 (2005).
[44]DIRAC, a relativistic *ab initio* electronic structure program, Release DIRAC13 (2013), written by L. Visscher, H. J. Aa. Jensen, R. Bast, and T. Saue, with contributions from V. Bakken, K. G. Dyall, S. Dubillard, U. Ekström, E. Eliav, T. Enevoldsen, E. Faßhauer, T. Fleig, O. Fossgaard, A. S. P. Gomes, T. Helgaker, J. K. Lærdahl, Y. S. Lee, J. Henriksson, M. Iliaš, Ch. R. Jacob, S. Knecht, S. Komorovský, O. Kullie, C. V. Larsen, H. S. Nataraj, P. Norman, G. Olejniczak, J. Olsen, Y. C. Park, J. K. Pedersen, M. Pernpointner, K. Ruud, P. Sałek, B. Schimmelpfennig, J. Sikkema, A. J. Thorvaldsen, J. Thyssen, J. van Stralen, S. Villaume, O. Visser, T. Winther, and S. Yamamoto (see http://www.diracprogram.org).
[45]S. Fritzsche, A. N. Grum-Grzhimailo, E. V. Gryzlova, and N. M. Kabachnik, J. Phys. B **44**, 175602 (2011).
[46]G. Wentzel, Z. Phys. **43**, 524 (1927).
[47]J. Craigie, A. Hammad, B. Cooper, and V. Averbukh, J. Chem. Phys. **141**, 014105 (2014).
[48]A. Hazi, J. Phys. B **11**, L259 (1978).
[49]P. W. Langhoff, C. T. Corcoran, F. Sims, J. S. Weinhold, and R. M. Glover, Phys. Rev. A **14**, 1042 (1976).
[50]C. T. Corcoran and P. W. Langhoff, J. Math. Phys. **18**, 651 (1977).
[51]F. Müller-Plathe and G. H. F. Diercksen, *Electronic Structure of Atoms, Molecules and Solids* (Kluwer Academic Publishers, 1990).
[52]W. P. Reinhardt, Comput. Phys. Commun. **17**, 1 (1979).
[53]E. Fasshauer, "Investigation of relativistic effects in electronic decay processes in small and large noble gas clusters by *ab initio* and new simulation approaches," Ph.D. thesis (University of Heidelberg, 2014).
[54]J. Schirmer, L. S. Cederbaum, and O. Walter, Phys. Rev. A **28**, 1237 (1983).
[55]A. B. Trofimov and J. Schirmer, J. Chem. Phys. **123**, 144115 (2005).
[56]F. Müller-Plathe and G. H. F. Diercksen, Phys. Rev. A **40**, 696 (1989).
[57]K. G. Dyall, Theor. Chem. Acc. **115**, 441 (2006).
[58]K. Kaufmann, W. Baumeister, and M. Jungen, J. Phys. B **22**, 2223 (1989).
[59]F. A. Parpia, C. Froese Fischer, and I. P. Grant, Comput. Phys. Commun. **94**, 249 (1996).
[60]M. Pernpointner, J. P. Zobel, and N. V. Kryzhevoi, Phys. Rev. A **85**, 012205 (2012).
[61]J. C. Baggesen, E. Lindroth, and L. B. Madsen, Phys. Rev. A **85**, 013415 (2012).
[62]A. Mäntykenttä, Phys. Rev. **47**, 3961 (1993).
[63]A. Ausmees, A. Hahlin, S. L. Sorensen, S. Sundin, I. Hjelte, O. Björneholm, and S. Svensson, J. Phys. B **32**, 197 (1999).
[64]S. Heinäsmäki, H. Aksela, J. Nikkinen, E. Kukk, A. Kivimäki, S. Aksela, and S. Fritzsche, J. Electron Spectrosc. Relat. Phenom. **137–140**, 281 (2004).
[65]I. D. Petrov, B. M. Lagutin, V. L. Sukhorukov, A. Ehresmann, and H. Schmoranzer, J. Phys. B **47**, 055001 (2014).
[66]V. L. Sukhorukov, I. D. Petrov, M. Schäfer, F. Merkt, M.-W. Ruf, and H. Hotop, J. Phys. B **45**, 092001 (2012).
[67]M. Born and W. Heisenberg, Z. Phys. **23**, 388 (1924).